# Porous Anodic Aluminum Oxide Scaffolds;

# Formation Mechanisms and Applications

By

JIHUN OH

B. S., Pohang University of Science and Technology (POSTECH), Korea (2000)

M. S., Seoul National University, Korea (2002)

Submitted to the Department of Materials Science and Engineering
In Partial Fulfillment of the Requirements of the Degree of

DOCTOR OF PHILOSOPHY
at the
MASSACHUSETTS INSTITUTE OF TECHNOLOGY



February 2010



Author.....

Department of Materials Science and Engineering
January 2010

Certified by.....

Carl V. Thompson
Stavros Salapatas Professor of Materials Science and Engineering
Thesis Supervisor

Accepted by.....

Christine Ortiz
Associate Professor of Materials Science and Engineering
Chair, Departmental Committee on Graduate Students

# Porous Anodic Aluminum Oxide Scaffolds; Formation Mechanisms and Applications

by

Jihun Oh

Submitted to the Department of Materials Science and Engineering on January 11, 2010 in partial fulfillment of the requirements for the degree of Doctor of Philosophy

## Abstract

Nanoporous anodic aluminium oxide (AAO) can be created with pores that self-assemble into ordered configurations. Nanostructured metal oxides have proven to be very useful as scaffolds for growth of nanowires and nanotubes with tunable diameters and with tight diameter distributions. For 50 years, field-assisted dissolution of the oxide has been cited as the mechanism that leads to pore formation in alumina, and by analogy, porous anodic $TiO_2$ and other functional metal oxides.

We show that field-assisted dissolution models are consistent with the observed dependence of the $Al_2O_3$ dissolution rate on the electric field, as well as the existence of a critical field for pore initiation. However, we further show that the well-known ordered porous structure, which has a significantly different length scale, does not result from a field-induced instability, but is instead the result of a strain-induced instability with forced plastic deformation and flow of the oxide during further anodization. We demonstrate that these pore generation mechanisms can be controlled independently, even when they co-exist, by controlling the electric field across the oxide as well as the anodization conditions. We also show that mechanical confinement results in a dendritic pore structure. Through interpretation of these results we develop a generalized mechanism for ordered pore formation in AAO in analogy with cellular solidification.

In addition, we report on abnormal behavior in anodic oxidation of Al in mechanically confined structures for formation of horizontal nanoporous anodic alumina oxide, H-AAO. Instead of smooth pore walls, periodic dendrite inner pore structures form, the growth rate is suppressed to 5 % of its value during bulk anodization under the same conditions, and a steady-state is never reached. These anomalies associated with

formation of H-AAO originate from suppressed volume expansion and plastic flow of $Al_2O_3$ confined by the $SiO_2$ hard mask. By determining new anodization conditions leading to zero volume expansion, dendritic H-AAO can be avoided and kinetic retardation can be minimized.

A new method for perforation of the AAO barrier layer has been developed, based on anodization of Al/W bilayer films on substrates. When Al/W bilayer films are anodized and pores approach the Al/W interface, tungsten oxide forms and penetrates the alumina barrier oxide, in part, due to enhanced plasticity of the alumina layer. By selectively etching the tungsten oxide, the barrier oxide can be removed and the base of the pores opened, without etching of the AAO.

Finally, we further refined the selective barrier perforation process using the W interlayer to develop a methodology for fabrication of through-pore AAO scaffolds on any conducting substrate (AS) by anodizing an Al/W/AS tri-layer. Structural and kinetic study of the $WO_3$ extrusion revealed that the anodization of W consumes a fixed thickness of the W layer in acidic electrolytes under specific anodization conditions. Based on this study, the optimum thickness of the W interlayer in the Al/W/Au tri-layer was measured for various anodization conditions. Through-pore AAOs were fabricated on Au layers with exposure of the surface at the base of the pores, using the optimum W thickness without a violent $O_2$ evolution reaction and without changing the pore diameters. With scaffolds made using this methodology, vertically-aligned free-standing Au and Pt nanowires with diameters ranging from about 12 nm to about 120 nm were grown by electrodeposition on a gold substrate.

Thesis Supervisor: Carl V. Thompson
Stavros Salapatas Professor of Materials Science and Engineering

## Acknowledgement

This work can not be completed without people who support and inspire me during the course of Ph.D. work at MIT.

First of all, I would like to thank Prof. Carl V. Thompson for the inspiration and guidance. It is out of question that his insight is critical to the thesis. His endless patience and belief on me make it possible to complete this work. I thank the committee members of my thesis, Prof. Donald Sadoway and Prof. Henry I. Smith for their helpful discussion and comments.

Many of this work are done at the MTL and at the NSL with help of research staffs. Especially, I wish to thank Kurt Broderick at the MTL and James Daley at the NSL for the help with all equipment.

I appreciate all the contribution from my colleagues. I am thankful to the TSA subgroup colleagues, Amanda, Donghyun, Jongpil, Ram, and Shih-wei, and to the Wire and Tube subgroup colleagues, Gilbert, Steve, and Robert, for their helpful discussions and interactive collaborations. Colleagues in the Thompson group have been great. They have shared hands, ideas, and conversations in various subjects. Especially, I'm indebted to Reiner, Zung, Donghyun, and the 4$^{th}$ floor gangs for their support and for providing the stress relaxing moments. And good luck to junior students, Ahmed and Yong Cheol.

My friends around MIT/Boston helped me the very survival in Boston. Special thanks to them for many laughs and memorable hours. I also thank working-hard-and-playing-hard members of the KGMSE at MIT.

I have received unconditional support from my family. I would like to thank my family – grandmother, parent, brother, and sisters and parent-in-laws. Especially, my brother, Sang-Hun, inspires me in many aspects. Last, but not the least, I am blessed to be with my beloved wife, Sebin. She always encourages and supports me with constant love in the best and worst time during the course of this work, and has been a center for balancing my graduate life. No word can express my deepest gratitude to her. Every day with her has been blessing.

The research in this thesis is supported by the Marcoelectronics Advanced Research Corporation and the Singapore-MIT alliance.

# Table of Contents

# List of Figures

**Figure 5-6.** Tilted-angle (30°) SEM images of free-standing Au and Pt nanowires on Au substrates, formed by electrodeposition in various through-pore AAOs formed with controlled pore diameters. (a) Au nanowires with diameters of about 120 nm and spacings of about 200 nm and lengths of about 590 nm and (b) Au nanowires with diameters of about 31.8 nm and spacings of about 100 nm and lengths of about 530 nm. Scale bars = 1 mm. (c) Pt nanowires with 12 nm diameters, spacings of 65 nm and lengths of about 710 nm. Scale bar = 200 nm. (d) Large-area view of the Pt nanowires in (c). Scale bar = 5 μm..... 151

## List of Tables

# Chapter 1. Introduction and Previous Work

## 1.1 Anodization of Aluminum

Anodization of aluminum is a well-established process for production of protective and decorative coatings on Al surfaces [1-4]. Anodization of Al is an electrochemical oxidation process carried out by applying positive voltage to Al in an electrolyte and results in thickening of its oxide. Because of their simple fabrication procedure and its excellent corrosion resistance, anodic aluminum oxide (AAO) films have been used in numerous products for 100 years.

The structure of AAO films was first revealed in 1953 by Keller, Hunter, and Robinson who used transmission electron microscopy (TEM) to observe hexagonally closed packed pore arrays as an ideal structure of AAO [5]. In 1995, Masuda and Fukuda discovered that the ideal structures of AAO can be realized at certain anodization conditions [6]. Since then, with burgeoning progress in nanotechnology, AAO has come to be seen as an ideal scaffold for the synthesis of various low-dimensional nanomaterials [7-10].

Despite rapid progress in anodization technology, however, the mechanism for pore formation in AAO is still in debate. Fundamentally, pores are believed to form as a result of instability in the oxide during anodization [11-13]. The origin of the instability is still unclear. For exploitation of novel structures of AAO, a much improved understanding of pore formation must be provided.

In this chapter, I will present an overview of the science and technology in the field of Al anodization. Throughout the overview, I will identify scientific and technological challenges whose resolution constitutes the objective of this thesis.

## 1.2 Thermodynamics and Kinetics

### 1.2.1 Thermodynamics [14]

It is well-known to a vacuum scientist that formation of aluminum oxide from aluminum is thermodynamically favorable in an oxygen ambient, even at room temperature. The spontaneous reaction of oxidation of Al is driven by a large negative Gibb's free energy change during oxidation. Aluminum also readily reacts with water in aqueous environments, but yields various stable by-products including $Al_2O_3$, $Al_2O_3 \cdot 3H_2O$, aluminum ions ($Al^{3+}$), and aluminate ions ($AlO_2^-$). For the Al-water system, 6 reactions are known to occur, assuming the absence of complexing agents with Al. For example, Al forms its oxide with water by,

$$2Al + 3H_2O = Al_2O_3 + 6H^+ + 6e^- . \quad (1)$$

From the Nernst equation, the equilibrium equation of the reaction (1) is given as a function of electrode potential E and pH of the solution by

$$E = E_o - \frac{RT}{zF}\ln[H^+]^3 = -1.505 - 0.0591pH \ , \quad (2)$$

where $E_o$ is the standard reduction potential, R is the universal gas constant, T is the absolute temperature, z is the charge number of the electrode reaction (in this case, z = 3), and F is the Faraday constant (96,500 C/mol). The other 5 reactions are

$$Al^{3+} + 2H_2O = AlO_2^- + 4H^+, \quad (3)$$

$$2Al^{3+} + 3H_2O = Al_2O_3 + 6H^+, \quad (4)$$

$$Al_2O_3 + H_2O = 2AlO_2^- + 2H^+, \quad (5)$$

$$Al = Al^{3+} + 3e^-, \quad (6)$$

$$Al + 2H_2O = AlO_2^- + 4H^+ + 3e^-. \quad (7)$$

Each reaction has corresponding equilibrium equations, determined by the Nernst equation if the reaction is electrochemical in nature (the reaction (1), (6), and (7)) and Gibb's free energy of the reactions if the reaction is chemical in nature (the reaction (3), (4), and (5)).

The resulting equilibrium equations allow construction of domain boundaries in a potential-pH diagram or a Pourbaix diagram of the Al-water system as shown in Fig. 1-1 [15]. The Pourbaix diagram for the Al-water system is a thermodynamic stability map of chemical species of the metal-aqueous solution at 25°C in the space of potential (y-axis) and pH of the solution (x-axis). When Al is anodically polarized or anodized, that is E > 0 in Fig. 1-1, in neutral, weak acidic, and basic solutions, the growth of the oxide is thermodynamically favored as described by reaction (1). A compact layer of aluminum oxide, called a barrier-type oxide, is known to grow in these conditions [1-4]. If Al is anodized in a strong acid such as perchloric acid, Al dissolves into the solution, and this process is called electropolishing of Al [2]. The electropolishing of Al proceeds by the reaction (6). In mildly acidic solutions, such as diluted phosphoric, oxalic, and sulfuric acids, it is well-known that porous alumina grows as a result of anodization [1-4]. It should be noted that formation of porous alumina is not expected from the simple

thermodynamic considerations shown in Fig. 1-1. Generally, it is widely believed that combination of the oxidation reaction (1) and the Al dissolution reaction (6) occurs [1]. However, this argument relies on slow kinetics of Al dissolution, not thermodynamics. Therefore, a more detailed thermodynamic argument for porous alumina formation must be provided to answer whether porous alumina solely the result of kinetic constriants.

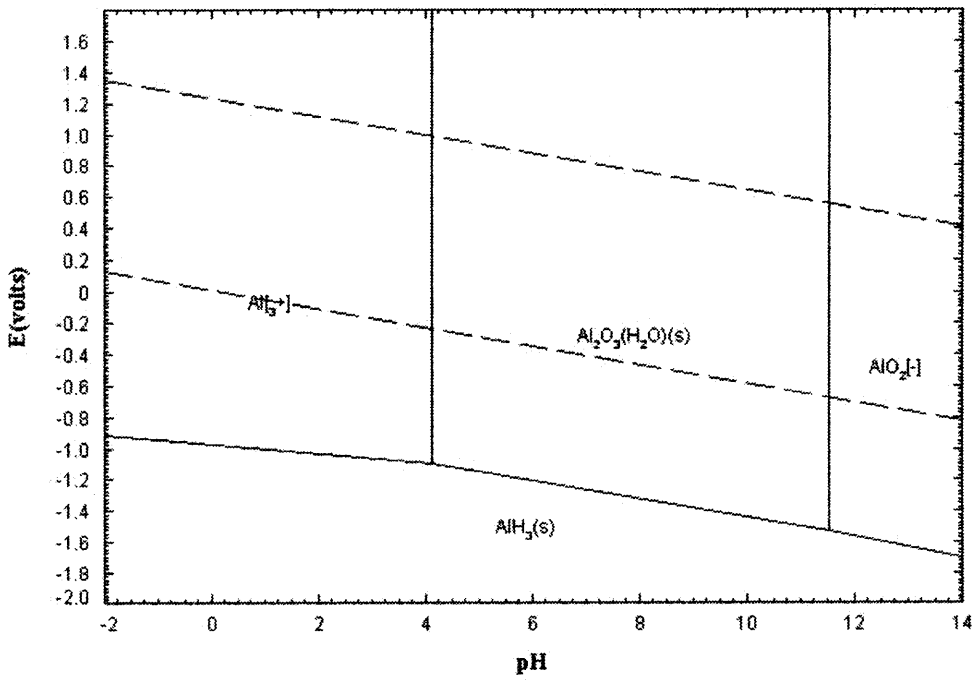


**Figure 1-1.** Pourbaix diagram of Al-$H_2O$ system 298K [15].

### 1.2.2. Kinetics and Interfacial Reactions

Anodic oxidation of Al proceeds though various kinetic steps associated with different ionic species ($Al^{3+}$ and $O^{2-}$). It is generally accepted from marker experiments that the anodic oxide grows simultaneously at both interfaces, i.e. at the metal/oxide

(m/o) interface by transport of oxygen ions and at the oxide/electrolyte (o/e) interface by transport of aluminum ions [16-18]. The relative fraction of the total current carried by a given ion is called as the transport number of an ion. In Al anodization, the transport number of $Al^{3+}$ varies from 0.2 ~ 0.7 as a function of anodic conditions such as pH, temperature, and applied current density [16, 18]. For porous oxides, a transport number for $Al^{3+}$ of about 0.4 is generally accepted [19].

For $O^{2-}$ ion transport during anodization, first, an oxygen ion (or $OH^-$) transfer reaction occurs at the o/e interface by the water splitting reaction [12] or

$$H_2O_{(aq)} = O^{2-}_{(ox)} + 2H^+_{(aq)}. \quad (8)$$

The transferred oxygen ions then migrate across the oxide to the m/o interface driven by the high electric field across the oxide, which is in the order of $10^6$ ~ $10^7$ V/cm [1]. Finally, the oxygen ions that arrive at the m/o interface react with Al metal to form $Al_2O_3$ by

$$2Al_m + 3O^{2-}_{ox} = Al_2O_3 + 6e^-. \quad (9)$$

Regarding the $Al^{3+}$ ions, the following reactions can occur. At the m/o interface, an ion transfer reaction takes places, such that

$$Al_m = Al^{3+}_{(ox)} + 3e^-. \quad (10)$$

At the o/e interface, two interfacial reactions are suggested, depending on the pH of the solution:

$$2Al^{3+}_{ox} + 3O^{2-}_{ox} = Al_2O_3 \quad (11)$$

in neutral solutions and/or

$$Al^{3+}_{ox} = Al^{3+}_{aq} \quad (12)$$

in acidic solutions. Implications of reaction (12) on porous alumina formation will be discussed in detail later in this chapter. The Al ion transport across the oxide is also driven by the high electric field. It should be noted that only reactions at the m/o interface are responsible for generation of anodic currents [20]. Shown in Fig. 1-2 is a summarized overall anodic reaction at both interfaces for porous oxide formation. Note the incorporation of the oxide dissolution reaction (4) in Fig. 1-2.

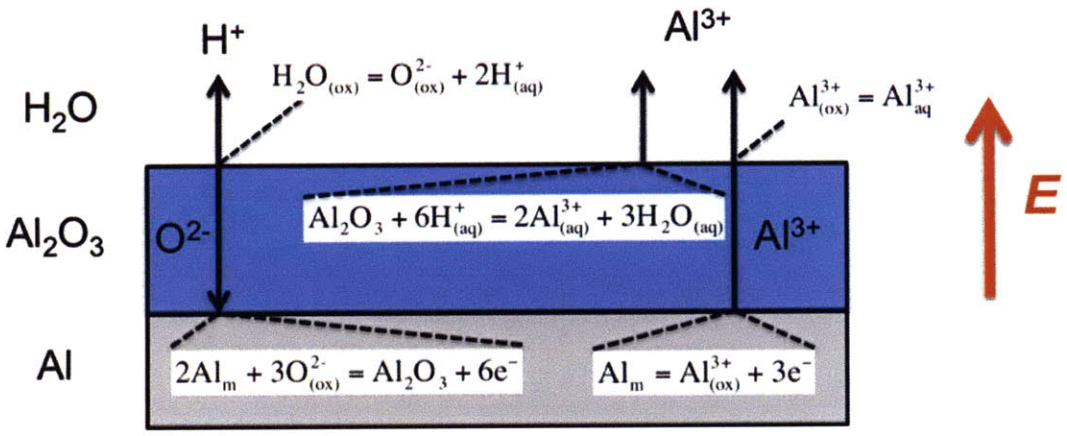


**Figure 1-2.** Summary of the interfacial reactions at the anode (Al).

Each kinetic step shown above can be a rate-determining step for film growth and the associated anodic oxide growth models have been proposed by various authors [1, 21, 22]. The specific description of each model is out of scope of this thesis but can be found in a review paper by Lohrengel [21] and in a work by Macdonald and coworkers [22]. Comparison of some of established models is summarized in Table 1-1. It is important to

point out that regardless of the rate-determining step, the kinetics of Al anodization can be described with a high-field conduction model or the Güntherschultz-Betz (G-B) equation,

$$j_i = j_0 \exp(\beta E). \tag{13}$$

Here, $j_i$ is the ionic current density due to the ion species $i$, $j_0$ and $\beta$ are temperature dependent parameters, and $E$ is the electric field across the oxide.

| Authors | Ref. | Ion | Rate determining step | Field strength | Kinetics |
|---|---|---|---|---|---|
| Güntherschulze and Betz (1934) | 109 | +, − | ox | $E=\Delta U/d$ | $i=i_0 \exp(\beta E)$ |
| Verwey (1935) | 110 | + | ox | | $i=i_0 \exp(\beta E)$ |
| Mott and Cabrera (1947) | 113 | + | me/ox | $E=$const. | $i=i_0 \exp(\beta E)$<br>$1/d=a-b \ln(t)$ |
| Vermilyea and Vetter (1955) | 176 | + | ox | $E=\Delta U/d$ | $i=i_0 \exp(\beta E)$<br>$dd/dt=Ai_0 \exp(\beta E)$ |
| Cohen and Sato (1964) | 114 | | | | $d=A+B \ln(t+t_0)$<br>Collective place exchange |
| Fehlner and Sato (1964) | 179 | − | ox/el | $E=$const. | $d=A+B \ln(t+t_0)$<br>$W=f(d)$ |
| Macdonald *et al.* (1981, 1991) | 107 | +, −<br>$e^-$, $h^+$ | ox<br>me/ox<br>ox/el | $E=$const.<br>No $f(d,U)$ | Point defect model |

**Table 1-1.** Comparison of kinetic models of anodic oxide growth [21].

## 1.3 Porous Anodic Aluminum Oxide Film

### 1.3.1 Nanostructure and Anodization Parameters

Porous anodic aluminum oxide is formed in mildly acidic solutions which promote dissolution of the oxide with application of a constant anodic voltage (potentiostatic mode) or a constant anodic current density (galvanostatic mode).

Typically, anodic voltages in the range of 10 ~ 200 V or current densities of 0.1 ~ 100 $mA/cm^2$ are used. Fig. 1-3 illustrates the structure of a porous alumina film. Porous alumina consists of vertically aligned cellular and cylindrical pores with diameters of the order of 10 ~ 300 nm and with, in principle, indefinite thickness. A scallop-shaped *barrier layer* at the base of the pores separates the porous layer and the Al substrate [5].

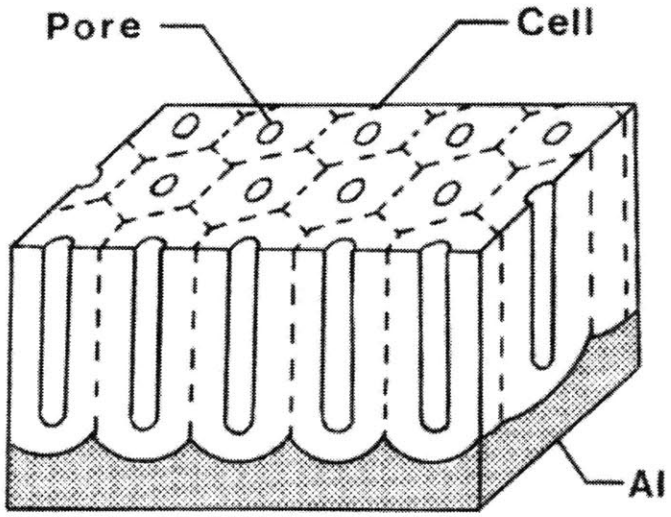


**Figure 1-3.** Schematic of ideal porous structure of anodic alumina [45].

While the thickness of porous alumina is controlled coulombically, the structure of porous AAO largely depends on the anodic potential (or formation voltage in the case of constant current mode) [1, 12]. Pore spacing, pore diameter, and thickness of the barrier layer at the pore base are linearly proportional to the anodic voltage and independent of the electrolytes used. For example, O'Sullivan and Woods showed that anodic voltage to barrier-layer thickness ratios, pore spacing, and pore diameter were

1.04, 2.77, and 1.29 $nmV^{-1}$ in the range of 80 ~ 120V in phosphoric acid [12]. Fig. 1-4 summarizes structural parameters for porous alumina as a function of anodic voltage in various electrolytes. More subtle dependencies of the structural features of porous alumina on other anodic conditions (pH, temperature, etc.) can be found in Dr. Krishnan's Ph.D. dissertation [23].

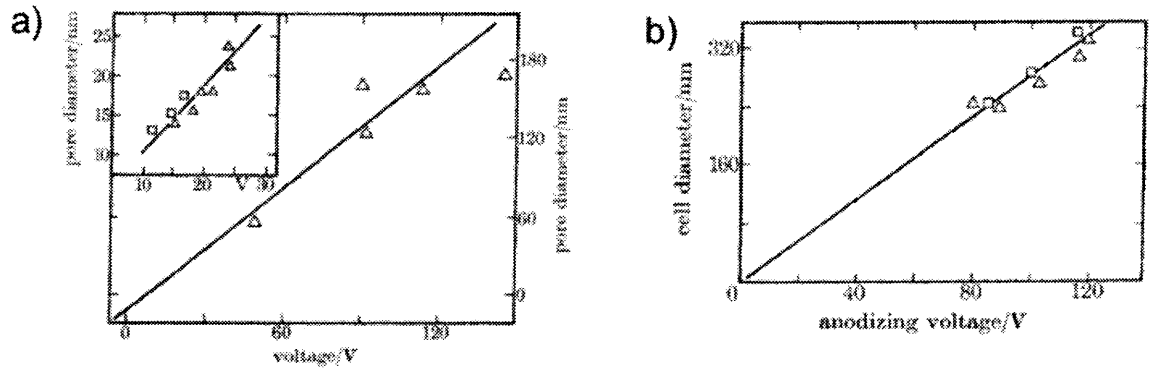


**Figure 1-4.** Linear dependence of (a) the pore diameter and (b) the pore spacing on the anodic voltage [12].

Since kinetics of anodization is governed by the high field conduction equation or the G-B equation, the ratio of the thickness of the barrier layer to the anodic voltage is an important parameter for understanding anodization kinetics and is called the anodizing ratio with units $nmV^{-1}$ [1]. Indeed, the anodizing ratio represents the reciprocal of the electric field across the barrier oxide ($E = V_{an}/d$) and, therefore, represents the anodic current or growth rate of the oxide given by Eq. (13). According to Eq. (13), the smaller the anodic ratio is, the faster porous alumina grows. For films formed in 0.4 M

phosphoric acid, the anodizing ratio decreases from 1.14 to 1.04 as the electrolyte temperature increases from 20 to 30°C at a constant voltage, and therefore the growth rate also increases with temperature [12]. In general, the anodizing ratio decreases as the aggressiveness of common electrolytes for porous oxide formation increase, and as a result, the growth rate of porous oxide increases with the aggressiveness of the electrolytes [1, 12]. The aggressiveness of electrolytes can increase by increasing the concentration of acids and temperature or by changing types of acids. For example, sulfuric acid is more aggressive than phosphoric acid and the resulting porous film has anodizing ratios of about 1 $nmV^{-1}$ and 1.14 $nmV^{-1}$, respectively, so that porous films in sulfuric acid solutions grow much faster at a given anodic voltage [12]. These characteristics are believed to arise from the coupled interplay of film formation and dissolution under the field, which will be discussed in the following chapter. In this regard, it is worth noting that the anodizing ratio of a planar barrier type oxide, which is formed in an electrolyte that does not dissolve $Al_2O_3$, is about 1.4 $nmV^{-1}$, larger than that of porous type oxides [1].

For complete understanding of the kinetics of porous alumina formation, however, quantitative analysis of the electric field distribution across the scalloped barrier layer of porous oxide must be provided. Surprisingly, it was not until 1992 that Parkhutik and Shershulsky calculated the electric field at both the m/o and o/e interfaces using the Poisson Equation, assuming the geometry of the barrier layer as a concentric hemisphere [24]. More recently, Houser and Hebert studied numerical simulation of the E-field and

potential distribution in porous oxide during steady-stage growth using the Poisson Equation with and without consideration of space charge, as shown in Fig. 1-5 [25].

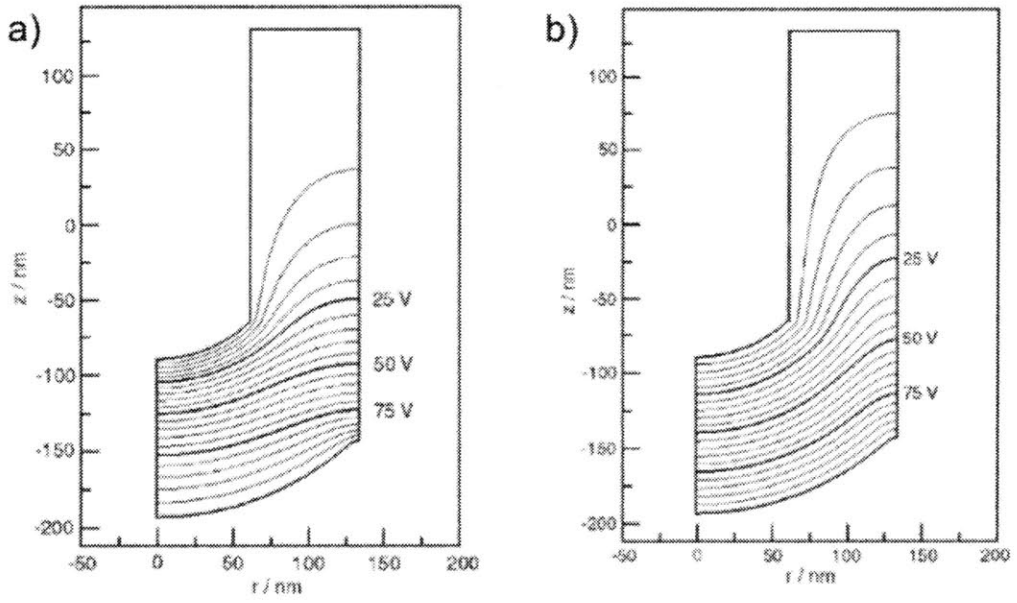


**Figure 1-5.** Potential distribution in the anodic oxide (a) with and (b) without space charge. A constant voltage of 100V is applied [25].

### 1.3.2 Current Transient and Pore Formation Stages

The structural evolution of pore formation can be monitored through the anodic current density in a constant voltage mode (or the formation voltage in constant current mode) [24, 26]. Fig. 1-6 (a) and (b) shows a schematic diagram of the anodic voltage and the anodic current transient, respectively, for anodization in mildly acid solutions [24]. Also shown are pore formation stages. In the galvanostatic mode, a constant current-density mode, (Fig. 1-6 (a)), the initial increase in the formation voltage represents gradual growth of the barrier type oxide, governed by the G-E equation (stage I). In

phenomenological terms, the resistance of the oxide is increasing at a constant rate due to thickening of the oxide. At stage II, embryonic pore structures develop at the o/e interface. Fig. 1-6 (c) shows a TEM image of the pore structure at stage II [26]. The stage II is also associated with the on-set of pore formation and Krishanan pointed out that the electrical charge passed through the oxide is constant regardless of anodization condition until the on-set of pore formation [23]. He also suggested that it could be related to the mechanism of pore initiation caused by generation of a critical tensile stress during anodization. Further anodizing results in a non-uniform E-field distribution across the oxide and therefore leads to well-developed pore structures with a scalloped barrier layer at the m/o interface (stage III). The formation voltage gradually decreases due to the drop in overall resistance due to the increase in the Al/oxide interfacial area. Finally, a steady-state pore structure is formed (stage IV). Evolution of a pore structure in a potentiostatic mode can be similarly explained. However, it must be noted that the barrier layer growth and pore initiation at the on-set of pore formation are not well-defined in potentiostatic-mode growth. To the best of the author's knowledge, details of pore evolution during stage I and II have not been investigated in potentiostatic mode, partially due to rapid evolution of the structure (typically $< 30$ s).

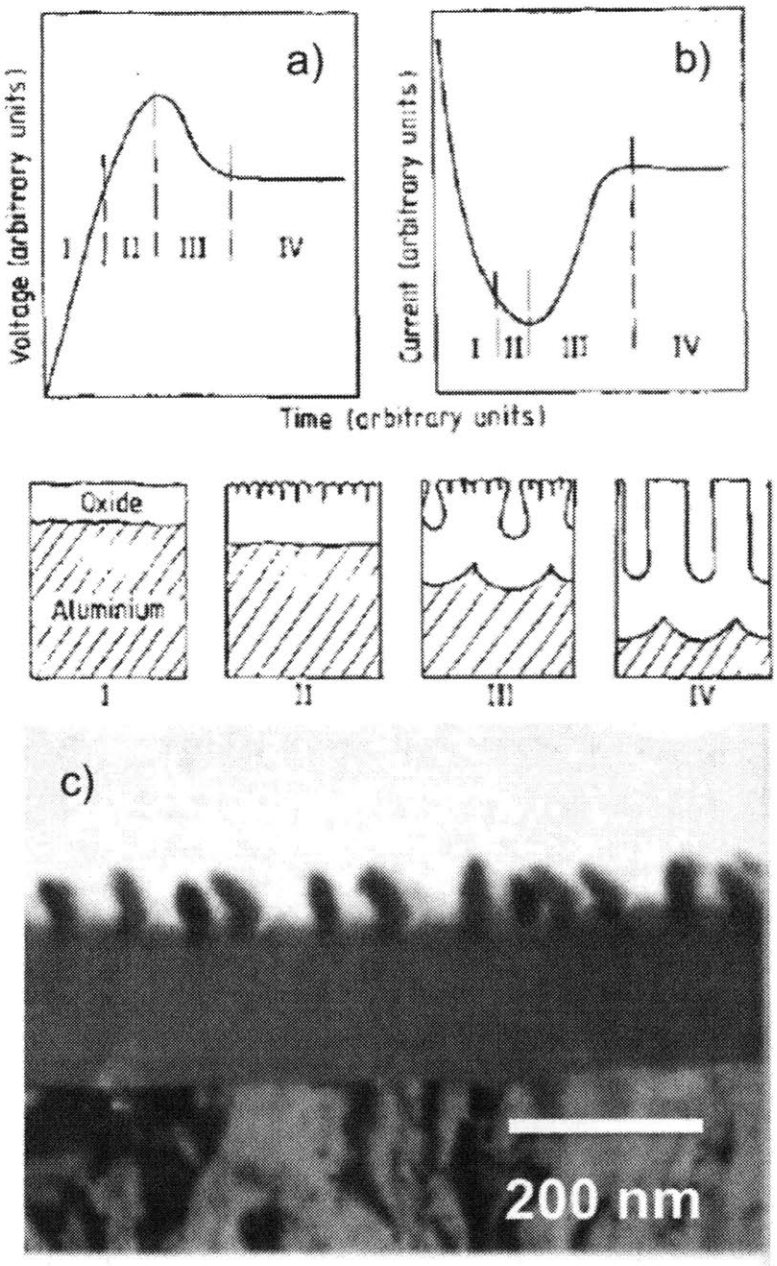


**Figure 1-6.** Schematic of the voltage and current transient in (a) galvanostatic and (b) potentiostatic modes [24]. The stages of porous structure evolution are also shown. (c) TEM image of the stage II [26].

## 1.4 Pore Formation Mechanisms

### 1.4.1 Field-Assisted Dissolution Model

Formation of porous AAO by anodizing Al in acidic electrolytes has distinctive features that contrast with formation of planar barrier-type oxides, which shed light on the mechanisms of pore formation [1, 12]. First, in the potentiostatic mode, or with application of a constant anodic voltage, porous alumina can grow indefinitely, while a barrier-type oxide stops growing with self-limiting manner as thickening of the oxide decreases the E-field across the oxide, as governed by the G-B equation. Second, the coating ratio or the current efficiency, that is the ratio of the weight of oxide formed to the weight of the aluminum consumed, for the formation of porous alumina is less than 100%. For example, the current efficiency for film growth in 0.4 M phosphoric acid with an anodizing current density of 5 $mA/cm^2$ at 293K is 62% [13]. In addition, as discussed above, the anodizing ratio of the barrier layer of a porous oxide, ~ 1.2 $nmV^{-1}$, is smaller than that of the barrier-type oxide, ~ 1.4 $nmV^{-1}$. These features imply that during porous growth a dynamic equilibrium is established between film formation by oxidation at the metal/oxide (m/o) interface and film dissolution at the oxide/electrolyte (o/e) interface. The chemical dissolution rate of the oxide, represented in Eq. (4), is, however, several orders of magnitude smaller than the formation rate at steady state. For instance, Hunter and Fowle estimated that dynamic equilibrium for anodizing at 0.2 $mA/cm^2$ in sulfuric acid at 21°C would require 53% acid boiling at 124°C at the pore bases to maintain dissolution at the required rate [27]. Local Joule heating at the base of pores was also

suggested for elevated dissolution rates of the oxide but the rise in temperature is less than 10°C [12].

The field-assisted dissolution model was first proposed by Hoar and Mott in 1959 [11]. In this model it is assumed that the dissolution rate of $Al_2O_3$ is greatly enhanced in presence of an E-field. As shown in Fig. 1-7 (a), the strength of the E-field is greatly increased at the pore bottom, P, due to the geometry, and therefore, the dissolution rate of the oxide is also increased at the pore base and the dynamic equilibrium between dissolution and oxidation can be establish. In detail, Hoar and Mott suggested that $Al_2O_3$ at the o/e interface at the point P in Fig. 1-7 (a) is spontaneously decomposed to $Al^{3+}$ and $O^{2-}$ ions in contact with acids and the $O^{2-}$ ions becomes $OH^-$ with reaction with $H^+$ in the acid and transport to the m/o interface due to the high E-field to form new oxide at the m/o interface, while $Al^{3+}$ ions goes into the solution. Since the oxide ions from point P are spread over a large area MN at the m/o interface, they suggested that the barrier oxide becomes thinner, that is dissolution of the oxide in net reaction is higher, based on volume conservation of oxygen in the oxide. The model, however, had not been widely accepted until O'Sullivan and Wood suggested a detailed physical mechanism for the electrochemical dissolution reaction in 1970 [1, 12, 28].

The seminal work by O'Sullivan and Wood has constituted a cornerstone for understanding the mechanisms of pore formation in Al and other metal oxide [12]. First, they suggested that the origin of oxygen ions in the oxide is mostly from water, which was later confirmed by $O^{16}$ and $O^{18}$ nuclear microanalysis, through hydrogen bond interaction between adsorbed water molecules and acid anions at the o/e interface [28,

29]. Second, they provided a physical origin for the field-assisted dissolution, as shown in Fig. 1-7 (b). They considered that the rate-limiting step for dissolution of the oxide is the interfacial reaction of breaking Al-O bonds in the Al lattice at the o/e interface. While hydrogen bonding in the solution can weaken the Al-O bonds, they further argued that application of a field across the oxide stretches the Al-O bond in the direction of the E-field from its equilibrium position, which can lower the effective activation energy for the dissolution, and, thus, greatly enhance the oxide dissolution rate. Since the E-field is focused in the pore bottom, the dissolution rate is greatest at the pore bottom and a dynamic equilibrium can be established.

Despite enormous amounts of experimental efforts on fabrication of anodic oxides, a very limited amount of work has been done on theoretical modeling of porous oxide formation [24, 30, 31]. By calculating the electric field distribution in the oxide using the Laplace equation and assuming the field-assisted dissolution of the oxide at the o/e interface as a rate-determining step during Al anodization, Parkhutik and Shershulsky were first to present an analytical expression providing a relationship between the pore structure and the electric field in the oxide with anodizing parameters, with successful demonstration of the linear dependence of pore spacing on the anodic voltage in a steady-state [24]. Thamida and Chang later modified Parkhutik's model using a linear and weakly non-linear stability analysis and predicted the critical electrolyte pH ($< 1.77$) for pore formation [30]. Additionally, Singh et al. performed a similar analysis but included the effects of stress on the dissolution rate of the oxide, arising from the Laplace pressure at the curved interfaces due to surface energy and volume expansion associated with

aluminum oxidation at the m/o interface [31]. Moreover, by incorporating of the effect of elastic stress from volume expansion, the Singh model allows prediction of the formation of self-ordered porous AAO.

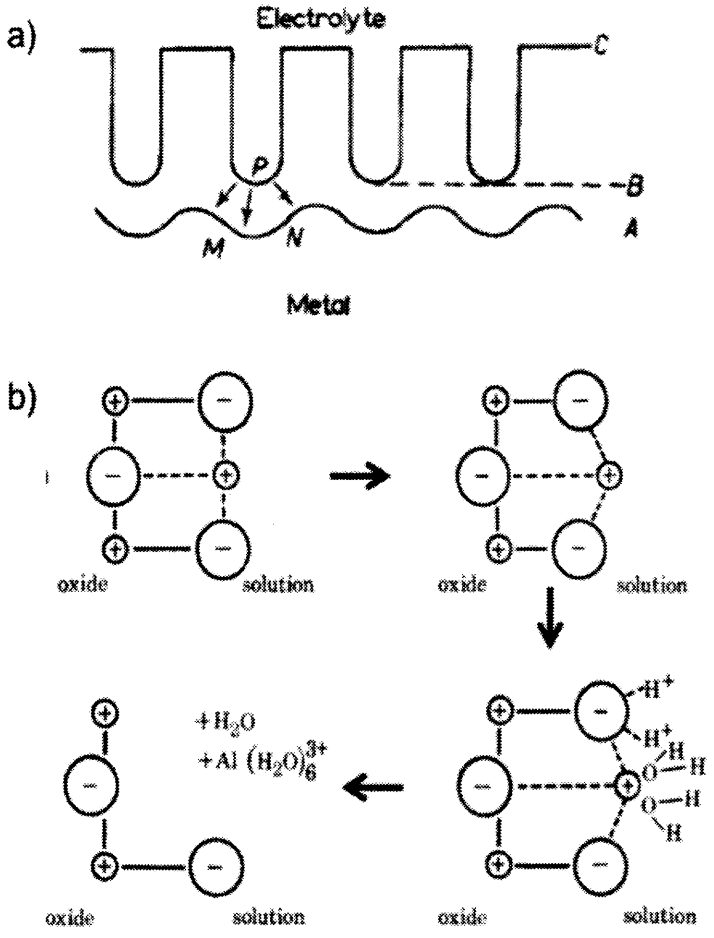


**Figure 1-7.** Schematics of field-assisted dissolution mechanism (a) by Mott and Hoar [11] and (b) O'Sullivan and Wood [12].

Unfortunately, Friedman et al. systemically showed that none of the theoretical models are consistent with experimental results [32]. While the models predicted a linear

relationship between pore spacing and the anodic voltage, they showed that the models do not fit the experimental data. More importantly, the predicted behaviors (pore spacing and pore diameter) as a function of pH from the models show large discrepancy with the experimental results.

This discrepancy originates from the fact that there is very limited information on the kinetics of the field-assisted dissolution of the oxide. Indeed, O'Sullivan and Wood [12] stated that 'until it is possible to measure field-assisted dissolution rates on plane surfaces as a function of the field, in the absence and presence of Joule heating, it does not seem possible to calculate further the interplay of film formation and film dissolution at the pore bases.' Diggle et al. measured the time required for re-establishment of a steady-state observed in capacitance-voltage curves for porous oxide growth by suddenly lowering the anodic voltage from 10 and 15V to 5 V in sulfuric acid, and indirectly observed an enhanced dissolution rate of the oxide without growth of the oxide [33]. *However, to best knowledge of the author, the field enhanced dissolution rate of the oxide has never been determined on planar surfaces as a function of the field, in isolation.*

### 1.4.2 $Al^{3+}$ Direct Ejection Model

While porosity of typical anodic films formed in an acid solution is 10 ~ 20%, the current efficiency at the same anodic conditions is about 60%. This implies that an additional oxide dissolution process takes places during anodization. Cherki and Siejka showed that the growing oxide layer is formed only at the m/o interface by oxygen ion transport, using an $O^{18}$ nuclear isotope experiment [28]. They proposed that the lower

current efficiency originates from direct dissolution of aluminum cations into the solutions. They also determined from the nuclear isotope study that the anodic oxide grows only at the m/o interface by $O^{2-}$ transport.

Later, Siejka and Ortega observed that enhanced oxygen ion loss at the pore base into the solutions does not occur during pore initiation, from an $O^{18}$ nuclear isotope experiment, which is contradictory to the field-assisted dissolution model [29]. They argued that pore formation consists of an oxide decomposition process involving only cation transfer into solutions. Therefore, reactions (10) and (12) occur and the overall reaction becomes

$$Al_m = Al^{3+}_{(aq)} + 3e^- . \quad (14)$$

This overall reaction is called $Al^{3+}$ direct ejection [17, 26]. It must be noted that while the direct ejection of Al ions model is not directly related to pore formation, it is generally believed as a necessary condition for porous oxide formation [17, 34]. In other word, any initiated pores would be healed without the $Al^{3+}$ direct ejection mechanism due to preferential formation of $Al_2O_3$ at the o/e interface because of the high E-field at the initiated pore bases.

### 1.4.3 Field-Assisted Plastic Flow Model

Recently, the Manchester group led by Prof. G. E. Thompson rejected the field-assisted dissolution model and proposed a field-assisted plastic flow model for pore formation in a steady-state [35]. In this model, they suggested that steady-state growth of pores is maintained by plastic flow of the film under growth stresses during anodization

in acidic electrolytes. To confirm their theory, they performed a tungsten tracer study to visualize details of mass transport in the porous oxide films, using transmission electron microscopy (TEM) [13, 36]. As shown in Fig. 1-8 (a), they introduced a thin layer of tungsten tracer in the middle of an Al substrate and anodized the substrate. The W tracer entered the oxide in the form of $WO_3$ as anodization was continued. Tungsten was chosen as a tracer because of its high atomic mass, which facilitates observation in TEM, and slow cation mobility (~ 0.3 times of $Al^{3+}$ mobility). From the distribution of the W tracer in the scalloped barrier layer, they argued that the mechanisms of pore formation could be determined as illustrated in Fig. 1-8 (b). If pores are formed by field-assisted dissolution of the oxide, tungsten tracer at the pore base should lie ahead of the tungsten at the cell boundary, due to outward migration of the ions driven by the concentrated E-field at the pore base [37].

TEM images of the porous film formed in phosphoric acid shows an inverted distribution, contrary to expectations based on the field-assisted dissolution model, as depicted in Fig. 1-8 (c) [13]. From the distortion of the tracer distribution in the porous film, they concluded that the pores are created mainly by flow of materials from the pore bases to the cell walls in phosphoric acid. Fig. 1-8 (d) illustrates motion of the oxide flow during anodization. Through a series of W tracer studies in various electrolytes, Thompson et al also concluded that steady state growth of pores proceeds by plastic flow of the oxide in sulfuric acid [38], and by field-assisted dissolution of the oxide in chromic acid [39] and in alkaline solutions [37].

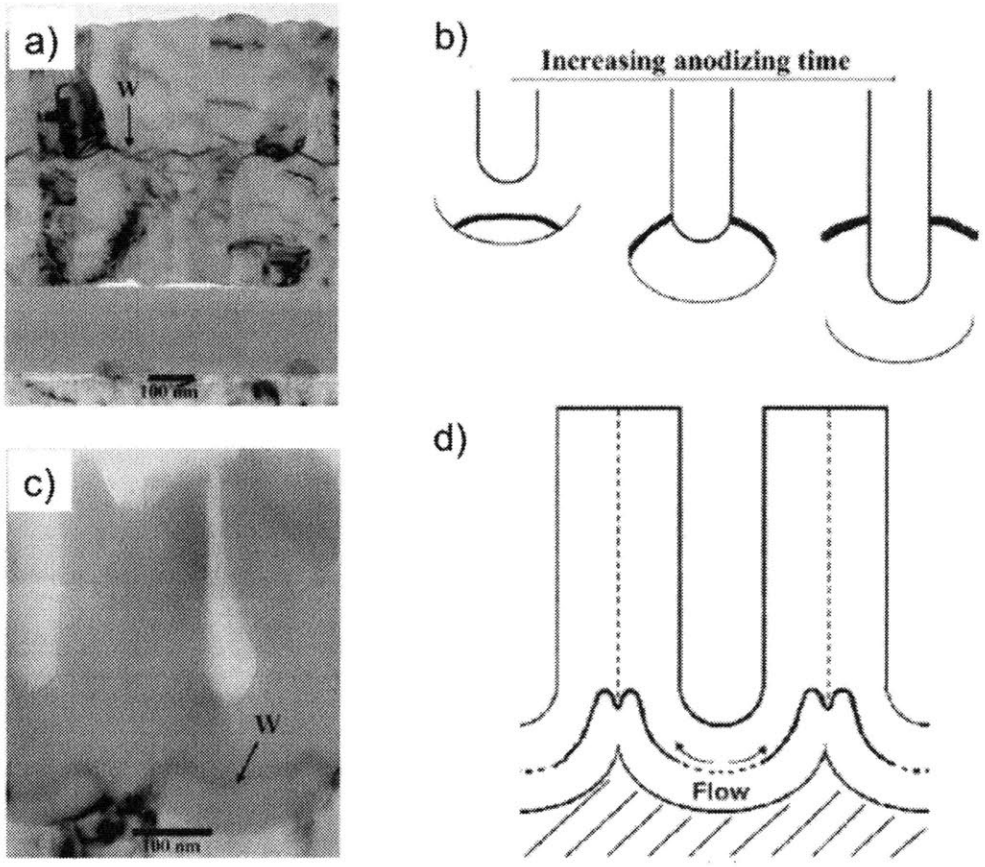


**Figure 1-8.** TEM images of aluminum with a W tracer (a) before and (c) after anodization in 0.4 M phosphoric acid at 5 mA/cm$^2$ [13]. Proposed distribution of the W tracer by (b) field-assisted dissolution mechanism [37] and by (d) plastic flow mechanism [35].

Computational modeling of the plastic flow model by Houser and Hebert [40] soon followed. In the model, they assumed that the volume of the porous AAO is not lost in a steady-state and that the oxide behaves as a Newtonian fluid, following a viscous creep model, under anodization conditions. They then enforced uniform interface motion at the m/o and o/e interface from the geometry of the steady-state pore structure. From

those assumptions (volume conservation, room temperature viscous flow and uniform interface motion of the oxide), they successfully matched simulated W tracer motion to the experimental results by the Manchester group. However, it must be noted that they did not include stress as a driving force for migration and they also did not include the impact of the volume expansion stress at the $Al/Al_2O_3$ interface on the flow of the oxide. Instead, they concluded that the oxide flow arises at the o/e interface at the pore base due to compressive stress and they also suggested that the compressive stress originates from competition of strong anion adsorption with deposition of oxygen.

However, a close examination of the boundary conditions used in the model reveals that the origin of the oxide flow is, in fact, volume expansion due to Al oxidation at the o/e interface. For example, the boundary condition at the o/e interface was given by

$$v_I \cdot n = \left(\frac{\eta \overline{V}_O}{2F} i + \overline{V}_O J_O + v\right) \cdot n, \tag{15}$$

where $v_I$ is the uniform interface velocity, $\eta$ is the current efficiency, $F$ is the Faraday constant, i is the anodic current density, $\overline{V}_O$ is the molar volume of $O^{2-}$ ions in alumina, Jo is the $O^{2-}$ transport flux, and v is the creep velocity, respectively. Note that $\overline{V}_O$ is, in fact, the molar volume of the alumina since the volume of $O^{2-}$ consists 98.6% of volume of alumina. According to Houser and Hebert, the first term on the right is the deposition rate of $O^{2-}$ ions and the second and third terms represent $O^{2-}$ migration flux and the volume flow, respectively. The boundary condition at the m/o interface, on the other hand, was given by

$$v_I \cdot n = \frac{\Omega_M}{3F} i \cdot n = (\overline{V}_O J_O + v) \cdot n. \tag{16}$$

Here, $\Omega_M$ is the molar volume of Al metal. By comparing Eq. (15) and (16), it becomes obvious that new volume of alumina is generating at the o/e interface by so-called $O^{2-}$ deposition from water electrolysis. However, the boundary conditions are clearly inconsistent with $O^{18}$ isotope studies and do not satisfy the necessary conditions for pore formation, which are described in earlier in this chapter.

The deposition of $O^{2-}$ at the o/e interface does not necessarily increase the volume of alumina, depending on the type of charge carriers in the oxide. The most likely charge carrier for $O^{2-}$ in anodic oxide is thought to be oxygen ion vacancies [20]. In this case, the volume of the oxide is generated at the metal/oxide interface by creating oxygen vacancies and no significant volume expansion is expected at the oxide/electrolyte interface, because the $O^{2-}$ transferred to the o/e interface from water just occupies the oxygen vacancy at the same interface. Therefore, the charge carrier in the anodic Al oxide must be determined to provide a precise theoretical model for the field-assisted plastic flow model.

It also must be noted that a tracer study alone can not verify the plastic flow of the oxide nor can it disprove the field-assisted dissolution of the oxide. For example, the Manchester group also conducted Nd and Hf tracer studies in phosphoric acid and found that the distribution of the Nd and Hf tracer is the exactly the same as that of the W tracer in the alkaline solution [41, 42]. According to Fig. 1-8 (b), such a distribution of a tracer indicates that pore forms by field-assisted dissolution of the oxide. Instead, they attributed this unexpected distribution of the Nd and Hf tracer to the dissolution of the tracer to the phosphoric acid by fast cation migration through the oxide, still arguing that

porosity forms by the plastic flow of the oxide based on the W tracer study. However, this result indicates that only W tracers in specific electrolytes show evidence of oxide flow. *Therefore, supportive experimental evidence other than W tracer studies is required to verify the oxide flow model and to determine whether field-assisted dissolution of the oxide occurs during anodization.*

### 1.4.4 Pore Initiation Mechanisms

It is well-known that pores are initiated by roughening of the o/e interface during anodization, as shown in Fig. 1-6 [17, 26]. At valleys of the o/e interface, the E-field is concentrated, and pores can grow either by field-assisted dissolution or by field-assisted plastic flow of the oxide. However, very few studies have been conducted on what causes the initial roughening of the o/e interface to form a periodic pattern [17, 23, 26]. For example, Krishnan proposed that tensile stress from Al vacancy formation causes the initial roughening at the Al/oxide interface due to a strain-induced instability, which is, however, inconsistent with previous experimental observations [23]. On the other hand, Raja et al. also proposed a strain-induced instability at the o/e interface to explain pore formation in anodic $TiO_2$ [43]. However, they did not provide any supportive evidence. Therefore, more systematic study is required to understand the pore initiation mechanism at the o/e interface.

## 1.5 Ordered Anodic Aluminum Oxide Films

### 1.5.1 Self-Ordering Anodization Conditions

*Mild and Hard Anodization*

While the structure of porous AAO has been modeled as a hexagonally close packed cellular structure since its first SEM observation, it was only after about 50 years that Masuda and Fukuda first discovered in 1995 that pores self-organized into the ideal honeycomb structure at the Al/AAO interface, but only after prolonged anodization (~ 160 hrs) in 0.3 M oxalic acid at 0°C with application of a constant voltage of 40V [6]. In the work of Masuda and Fukuda, domains of hexagonally closed-packed pores form with a pore spacing, $D_s$, of about 100 nm. Soon after this discovery, other anodization conditions that lead to formation of self-ordered porous structures with various $D_s$ have been extensively sought [44-47]. As a result, anodization conditions for self-ordered AAO with $D_s$ = 50, 65, 100, 420, and 500 nm have been found after anodizing Al foil for extended anodization time, typically > 10 hrs, in sulfuric acid at $V_{an}$ = 19 and 25V, in oxalic acid at $V_{an}$ = 40V, and in phosphoric acid at $V_{an}$ = 160 and 195V, respectively. These conditions have been called self-ordering anodization regime in mild anodization conditions.

Recently, new anodization conditions that lead to self-ordering in AAO with $D_s$ from 90 ~ 140 nm and 220 ~ 300 nm were discovered [48-52]. These anodization conditions were called high-field anodization by Chu et al. and One et al., or hard anodization by Lee et al. Fig. 1-9 summarizes self-ordering voltages and corresponding values of $D_s$ in the mild and hard anodization conditions. Hard anodization usually involves very high current densities, typically > 100 mA/cm$^2$, and results in very fast growth rates, > 50 μm/hr. However, it suffers from extensive heat generation and fracture

of the oxide, which prevents stable anodization and ideal ordering of pores. To avoid such side effects, aging of electrolytes or pre-treatment of the Al by forming a pre-oxide layer of ~ 400 nm is required. For example, Chu et al reported that formation of domains of self-ordered pores with $D_s$ = 90 ~ 140 nm, using aged sulfuric acid at 40 ~ 70V [48]. Interestingly, when the anodic voltage is further increased to $V_{an}$ = 70V, $Al_2O_3$ nanotubes form instead of porous $Al_2O_3$. Lee et al. systemized stable hard anodization using the pre-anodizing technique and demonstrated self-ordering of pores with $D_s$ = 220 ~ 300 nm with application of a constant voltage from 120 ~ 150 V using 0.3M oxalic acid at 1°C [49]. Similarly, the self-anodization conditions in other electrolytes, such as citiric, malonic, and tartaric acid were also found using hard anodization [51-53]. It should be noted that the proportionality factor $\xi_{int}$ in hard anodization is about 2.0 nm/V while $\xi_{int}$ in mild anodization is about 2.5 nm/V. In addition, $D_s$ increases as the current density drops for an initial 30 min at 140V, indicating the anodizing current density is also an important parameter for obtaining self-ordered pores in hard anodization [49]. Interestingly, Schwirn et al. discovered spontaneous modulation of pore diameters at $V_{an}$ = 27 ~ 32V during an $H_2SO_4$ hard anodization process [54].

Recent advances in anodization of Al using high anodic voltage/high electric field have allowed exploitation of self-ordered nanoporous AAO using unconventional electrolytes, namely acidic organic electrolytes [55-57]. Notably, Li et al. used mixtures of ethanol and various acids (phosphoric, oxalic, sulfuric acid) in water as electrolytes to increase the anodic current density but maintain $V_{an}$ at the self-ordering conditions, i.e. 195V in phosphoric acid [56, 57]. As result, they achieved self-ordered AAO with a

growth rate of 240 ~ 600 μm/hr. They also found that the $D_s$ is dependent not only of the anodic voltage but also of the anodic current density.

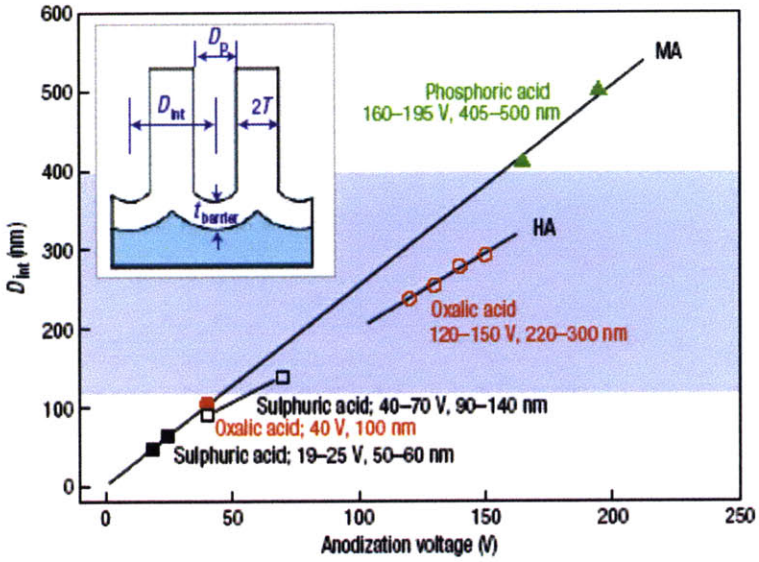


**Figure 1-9.** Summary of self-ordering voltages and the $D_s$ in various anodization conditions [49].

***Self-Ordering under Galvanostatic Conditions***

It is widely believed that self-ordering of pores occurs only in potentiostatic mode (constant voltage), since the pore spacing is directly dependent on the anodic voltage. Recently, however, Zhao et al. demonstrated that self-ordered porous AAO can be formed under galvanostatic conditions of 160 mA/cm$^2$ using mixture of $H_2SO_4$ and $Al_2(SO_4)_3$ as a electrolyte at 1°C [58]. In addition, they also showed that additional pores can be opened at the triple cell junctions of the hexagonally closed packed pores after treatment of the AAO in HCl/$CuCl_2$ solutions, as shown in Figure 1-10 (a). Lee et al. also

showed self-ordering of pores using concentrated sulfuric acid [59]. By switching to a constant voltage mode after establishment of pore ordering in the galvanostatic mode, they further showed that domains with two different $D_s$, 120 and 160 nm, co-exist, as illustrated in Fig. 1-10 (b). However, process parameters and mechanisms leading to the pore ordering under galvanostatic conditions are not well-established in detail.

***Domain Structures***

The self-ordered porous AAO forms multi-domains of hexagonally closed packed pore arrays with different in-plane orientations. One of the most important parameter that controls the domain size of the self-ordered porous AAO is the quantity of the reacted Al or the formed $Al_2O_3$, not the anodization time, in the self-ordering anodization regime. The anodization time for self-ordering at the metal/oxide interface can be reduced by increasing the rate of the AAO formation through increasing the concentration of the electrolytes or temperature. For example, Masuda himself reduced the anodization time from 160 h to 10 h by increasing temperature from 0 to 17°C to increase the growth rate of the AAO in 0.3 M oxalic acid at 40V [6, 60]. Li et al. quantitatively showed that the domain size of the self-ordered AAO linearly increases as a function of the anodization time and temperature. For example, domains of area ~ 1 $\mu m^2$ can be achieved after 1 h at 15°C while 4 h is required at 0°C in 0.3M oxalic acid at 40V [61]. On the other hand, Nielsch et al. showed that there appears to be an optimum anodization time to achieve a maximum domain area; the domain size increased to about 17 $\mu m^2$ until 24 h, then the size of the domains decreased for further anodization in anodization condition for AAO with $D_s$ = 500 nm, i.e., 1% phosphoric acid at 195V [62]. However, effects of varied

anodization conditions, such as electrolyte concentration and temperature, on domain structures as a function of time are still uninvestigated.

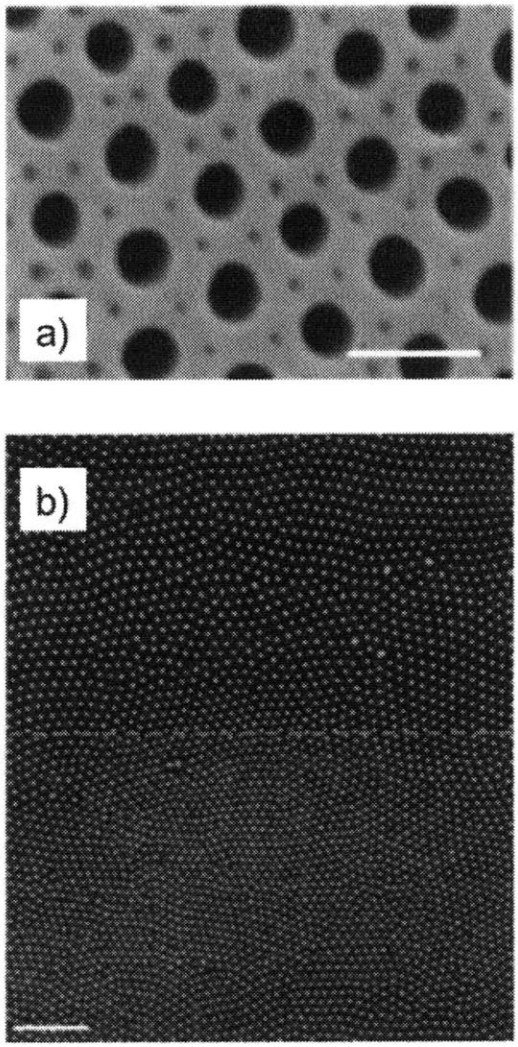


**Figure 1-10.** (a) SEM image of AAO with small pores at the cell junction [58]. Scale bar = 100 nm. (b) TEM image of AAO with domains with different $D_s$ [59]. Scale bar = 1 μm.

### 1.5.2 Highly Ordered Anodic Aluminum Oxide

*Two-step Anodization Process*

As described earlier, domains of self-ordered pores only form at the m/o interface as AAO grows after prolonged anodization times in specific self-ordering anodization regimes. However, the pores at the top surface of AAO remain disordered, indicating that many pores at the top surface do not run through to the bottom surface. In order to fabricate ordered AAO with straight pores, Masuda demonstrated a two-step anodization process [60]. In the two-step anodization process, anodization is first carried for a long time to form ordered arrays of pores at the m/o interface, and then the AAO is selectively removed. As a result, the Al surface has ordered dimples, a replica of the ordered pores at the bottom of the removed porous alumina. This Al nano-pattern then guides the initiation of pore formation in a second anodization which is usually carried out under the same conditions as the first anodization. Using this technique, Masuda was able to fabricate thin, ordered AAO membranes for shadow mask deposition of Au dots. The two-step anodization process has subsequently become a standard procedure for creation of locally ordered AAO scaffolds.

***Lithographically Guided Anodization Process – Templated Porous AAO***

When bi-periodic dimples are patterned on an Al surface using nano-lithographic techniques, monodomain ordered AAO can be created by anodizing the pre-patterned Al with application of a constant anodization voltage from which the expected pore spacing matches to the period of the dimples, i.e. $V_{an} \sim D_s/\xi_{int}$. Like the two-step anodization process, the dimples on the Al surface guide the initiation of pore formation and the

process is called templated anodization. The templated anodization process does not require a thick Al foil for self-ordering of pores, which is vital in the two-step anodization process, and therefore, can be used to form ordered AAO from thin films of Al on a substrate.

Masuda et al. first demonstrated fabrication of monodomains of ideally ordered porous AAO by creating hexagonally ordered dimples on Al by nano-imprint lithography before anodization [63]. Fig. 1-11 (a) and (b) show a schematic of the two-step and templated anodization processes. With advances in nanotechnology, various lithography technologies have been used to pattern bi-periodic dimples on Al surfaces. For instance, various nano-lithographic technique, including nano-imprint lithography using different masters [64-66], e-beam lithography [67], interference lithography [68-70], and block-copolymer lithography [71], have been used to create periodic dimples on Al surfaces.

Templated anodization has unique features in porous AAO formations. Monodomain ordered AAO can be achieved with a wider range of pore spacings and with pore geometries other than hexagonally closed packed. For example, Choi et al. fabricated ordered AAO with moiré patterns by anodizing Al substrates with moiré patterns and by nano-indenting the Al surface twice by rotating a master with a hexagonal pattern [72]. Asoh et al. [73] and Masuda et al. [74] demonstrated fabrication of an ordered AAO with square cells by anodizing Al surface-patterned with a SiC mold with square symmetry. Krishnan et al. fabricated ordered AAO with hexagonal and square symmetries [70]. They further demonstrated that templated anodization allows

independent control of pore diameter and pore spacing using mild and hard anodization, as shown in Fig. 1-12.

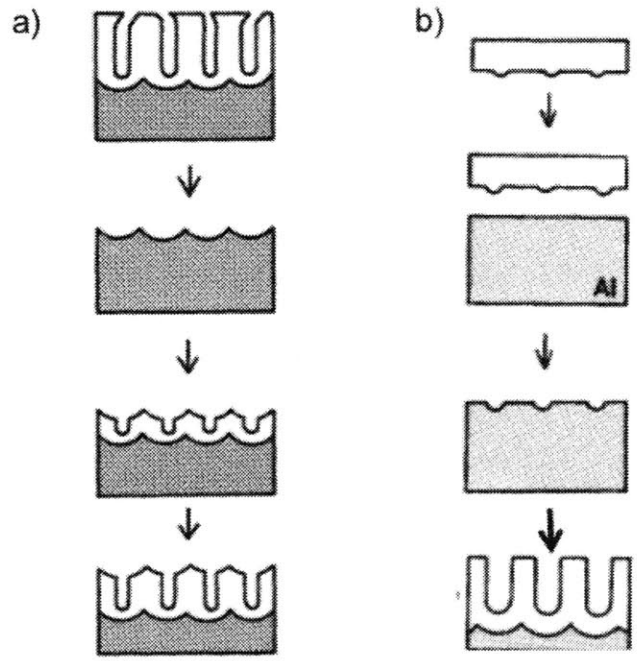


**Figure 1-11.** Schematic of (a) the two-step anodization process [60] and (b) templated anodization processes [63].

***Structural Engineering of Ordered AAO***

Independent control of pore spacing and pore diameter also enables modification of the pore structure of the templated AAO [49, 70]. For example, Krishnan and Thompson fabricated ordered AAO with modulated pore diameter by switching the electrolyte for mild anodization ($H_3PO_4$) from that for hard anodization (oxalic acid) [70]. Similar pore structures can also be fabricated by changing the anodic voltage in a fixed electrolyte. In

this case, the fabrication process can be automated. Lee et al. demonstrated the use of pulse anodization to fabricate AAO with modulated pore diameters, without changing electrolytes [75]. Fig. 1-13 shows a schematic for the pulse anodization process as well as fabricated pore structures. Losic et al. also used a similar technique, i.e., cyclic modulation of the anodic voltage, to form modulated porous structures [76].

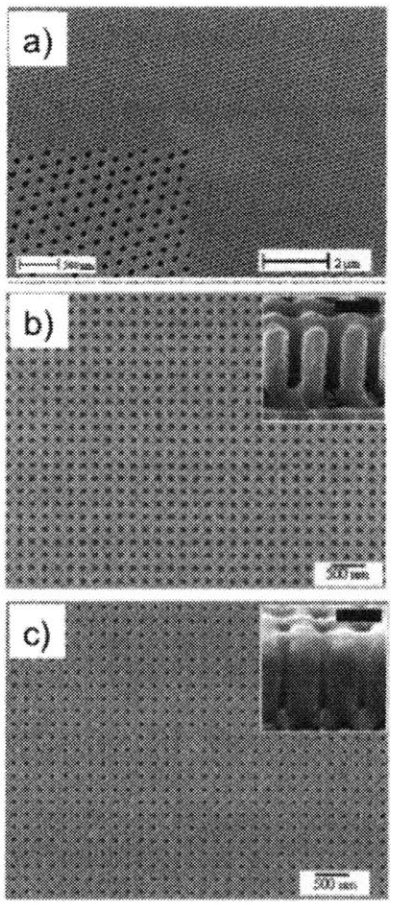


**Figure 1-12.** SEM images of templated AAO arrays with (a) hexagonal, and (b) and (c) square symmetry. Pore diameter is ~ 80 nm in (a) and (b), and ~ 30 in (c), respectively. The scale bars in the inset are 200 nm [70].

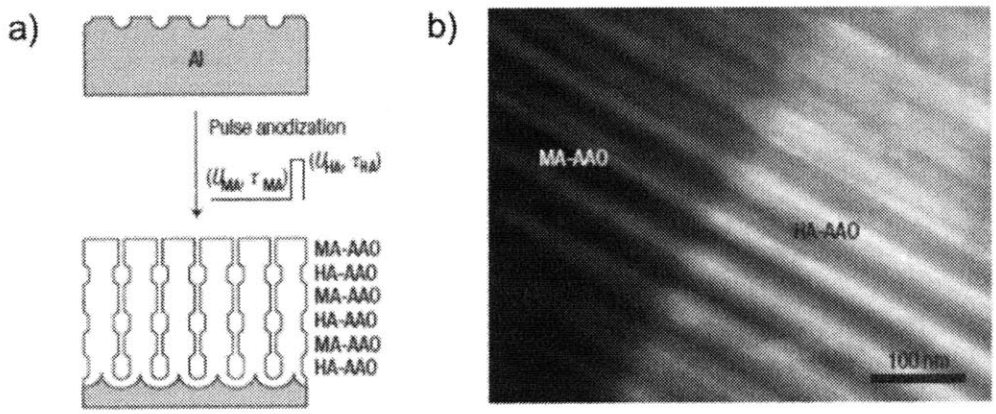


**Figure 1-13.** (a) Schematic of pulse anodization process. (b) TEM image of AAO with modulated pore diameter [75].

### 1.5.3 Thin Film AAO and Barrier Perforation

Thin-Films of highly ordered AAO can be formed on a substrate to serve as a scaffold for growth of low-dimensional materials, such as nanowires and nanotubes. To incorporate low-dimensional nanomaterials into devices on a substrate, electrical contact should be made at both the top and bottom of the porous AAO. However, the bottom of the as-anodized AAO is electrically isolated from the substrate by an aluminum oxide barrier layer, as discussed earlier in this chapter. An additional process is required to remove the barrier layer and to expose the substrate surface at the pore bottom. Typically, the barrier layer is removed using a chemical etching process with phosphoric acid and results in a significant widening of the pores that makes it difficult to provide scaffolds for small-diameter 1-D nanomaterials [77, 78]. So far, few techniques have been proposed for selective removal the barrier layer but their use is limited by the need for specific anodization conditions or specific choices of a substrates [79, 80]. *Therefore, a*

*new process for selective perforation of the barrier layer is required for use over a wide range of anodization conditions and on various substrates.*

### 1.5.4 Horizontal Porous Aluminum Oxide

Thin film horizontal AAO scaffolds have also been fabricated on substrates [81-84]. Masuda et al. were first to propose a side anodization process to fabricate mono- and double layers of horizontal pores in AAO with $D_s \sim 200$ nm, by anodizing vertical Al sidewalls of 200 and 400 nm thickness, prepared by cleaving $Al_2O_3$/Al/glass structures, as shown in Fig. 1-14 [81].

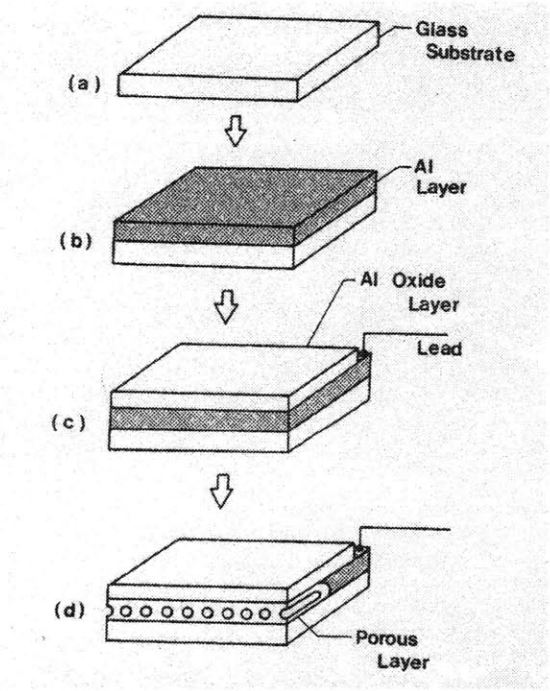


**Figure 1-14.** Schematic of a side anodization process for fabrication of a horizontal AAO array on a substrate [81].

Recently, Cojocaru et al. also fabricated horizontal AAOs with multilayers of pores with $D_s < 50$ nm on $SiO_2$ substrates [82]. In previous reports, however, anodization to form lateral pores has been performed only for very short times (5~10 min), resulting in lateral pores with low aspect ratios (<10:1) and poor ordering. *Therefore, to achieve highly ordered lateral pore arrays, horizontal anodization for extended times under self-ordering anodization conditions is required.*

## 1. 6 Thesis Objectives

The objective of this thesis is to provide a quantitative understanding of pore formation mechanisms and self-ordering behavior in Al anodization. This includes devising a new experimental procedure to separately reveal underlying physical phenomena that govern the growth mechanisms.

I also explore pathways for utilization nanostructured AAO films for assembly of ordered arrays of low-dimensional materials with controlled diameter, spacing, and orientation on a desirable substrate. For the controlled synthesis of low-dimensional materials, it is required that a process that allows perforation of the insulating barrier oxide without modifying the porous structure of as-grown AAO films be developed for use on any substrate. In order to control of the orientation of pores, we also investigate a side anodization processes to fabricate horizontal porous AAO thin films on a substrate.

## 1.7 Thesis Outline

In chapter 2, we report a mechanistic study of pore formation during Al anodization. We exploit a new anodization process, called discontinuous anodization, to decouple interface motion at the m/o and o/e interfaces as a function of the E-field. From discontinuous anodization, we show that field-assisted dissolution models are consistent with the observed dependence of the $Al_2O_3$ dissolution rate on the electric field, as well as the existence of a critical field for pore initiation. However, we further show that the well-known ordered porous structure that as been widely studied is the result of a strain-induced instability with forced plastic deformation and flow of the oxide during further anodization. We also show that mechanical confinement of anodizing Al results in a dendritic pore structure. Through interpretation of these results, we develop a generalized mechanism for ordered pore formation in AAO, in analogy with cellular growth during solidification.

In chapter 3, we report abnormal behavior in anodic oxidation of Al in mechanically confined structures used for formation of horizontal anodic alumina oxide, H-AAO. We show that side anodization for H-AAO results in formation of periodic dendrite inner pore structures and a reduction of the growth rate. I demonstrate that these anomalies associated with H-AAO originate from suppressed volume expansion and plastic flow of the $Al_2O_3$ confined by the $SiO_2$ hard mask. I further present a new anodization conditions that lead to zero volume expansion avoid dendritic H-AAO and kinetic retardation.

In chapter 4, I report development of a selective barrier perforation process based on anodization of Al/W bilayer films on substrates. We show that $WO_3$ forms and penetrates the barrier layer of AAO. Based on thermodynamic calculation of the solubility of $Al_2O_3$ and $WO_3$ in water, I successfully remove penetrated $WO_3$ and exposed the metallic W surface at the base of the pores, without changing the as-anodized pore structure. Application of this technique was demonstrated, used with templated pore formation, by creation of Ni nano-electrode arrays with fixed electrode spacings but varied electrode diameters.

In chapter 5, I report a W interlayer process for fabrication of a through-pore AAO scaffold on any substrate (AS). I demonstrate fabrication of through-pore AAOs on a variety of substrates for various anodization conditions, without changing the pore diameter. This is done through determination of the thickness of the W interlayer in the Al/W/AS tri-layer that will allow complete removal of W metal (through oxidation and selective removal) at the bottom of the pores. With this W interlayer process, I fabricated vertically aligned free-standing Au and Pt nanowires with diameters ranging from about 12 nm to about 120 nm using electrodeposition on an Au substrate.

Finally, chapter 6 contains a summary of the results of the previous chapters. This chapter also includes suggestions for future research.

## References


1. Diggle, J.W., T.C. Downie, and C.W. Goulding, *Anodic oxide films on aluminum*. Chemical Reviews, 1969. **69**(3): p. 365-405.
2. Despic, A.P., V. P., *Modern aspects of electrochemistry*, ed. J.O.M.W. Bockris, R. E.; Conway, B. E. Vol. 20. 1989, New York: Plenum Press.
3. Young, L., *Anodic oxide films*. 1961, New York: Academic Press.
4. *Corrosion; Aqueous Processes and Passive Films*. Treatise on Materials Science and Technology, ed. J.C. Scully. 1983, New York: Academic Press.
5. Keller, F., M.S. Hunter, and D.L. Robinson, *Structural Features of Oxide Coatings on Aluminum*. Journal of the Electrochemical Society, 1953. **100**(9): p. 411-419.
6. Masuda, H. and K. Fukuda, *Ordered Metal Nanohole Arrays Made by a 2-Step Replication of Honeycomb Structures of Anodic Alumina*. Science, 1995. **268**(5216): p. 1466-1468.
7. Xia, Y.N., et al., *One-dimensional nanostructures: Synthesis, characterization, and applications*. Advanced Materials, 2003. **15**(5): p. 353-389.
8. Martin, C.R., *NANOMATERIALS - A MEMBRANE-BASED SYNTHETIC APPROACH*. Science, 1994. **266**(5193): p. 1961-1966.
9. Bhushan, B., ed. *Springer hnadbook of nanotechnology*. 2004, Springer-Verlag: Heidelbert. 99 - 145.
10. Kline, T.R., et al., *Template-grown metal nanowires*. Inorganic Chemistry, 2006. **45**(19): p. 7555-7565.

11. Hoar, T.P. and N.F. Mott, *A mechanism for the formation of porous anodic oxide films on aluminium*. Journal of Physics and Chemistry of Solids, 1959. **9**(2): p. 97-99.

12. O'Sullivan, J.P. and G.C. Wood, *The Morphology and Mechanism of Formation of Porous Anodic Films on Aluminium*. Proceedings of the Royal Society of London. A. Mathematical and Physical Sciences, 1970. **317**(1531): p. 511-543.

13. Garcia-Vergara, S.J., et al., *A flow model of porous anodic film growth on aluminium*. Electrochimica Acta, 2006. **52**(2): p. 681-687.

14. Pourbaix, M., *Atlas of electrochemical equilibria in aqueous solution*. 1974, Houston: National Association of Corrosion Engineers.

15. Available from: http://www.crct.polymtl.ca/ephweb.php.

16. Davies, J.A., et al., J. Electrochem. Soc., 1965. **112**: p. 675-680.

17. Thompson, G.E., Thin Solid Films, 1997. **29**: p. 192-201.

18. Shimizu, K., et al., *Direct Observations of Ion-Implanted Xenon Marker Layers in Anodic Barrier Films on Aluminum*. Thin Solid Films, 1982. **88**(3): p. 255-262.

19. Shimizu, K., et al., *A Novel Marker for the Determination of Transport Numbers during Anodic Barrier Oxide-Growth on Aluminum*. Philosophical Magazine B-Physics of Condensed Matter Statistical Mechanics Electronic Optical and Magnetic Properties, 1991. **64**(3): p. 345-353.

20. Macdonald, D.D., *The Point-Defect Model for the Passive State*. Journal of the Electrochemical Society, 1992. **139**(12): p. 3434-3449.

21. Lohrengel, M.M., *THIN ANODIC OXIDE LAYERS ON ALUMINUM AND OTHER VALVE METALS - HIGH-FIELD REGIME*. Materials Science & Engineering R-Reports, 1993. **11**(6): p. 243-294.

22. Zhang, L., et al., *On the kinetics of growth of anodic oxide firms*. Journal of the Electrochemical Society, 1998. **145**(3): p. 898-905.

23. Krishnan, R., *Templated self-assembly of nanoporous alumina: pore formation and ordering mechanisms, methodologies, and applications*, in *Department of Materials Science and Engineering*. 2005, MIT: Cambridge.

24. Parkhutik, V.P. and V.I. Shershulsky, *Theoretical Modeling of Porous Oxide-Growth on Aluminum*. Journal of Physics D-Applied Physics, 1992. **25**(8): p. 1258-1263.

25. Houser, J.E. and K.R. Hebert, *Modeling the potential distribution in porous anodic alumina films during steady-state growth*. Journal of the Electrochemical Society, 2006. **153**(12): p. B566-B573.

26. Thompson, G.E., et al., *Nucleation and Growth of Porous Anodic Films on Aluminum*. Nature, 1978. **272**(5652): p. 433-435.

27. Hunter, M.S. and P. Fowle, *Factors Affecting the Formation of Anodic Oxide Coatings*. Journal of the Electrochemical Society, 1954. **101**(10): p. 514-519.

28. Cherki, C. and J. Siejka, *Study by Nuclear Microanalysis and O[sup 18] Tracer Techniques of the Oxygen Transport Processes and the Growth Laws for Porous Anodic Oxide Layers on Aluminum*. Journal of the Electrochemical Society, 1973. **120**(6): p. 784-791.

29. Siejka, J. and C. Ortega, *An O[sup 18] Study of Field-Assisted Pore Formation in Compact Anodic Oxide Films on Aluminum*. Journal of the Electrochemical Society, 1977. **124**(6): p. 883-891.

30. Thamida, S.K. and H.C. Chang, *Nanoscale pore formation dynamics during aluminum anodization*. Chaos, 2002. **12**(1): p. 240-251.

31. Singh, G.K., A.A. Golovin, and I.S. Aranson, *Formation of self-organized nanoscale porous structures in anodic aluminum oxide*. Physical Review B, 2006. **73**(20): p. 205422.

32. Friedman, A.L., D. Brittain, and L. Menon, *Roles of pH and acid type in the anodic growth of porous alumina*. Journal of Chemical Physics, 2007. **127**(15): p. 154717.

33. Diggle, J.W., T.C. Downie, and C.W. Goulding, *Processes Involved in Reattainment of Steady-State Conditions for Anodizing of Aluminum Following Formation Voltage Changes*. Journal of the Electrochemical Society, 1969. **116**(6): p. 737-740.

34. Shimizu, K., R.S. Alwitt, and Y. Liu, *Cellular porous anodic alumina grown in neutral organic electrolyte II. Transmission electron microscopy examination of ultrathin cross sections and a model for film growth*. Journal of the Electrochemical Society, 2000. **147**(4): p. 1388-1392.

35. Garcia-Vergarai, S.J., et al., *Mechanical instability and pore generation in anodic alumina*. Proceedings of the Royal Society a-Mathematical Physical and Engineering Sciences, 2006. **462**(2072): p. 2345-2358.

36. Skeldon, P., et al., *A tracer study of porous anodic alumina*. Electrochemical and Solid State Letters, 2006. **9**(11): p. B47-B51.

37. Garcia-Vergara, S.J., et al., *Formation of porous anodic alumina in alkaline borate electrolyte*. Thin Solid Films, 2007. **515**(13): p. 5418-5423.

38. Garcia-Vergara, S.J., et al., *Stress generated porosity in anodic alumina formed in sulphuric acid electrolyte*. Corrosion Science, 2007. **49**(10): p. 3772-3782.

39. Garcia-Vergara, S.J., et al., *A tracer investigation of chromic acid anodizing of aluminium*. Surface and Interface Analysis, 2007. **39**(11): p. 860-864.

40. Houser, J.E. and K.R. Hebert, *The role of viscous flow of oxide in the growth of self-ordered porous anodic alumina films*. Nat Mater, 2009. **8**(5): p. 415-420.

41. Garcia-Vergara, S.J., et al., *Behaviour of a fast migrating cation species in porous anodic alumina*. Corrosion Science, 2008. **50**(11): p. 3179-3184.

42. Garcia-Vergara, S.J., et al., *Growth of porous anodic films on sputtering-deposited aluminium incorporating Al-Hf alloy nanolayers*. Electrochimica Acta, 2009. **54**(13): p. 3662-3670.

43. Raja, K.S., M. Misra, and K. Paramguru, *Formation of self-ordered nano-tubular structure of anodic oxide layer on titanium*. Electrochimica Acta, 2005. **51**(1): p. 154-165.

44. Li, A.P., et al., *Hexagonal pore arrays with a 50-420 nm interpore distance formed by self-organization in anodic alumina*. Journal of Applied Physics, 1998. **84**(11): p. 6023-6026.

45. Masuda, H., F. Hasegwa, and S. Ono, *Self-ordering of cell arrangement of anodic porous alumina formed in sulfuric acid solution*. Journal of the Electrochemical Society, 1997. **144**(5): p. L127-L130.

46. Jessensky, O., F. Müller, and U. Gösele, *Self-organized formation of hexagonal pore structures in anodic alumina*. Journal of the Electrochemical Society, 1998. **145**(11): p. 3735-3740.

47. Masuda, H., K. Yada, and A. Osaka, *Self-ordering of cell configuration of anodic porous alumina with large-size pores in phosphoric acid solution*. Japanese Journal of Applied Physics Part 2-Letters, 1998. **37**(11A): p. L1340-L1342.

48. Chu, S.Z., et al., *Fabrication of ideally ordered nanoporous alumina films and integrated alumina nanotubule arrays by high-field anodization*. Advanced Materials, 2005. **17**(17): p. 2115-2119.

49. Lee, W., et al., *Fast fabrication of long-range ordered porous alumina membranes by hard anodization*. Nature Materials, 2006. **5**(9): p. 741-747.

50. Shingubara, S., et al., *Self-organization of a porous alumina nanohole array using a sulfuric/oxalic acid mixture as electrolyte*. Electrochemical and Solid State Letters, 2004. **7**(3): p. E15-E17.

51. Ono, S., et al., *Controlling factor of self-ordering of anodic porous alumina*. Journal of the Electrochemical Society, 2004. **151**(8): p. B473-B478.

52. Chu, S.Z., et al., *Large-scale fabrication of ordered nanoporous alumina films with arbitrary pore intervals by critical-potential anodization*. Journal of the Electrochemical Society, 2006. **153**(9): p. B384-B391.

53. Lee, W., K. Nielsch, and U. Gösele, *Self-ordering behavior of nanoporous anodic aluminum oxide (AAO) in malonic acid anodization*. Nanotechnology, 2007. **18**(47): p. 475713.

54. Schwirn, K., et al., *Self-ordered anodic aluminum oxide formed by H2SO4 hard anodization*. Acs Nano, 2008. **2**(2): p. 302-310.

55. Chen, W., J.S. Wu, and X.H. Xia, *Porous anodic alumina with continuously manipulated pore/cell size*. Acs Nano, 2008. **2**(5): p. 959-965.

56. Li, Y.B., et al., *Fabrication of highly ordered nanoporous alumina films by stable high-field anodization*. Nanotechnology, 2006. **17**(20): p. 5101-5105.

57. Li, Y.B., M.J. Zheng, and L. Ma, *High-speed growth and photoluminescence of porous anodic alumina films with controllable interpore distances over a large range*. Applied Physics Letters, 2007. **91**(7): p. 073109.

58. Zhao, S.Y., et al., *Novel structure of AAO film fabricated by constant current anodization*. Advanced Materials, 2007. **19**(19): p. 3004-3007.

59. Lee, K., Y. Tang, and M. Ouyang, *Self-Ordered, Controlled Structure Nanoporous Membranes Using Constant Current Anodization*. Nano Letters, 2008. **8**(12): p. 4624-4629.

60. Masuda, H. and M. Satoh, *Fabrication of gold nanodot array using anodic porous alumina as an evaporation mask*. Japanese Journal of Applied Physics Part 2-Letters, 1996. **35**(1B): p. L126-L129.

61. Li, F.Y., L. Zhang, and R.M. Metzger, *On the growth of highly ordered pores in anodized aluminum oxide*. Chemistry of Materials, 1998. **10**(9): p. 2470-2480.

62. Nielsch, K., et al., *Self-ordering regimes of porous alumina: The 10% porosity rule*. Nano Letters, 2002. **2**(7): p. 677-680.

63. Masuda, H., et al., *Highly ordered nanochannel-array architecture in anodic alumina*. Applied Physics Letters, 1997. **71**(19): p. 2770-2772.

64. Choi, J., et al., *Fabrication of monodomain alumina pore arrays with an interpore distance smaller than the lattice constant of the imprint stamp*. Journal of Vacuum Science & Technology B, 2003. **21**(2): p. 763-766.

65. Asoh, H., et al., *Conditions for fabrication of ideally ordered anodic porous alumina using pretextured Al*. Journal of the Electrochemical Society, 2001. **148**(4): p. B152-B156.

66. Mikulskas, I., et al., *Aluminum oxide photonic crystals grown by a new hybrid method*. Advanced Materials, 2001. **13**(20): p. 1574-1577.

67. Li, A.P., F. Muller, and U. Gosele, *Polycrystalline and monocrystalline pore arrays with large interpore distance in anodic alumina*. Electrochemical and Solid State Letters, 2000. **3**(3): p. 131-134.

68. Sun, Z.J. and H.K. Kim, *Growth of ordered, single-domain, alumina nanopore arrays with holographically patterned aluminum films*. Applied Physics Letters, 2002. **81**(18): p. 3458-3460.

69. Krishnan, R., et al., *Wafer-level ordered arrays of aligned carbon nanotubes with controlled size and spacing on silicon*. Nanotechnology, 2005. **16**(6): p. 841-845.

70. Krishnan, R. and C.V. Thompson, *Monodomain high-aspect-ratio 2D and 3D ordered porous alumina structures with independently controlled pore spacing and diameter*. Advanced Materials, 2007. **19**(7): p. 988-992.

71. Kim, B.Y., et al., *Fabrication of ordered anodic aluminum oxide using a solvent-induced array of block-copolymer micelles*. Small, 2007. **3**(11): p. 1869-1872.

72. Choi, J.S., R.B. Wehrspohn, and U. Gösele, *Moiré pattern formation on porous alumina arrays using nanoimprint lithography*. Advanced Materials, 2003. **15**(18): p. 1531-1534.

73. Asoh, H., et al., *Growth of anodic porous alumina with square cells*. Electrochimica Acta, 2003. **48**(20-22): p. 3171-3174.

74. Masuda, H., et al., *Square and triangular nanohole array architectures in anodic alumina*. Advanced Materials, 2001. **13**(3): p. 189-192.

75. Lee, W., et al., *Structural engineering of nanoporous anodic aluminium oxide by pulse anodization of aluminium*. Nature Nanotechnology, 2008. **3**(4): p. 234-239.

76. Losic, D., M. Lillo, and D. Losic, *Porous Alumina with Shaped Pore Geometries and Complex Pore Architectures Fabricated by Cyclic Anodization*. Small, 2009. **5**(12): p. 1392-1397.

77. Crouse, D., et al., *Self-ordered pore structure of anodized aluminum on silicon and pattern transfer*. Applied Physics Letters, 2000. **76**(1): p. 49-51.

78. Choi, J.S., et al., *Monodisperse metal nanowire arrays on Si by integration of template synthesis with silicon technology*. Journal of Materials Chemistry, 2003. **13**(5): p. 1100-1103.

79. Rabin, O., et al., *Formation of thick porous anodic alumina films and nanowire arrays on silicon wafers and glass*. Advanced Functional Materials, 2003. **13**(8): p. 631-638.

80. Tian, M.L., et al., *Penetrating the oxide barrier in situ and separating freestanding porous anodic alumina films in one step*. Nano Letters, 2005. **5**(4): p. 697-703.

81. Masuda, H., K. Nishio, and N. Baba, *Fabrication of a One-Dimensional Microhole Array by Anodic-Oxidation of Aluminum*. Applied Physics Letters, 1993. **63**(23): p. 3155-3157.

82. Cojocaru, C.S., et al., *Conformal anodic oxidation of aluminum thin films*. Nano Letters, 2005. **5**(4): p. 675-680.

83. Gowtham, M., et al., *Controlled fabrication of patterned lateral porous alumina membranes*. Nanotechnology, 2008. **19**(3): p. 035303.

84. Xiang, Y., et al., *Microstructured horizontal alumina pore arrays as growth templates for large area few and single nanowire devices*. Physica Status Solidi-Rapid Research Letters, 2008. **2**(2): p. 59-61.

# Chapter 2. Pore Formation During Aluminum Anodization; the Interaction of Two Instabilities

## 2.1 Introduction

Porous anodic aluminum oxide (AAO) is created through electrochemical oxidation in an acidic electrolyte which dissolves $Al_2O_3$ at the same time new $Al_2O_3$ is formed. In the steady-state, the thickening of porous layers occurs at a constant rate, while the thickness of the continuous $Al_2O_3$ layer at the bottom of the pores, the barrier layer, remains constant. This implies that a dynamic equilibrium between film formation by oxidation at the metal/oxide (m/o) interface and film dissolution at the oxide/electrolyte (o/e) interface develops [1-3]. This occurs when the field across the oxide is 8.33 to 12.5 MV/cm. However, the chemical dissolution rate of the oxide is, in fact, several orders of magnitude smaller than the formation rate in the steady state [4]. A field-assisted dissolution model was suggested to explain steady-state anodization kinetics, by arguing that the dissolution rate of $Al_2O_3$ increases in the presence of a high external electric field (E-field) at the tips of pores [1,2]. The porous structures can therefore achieve a steady state when the field-enhanced dissolution at the base of the pores balances the oxide formation rate. Moreover, pores are thought to first form at local points, e.g. associated with defects and non-uniform oxide thickness, where the E-field is concentrated [5]. However, the effect of the electric field on the oxide dissolution rate has not been measured due to the nature of the dynamic equilibria and the non-uniform E-field distribution at pore tips.

In addition to the field-assisted dissolution of the oxide at high external electric field, it has also been shown that $Al^{3+}$ ions are directly ejected into the acidic electrolyte, without deposition of oxide at the o/e interface [6, 7]. This process is called as field-assisted ejection of $Al^{3+}$ ions and is thought to be a necessary condition for the formation of porous aluminum oxide, otherwise roughened surfaces associated with the initiation of pore formation at the o/e interface will be flattened by preferential thickening at the pore tip due to oxidation from mobile $Al^{3+}$ ions at the o/e interface [8].

In this chapter, we investigate pore formation mechanisms by decoupling kinetic and morphological interactions between the m/o and o/e interfaces during Al anodization. To measure the effect of an external E-field on the $Al_2O_3$ dissolution rate, we developed a discontinuous anodization process that allows decoupling of the dynamic equilibria associated with the oxidation and dissolution reactions. As illustrated in Fig. 2-1, this was done by first pre-forming an $Al_2O_3$ barrier oxide layers with flat surfaces, and then continuing anodization under conditions that lead to formation of porous AAO formation, i.e. using 5 wt.% $H_3PO_4$ as the electrolyte. Pre-forming of the $Al_2O_3$ allows application of an electric field that drives dissolution of the alumina without causing further oxidation of the aluminium. The initial E-field, $\boldsymbol{E}_o$, across the oxide is controlled by the thickness of the pre-formed oxide, $h_o$, and the applied anodic voltage, $V_{an}$ ($\boldsymbol{E}_0 = V_{an}/h_0$).

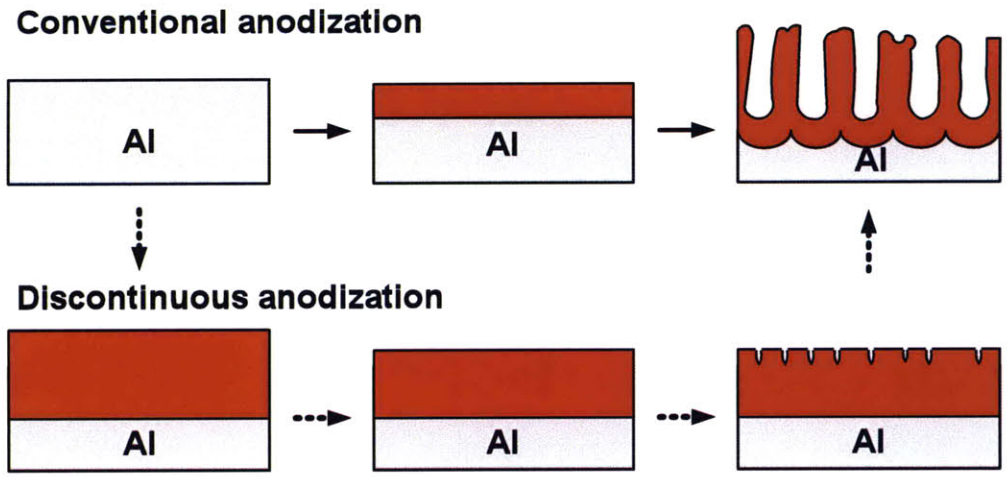


**Figure 2-1.** Schematic illustration of the discontinuous anodization process. (top) In conventional anodization processes, field-assisted dissolution of the oxide is hard to characterize because of simultaneous growth and dissolution processes. (bottom) A discontinuous anodization process was devised to measure the rate of oxide dissolution due to an applied electric field and to determine morphological evolution of pore formation. This involved pre-anodization under conditions that lead to an oxide of uniform thickness with a flat surface, followed by anodization under conditions that are known to lead to pore formation.

## 2.2 Experiments

Thin films of Al (500 ~ 600 nm) were deposited on thermally oxidized Si substrates using e-beam evaporation. The base pressure was $1 \times 10^{-6}$ Torr and the thickness of the films was determined using a quartz crystal monitor. For formation of $Al_2O_3$ with flat surfaces, Al thin films were anodized in a solution of 0.5 M boric acid ($H_3BO_3$, Merck) and 0.05 M sodium borate ($Na_2B_4O_710H_2O$, J. T. Baker) at various current densities (0.15, 1.5, and 15 mA/cm$^2$) and at room temperature. The thickness of the barrier oxide was controlled by controlling the reaction time by monitoring the anodic

voltage. The pre-formed barrier oxide was then transferred to 5 wt.% phosphoric acid. Anodization in 5 wt.% phosphoric acid was conducted at a constant voltage, ranging from 86V to 150V, and at room temperature. Changes in the thickness and morphology of the barrier oxide were observed using scanning electron microscopy. In Fig. 2-9 (b), thin films of $SiO_2$ with 500 nm thickness were deposited on the Al film using plasma-enhanced chemical vapor deposition (PECVD) at 250°C to prevent anodization from the top surface of the Al. $SiO_2$ gratings were patterned using photolithography and reactive ion etching (RIE) in $CF_4$. Photoresist (AZ1518, Shipley; 1.5μm-thick) was deposited on the $SiO_2$ capping layer was also used as a mask layer to prevent unwanted anodization of Al from the top surface through pin-holes in the PECVD $SiO_2$. The exposed Al surface where the $SiO_2$ mask was removed was anodized in 5 wt.% $H_3PO_4$ at 86V and 3°C.

## 2.3 Pore Formation Mechanisms; Field-induced and Strain-induced Instabilities

Figures 2-2 (a) and (b) show SEM images of pre-formed $Al_2O_3$ before and after re-anodization in 5 wt.% $H_3PO_4$ at RT and an anodic voltage of 86V. The initial E-field, $\boldsymbol{E_0}$, for the second anodization in 5 wt.% phosphoric acid was set significantly lower than the anodic ratio of porous alumina, i.e. 1.12 nm/V. For example, the anodic ratio during the second anodization becomes 1.86 nm/V (or 5.36 MV/cm in E-field). The $\boldsymbol{E_0}$ was then too low to drive anions to react with Al through the barrier oxide. Figure 2-2 (b) clearly shows that the thickness of the barrier oxide decreased to 131 nm from 160 nm after anodization for 49 min in 5 wt.% $H_3PO_4$ at 86V, while the thickness of the Al remained

unchanged. During the second anodization, the morphologies of the m/o and o/e interfaces in Figure 2-2 (b) do not change, allowing calculation of the E-field across the layer.

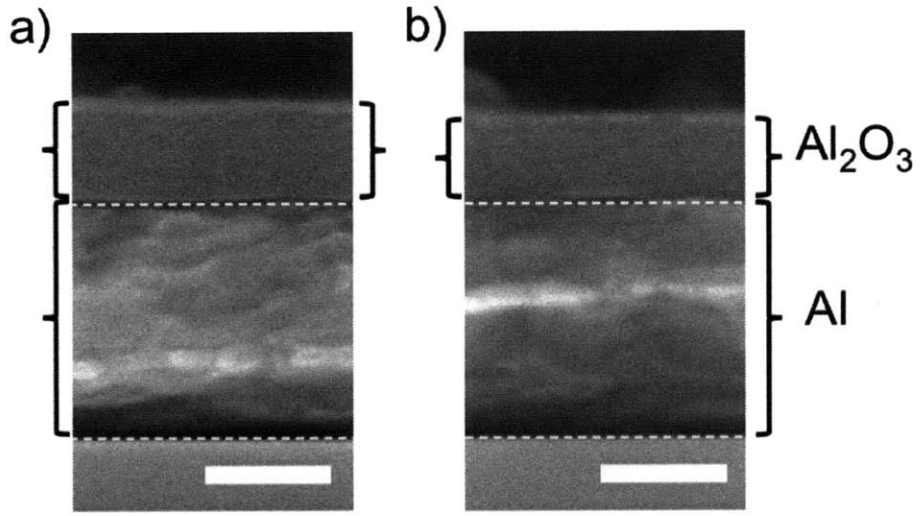


**Figure 2-2.** Field-assisted dissolution of AAO. (a), (b), Cross-sectional SEM images of $Al_2O_3$ formed from an Al film on a Si substrate by anodizing in 0.5M boric acid and 0.05M sodium borate solution: (a) before and (b) after re-anodizing in 5 wt.% $H_3PO_4$ solution with electric field ($V_{an}$=86V) turned-on for 49 min at room temperature. Scale bar = 200 nm.

Figure 2-3 shows the dissolution rate for a fixed initial thickness and different applied bias. Also shown is the dissolution rate at zero applied bias. The zero-bias results show the result of purely chemical dissolution. When a bias is applied, the alumina thickness decreases over time and the electric field increases. Initially, at high fields, the dissolution is purely chemical, with a rate of 0.24 nm/min. However, as the field

increases there is a point at which the dissolution rate significantly increases. For example, at $E_0$ = 5.36 MV/cm, while the dissolution rate is consistent with the chemical dissolution for an initial 20 min, as the thickness of the $Al_2O_3$ decreases, the E-field across the barrier oxide increases and the dissolution rate begins to significantly increase, to about 0.45 nm/min. When $E_0$ is increased to 6.685 MV/cm in 5 wt.% $H_3PO_4$, the dissolution rate of the $Al_2O_3$ is about 17 times faster (4.08 nm/min) than the chemical dissolution rate. It should be noted that during the measurement shown in Fig. 2-3, the morphology of the pre-formed oxide and the thickness of the unreacted Al film did not change.

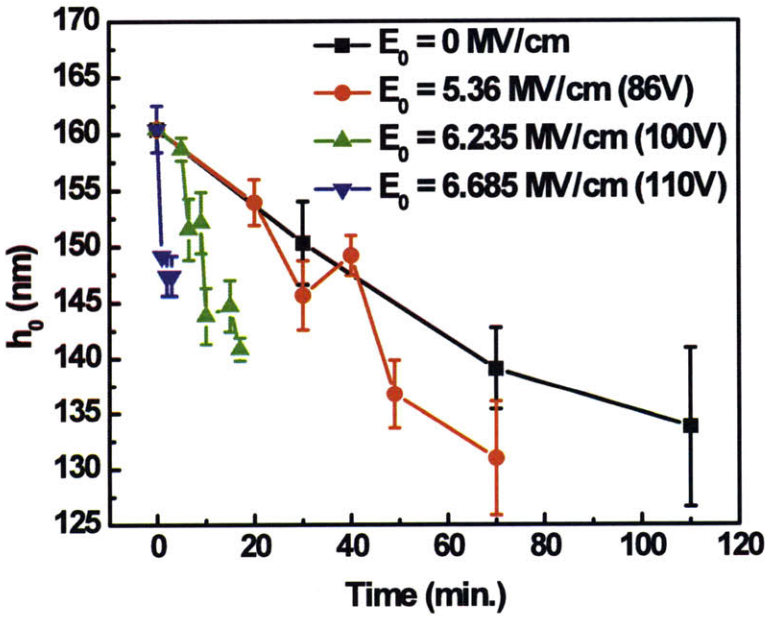


**Figure 2-3.** Field-assisted dissolution of AAO. Changes in the thickness of a planar pre-formed $Al_2O_3$ layer lead to associated changes in the subsequent field- and time-dependent dissolution behavior in 5 wt.% $H_3PO_4$ solution.

The field effect illustrated in Fig. 2-3 sheds light on the dissolution mechanism. Mott and Hoar suggested that dissolution of aluminum oxide in an acid electrolyte proceeds by spontaneous decomposition of $Al_2O_3$ at the o/e interface into $Al^{3+}$ and $O^{2-}$ ions leading to net dissolution with the dissolution rate determined by the rate of removal of the $O^{2-}$ ions via field-enhanced diffusion through the oxide. In this case $Al_2O_3$ forms at the m/o interface and a dynamic equilibrium between dissolution and formation of the alumina would be established [1]. However, the observed invariance of the Al film thickness indicates that the E-field is too week to drive transport of the oxygen ions though the oxide. Therefore, our results indicate that dissolution of $Al_2O_3$ occurs through the following reaction

$$Al_2O_3 + 6H^+ \rightarrow 2Al^{3+} + 3H_2O \qquad (1)$$

at the o/e interface, through modification of the polarization of the Al-O bond [2]. It should be noted that reaction (1) is chemical in nature and hence does not contribute to the anodization current.

At sufficiently high E-field, the o/e interface becomes unstable with respect to perturbations due to non-uniform dissolution. Fig. 2-4 (a) and (b) demonstrates incipient pore formation after 5 minutes of anodization in 5 wt.% $H_3PO_4$ at 110V. Invariance of the Al film thickness and the m/o interface morphology confirms that the incipient pores are developed by field-assisted dissolution so that pore formation occurs as a result of a field-induced instability at the o/e interface. Pore growth due to a field-induced instability is self-stabilized since the local E-field at the base of the pores increases the dissolution rate of the oxide at the base, which results in further strengthening of the E-field. In turn, the

E-field becomes strong enough to drive diffusion of $O^{2-}$ ions to the m/o interface for $Al_2O_3$ growth. After 7 minutes of anodization, anodic oxidation of Al begins as the E-field at the base of the pores further increases to 8.4 MV/cm (Fig. 2-4 (a)). As a result, the total thickness of the $Al_2O_3$ increased to 174 nm, thicker than the pre-formed $Al_2O_3$, and a dynamic equilibrium is maintained. It should be noted, however, that the interpore distance associated with the field-induced instability, $\lambda_F$, is only about 30 nm, significantly smaller than the 275 nm expected from conventional anodization.

The dissolution rate, incipient pore formation, and anion transport through the barrier oxide are governed by the E-field across the oxide [3]. Fig. 2-4 (c) shows changes in the E-field at various anodic voltages. The E-field increased as the pre-formed barrier oxide thinned via field-assisted dissolution at a constant voltage. After the initiation of pore formation, i.e. after 5 min at 110V, the barrier thickness rapidly decreased as the pores developed, as shown in Fig. 2-4 (a), and a rapid increase of the E-field across the barrier oxide results, reaching a steady-state value of 8.9 MV/cm. Interestingly, the E-fields at which the incipient pores formed are consistently about 7.46 MV/cm, regardless of the initial anodic voltage. Therefore, the transition E-field in Fig. 2-4 (c) is defined as the critical E-field for initiation of pore formation, $\boldsymbol{E^*}$, associated with the field-assisted dissolution mechanism. $\boldsymbol{E^*}$ is 7.46 MV/cm in 5 wt.% phosphoric acid at room temperature. The oxide only thins without a morphological change if $\boldsymbol{E < E^*}$, and pores will form at the o/e interface if $\boldsymbol{E > E^*}$. It should be noted that $\boldsymbol{E^*}$ is much smaller than the E-field associated with steady state pore formation (8.9 MV/cm).

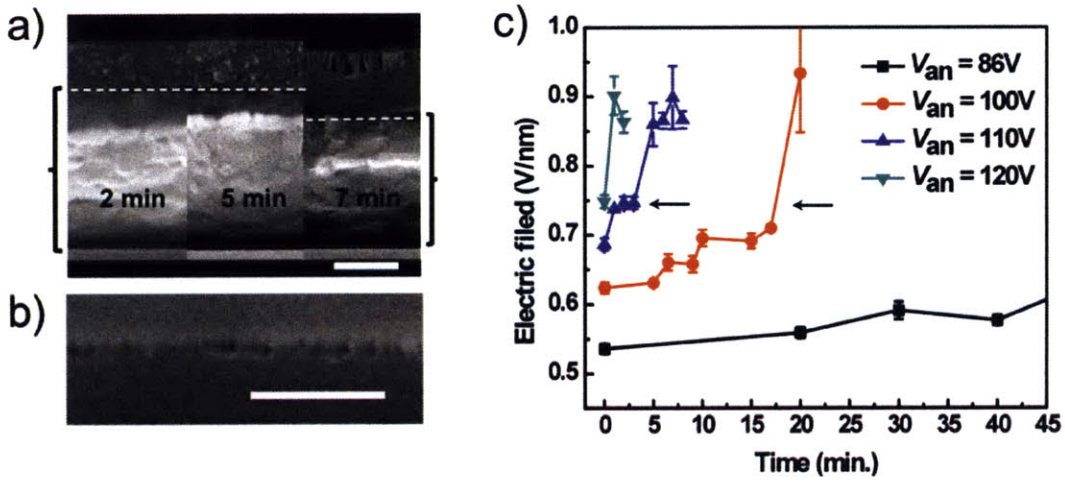


**Figure 2-4.** Incipient pore formation due to field-assisted dissolution. a) Morphological evolution of $Al_2O_3$ layers with initially flat surfaces as porous structures form during anodization in a 5 wt.% $H_3PO_4$ solution with an anodic voltage of 110V at RT. The incipient pores form at the oxide/electrolyte interface after 5 min of anodization. b) A 25° tilted higher-magnification view of the incipient pores at the o/e interface after 5 min of anodization at 110V at room temperature (the middle figure in a)). c) The average electric field across the AAO during anodization in a 5 wt.% $H_3PO_4$ solution at a constant voltage from 86 to 120V, as a function of time. The electric field initially slowly increases due to the thickness reduction caused by field-assisted dissolution of the oxide. The field then rapidly increases due to re-growth of AAO and pore formation in phosphoric acid. Formation of the incipient pores begins at the critical E-field, $\boldsymbol{E^*}$. The arrows in the plot indicate $\boldsymbol{E^*}$. Scale bar = 200 nm.

When $E$ increases from $E^*$ to the value associated with steady state pore formation, 8.9 MV/cm, a second instability begins to develop. This instability ultimately results in pores with the larger spacings usually associated with anodization of aluminum. Fig. 2-5 (a) illustrates the transition stage in the morphological evolution from incipient to secondary porous structures when anodization was carried out for 4 min at $V_{an}$ = 140V in 5 wt.% $H_3PO_4$ at room temperature, with a pre-formed oxide of thickness of 160 nm ($E_0$ = 8.75 MV/cm). As shown in Fig. 2-5 (a), both the pore-oxide interface (p-o) and the metal-oxide interface developed perturbed shapes and one of the incipient pores at a minimum in the p-o interface began to grow preferentially and to widen. This secondary instability leads to development of a larger scale pore structure and a dual scale pore structure near the o/e and m/o interfaces. The spacing of the secondary pores at the m/o interface is about 400 nm and that of the incipient pores at the o/e interface is about 37 nm. In conventional porous AAO formation, the pore spacing has been empirically shown to depend linearly on $V_{an}$ with a proportionality, $\xi$, of 2.0 ~ 2.5 nm/V [2, 9]. Porous alumina with different pore periods can form only when the anodic voltage also changes during anodization, where the spacing is still set by the $\xi$ and $V_{an}$ [2, 10]. However, Fig. 2-5 (a) shows that a constant anodic voltage can create a dual-scale porous structure having distinctively different $\xi$'s, such as 0.27 nm/V (in the regime of a weak voltage dependence) and 2.8 nm/V (in the regime of a strong voltage dependence). This implies that these two instabilities have different formation mechanisms. In the discussion of Fig. 2-4 (a) – (c) we demonstrated that the incipient pores, for which $\xi$ = 0.27 nm/V, originate from field-assisted dissolution of the oxide at the o/e interface with

$E > E^* = 7.46$ MV/cm. The weak voltage dependence of the pore spacing can be inferred from the fact that the dissolution kinetics of the oxide depends on the electric field at the o/e interface, not on the applied voltage. Therefore, the secondary pore structure, with $\xi =$ 2.8 nm/V in Fig. 2-5 (a), may originate from a mechanism other than field assisted dissolution of the oxide. Indeed, we found that secondary pores formed at significant electrical currents (~ 1.4 mA/cm$^2$ at $V_{an}$ = 140V) from an electrochemical reaction, while the incipient pores did not, as shown in Fig. 2-6. The electrochemical oxidation reaction is associated with generation and transport of charged species, such as oxygen and aluminum ions as well as anion impurities, at the m/o and the o/e interfaces of the aluminum oxide. Hence, we postulate that the initiation of a secondary instability is associated with these charged species.

Based on this postulate, we increased $E_0$ to 8.82 MV/cm to generate and drive sufficient ions through the oxide to cause initiation of the secondary instability without prior formation of the incipient pores. The pre-formed $Al_2O_3$ was about 170 nm thick when a current density of 15 mA/cm$^2$ in a mixed solution of boric acid and sodium borate was used. Subsequent application of $V_{an}$ = 150 V for 50 sec in 5 wt.% $H_3PO_4$ at RT, as shown in Fig. 2-5 (b), clearly caused a secondary instability to develop at the o/e interface, while the m/o interface stayed flat. In Fig. 2-5 (b), the small-scale instability due to field assisted dissolution also developed at the o/e interface, because $E_0 > E^*$, but did not evolve into incipient pores. A large scale surface instability developed at the o/e interface, as seen in Fig. 2-5 (b), and led to an increased driving force for oxidation of Al at the m/o interface, due to an increased electric field associated with the thinner barrier

oxide. As a result, the m/o interface follows the surface morphology of the o/e interface, later leading to the steady-sate growth of porous structures at $\xi = 2.5$ nm/V.

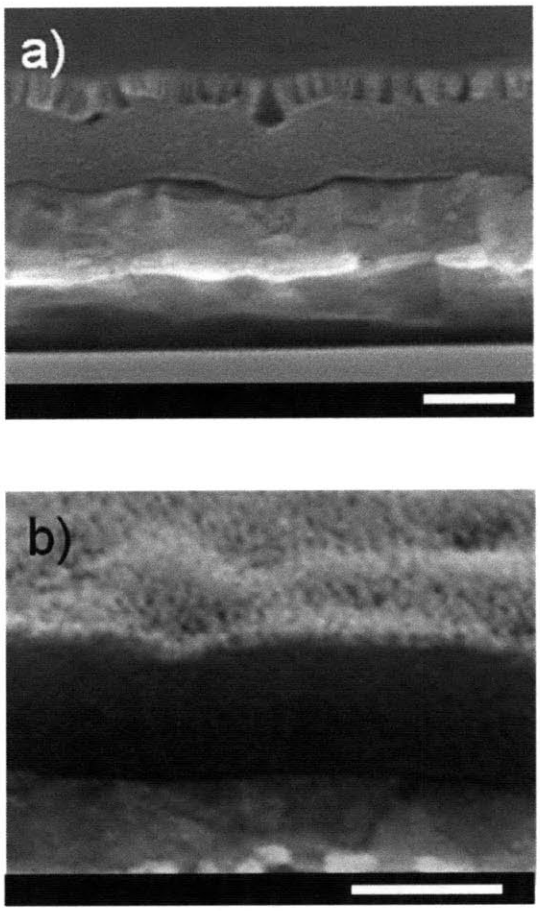


**Figure 2-5.** Larger-scale secondary pore formation due to a mechanical instability. a) Cross-sectional SEM image of AAO with a pre-formed $Al_2O_3$ after re-anodizing in a 5 wt.% $H_3PO_4$ solution at RT with $V_{an}$=140V for 4 min. Waviness at the oxide/electrolyte interface, which was initially flat, indicates plastic deformation of the AAO during the re-growth of AAO in a 5 wt.% $H_3PO_4$ solution. b) Tilted-angle (25°) SEM image of AAO with a pre-formed $Al_2O_3$ after re-anodizing at $V_{an}$=150V for 50 sec. in 5 wt.% $H_3PO_4$ at RT. Here the pre-formed $Al_2O_3$ was formed at 15 mA/cm$^2$ for 15 sec. Scale bars = 200 nm.

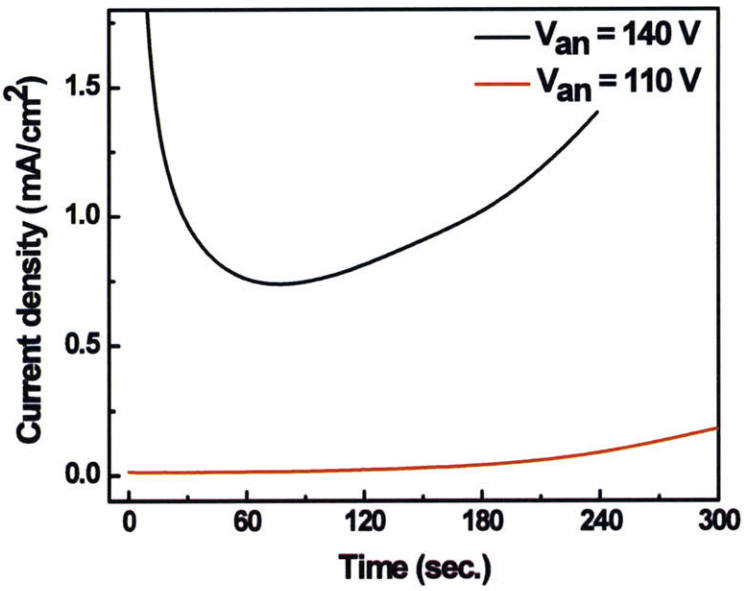


**Figure 2-6.** The *j-t* curve for anodization of Al with a pre-formed $Al_2O_3$ layer re-anodized at different anodic voltages ($V_{an}$) in 5 wt.% $H_3PO_4$. The large-scale instability at the o/e interface shown in Fig. 2-5 (a) accompanies significant growth of the AAO and hence the anodic current.

Defects and impurities in a film generate stress and strain in the film. In Al anodization, from in-situ stress measurements it has been shown that the compressive stress in the oxide develops during anodization [11-13]. While the volume expansion associated with transforming from Al to $Al_2O_3$ can contribute to the measured stress, the in-situ compressive stress is relaxed or even changes sign after anodization is stopped. Therefore, this in-situ stress is believed to originate, at least in part, from insertion and transport of anions ($O^{2-}$ or $OH^-$, impurity ions and phosphorous in our case) and cations ($Al^{3+}$) in the oxide, as well as from electrostriction, forced by the external electric field

[11-13]. We postulate that growth stress/strain that develops during anodization cause the o/e interface to become unstable and induces the secondary instability in the oxide-dissolving electrolyte interface. Asaro and Tiller showed that if a bi-axial stress larger than critical stress, $\sigma_c$, is applied to a material in a corrosive environment, the surface of the material can develop a roughness to lower strain energy, such that

$$\lambda_c = \frac{\pi E \gamma}{\sigma_c^2}, \tag{2}$$

where $\lambda_c$ is the minimum period for a stable perturbation, $E$ is the Young's modulus of the material and $\gamma$ is the interface energy [14]. Asaro and Tiller also showed that for growth of the perturbation by surface diffusion, the fast growing period $\lambda_{max}$ scales with $\lambda_c$. Therefore, the large-scale secondary instability in Fig. 2-5 (b) can develop to lower the strain energy due to localized dissolution and/or incorporation of anion impurities at the o/e interface. According to Eq. (2), $\sigma_c$ = 180 MPa is required to produce a perturbation with a periodicity of 400 nm, assuming a Young's modulus of 122 GPa [15] and $\gamma$ = 34 mJ/m$^2$ [16]. Aziz and co-workers suggested that a reaction interface subjected to a bi-axial stress can be unstable to perturbations due to a stress-dependent diffusivity of reaction species across an interface [17] and Yu and Suo also showed that $\lambda_c \propto 1/\sigma_c$ for a kinetically driven stress instability [18]. While a detailed mechanism for the growth of the secondary instability at the o/e interface in Fig. 2-5 (b) is still unclear, all analyses suggest that $\lambda_c$ (and therefore $\lambda_{max}$) decreases with $\sigma_c$, according to $\lambda_c \propto 1/\sigma_c$ or $\lambda_c \propto 1/\sigma_c^2$, depending on the detailed origin of the instability. It has been reported that the constant compressive stress observed in-situ during anodization at a constant current begins to either decrease or increase (the stress decreases in phosphoric acid and

increases in sulphuric acid at the on-set of pore formation) at the on-set of pore formation [12, 13]. This implies the existence of a critical stress $\sigma_c$ for the secondary instability. For further clarification, in-situ stress measurements at the on-set of pore formation are required as a function of the anodic conditions to relate pore periodicity and the maximum compressive stress $\sigma_{max}$ with different values of $V_{an}$ and in different electrolytes, to determine the detailed mechanisms of the stress induced instability.

The growth stress in the oxide also has an impact on the steady-state pore growth. Fig. 2-5 (a) shows that the morphology of the o/e interface, which was initially flat before anodization, distorts and follows the waviness of the m/o interface, clearly indicating that the oxide was plastically deformed. Recently, Garcia-Vergara et al proposed that the growth of porous AAO is maintained by 'plastic flow' of the oxide, as indicated by experiments in which a tungsten tracer layer was used to indicate flow resulting from steady-state anodization at a constant current [19]. Our result also shows direct evidence that the pore growth, but not the initiation of pore formation, is associated with plastic deformation and flow of the anodic oxide, when the E-field is close to the steady-state value (8.9 MV/cm) and when constant voltages are applied.

The interplay between field-assisted-dissolution and strain-induced instabilities and subsequent plastic deformation and flow in nanoporous AAO can explain formation of hexagonally closed packed porous AAO at certain anodization conditions [9, 20]. At the m/o interface, the rate of formation of new oxide is balanced by the lateral flux through plastic flow of the $Al_2O_3$. The pores, therefore, pack densely to minimize the

flow distance for the collection of pores with repulsive mechanical interactions of each pore arising from the need to share a volume in which the oxide flows.

In steady state, pore propagation is limited by the forced plastic flow of the oxide. Figure 2-7 is a schematic of steady-state pore formation. In analogy with cellular growth during solidification [21], the flux of the newly-generated aluminium oxide at the m/o interface, $J_E$, must be balanced with the flux of the forced plastic flow of the oxide toward the pore wall, $J_\sigma$. From Faraday's law, the flux of the newly-generated $Al_2O_3$ at the m/o interface, $J_E$, is linearly proportional to the anodic current density, $j$,

$$J_E = K_1 j = \frac{N_A \eta}{2z\mathrm{F}} j, \tag{3}$$

where $N_A$ is Avogadro's number, $z$ is the valence number of Al (= 3), F is Faraday's constant, and $\eta$ is the current efficiency for anodic oxidation, which is defined as the current used for formation of the anodic oxide divided by the total current. Under pore-forming anodization conditions, $\eta$ is less than 1 and also dependent on the specific anodic conditions.

Now, the flux from the flow of the oxide toward the pore walls, $J_\sigma$, is a product of the flow velocity of the oxide at the m/o interface, $v$, and the atomic concentration of aluminium oxide, $c_0$, such that,

$$J_\sigma = c_0 v. \tag{4}$$

The flow velocity is related to the strain rate, $\dot{\varepsilon}$, through a general relationship with the flow stress at the m/o interface, $\tau$, by [22]

$$\dot{\varepsilon} = K\tau^n = \frac{1}{\lambda_{pf}} \frac{\mathrm{d}\lambda_{pf}}{\mathrm{dt}} = \frac{1}{\lambda_{pf}} v. \tag{5}$$

In Eq. (5), $K$ is a temperature and material-dependent constant, $n$ is a constant related to the atomistic mechanism for the plastic flow, and $\lambda_{pf}$ is the spacing between pores. It should be noted that Eq. (5) can also represent the flow rate of viscous materials, in which case $K$ is the reciprocal of the viscosity of the material. If Eq. (5) is substituted into Eq. (4), then

$$J_{\sigma} = K\lambda_{pf}\tau^{n}. \tag{6}$$

In steady-state, $J_E = J_{\sigma}$. Therefore,

$$\frac{\lambda_{pf}\tau^{n}}{\eta j} = \frac{N_A}{2zFK} = const. \tag{7}$$

In equation (7), the material-dependent constant $K$ of the anodic alumina is assumed to be independent of the anodization conditions. However, it should be noted that $K$ can depend on the anodic conditions through their effect on anion incorporation and the microstructure of the anodic oxide.

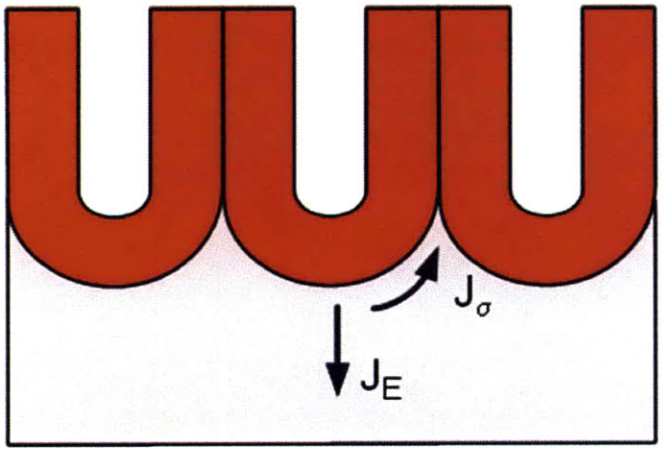


**Figure 2-7.** Schematic diagram of the cellular growth model for the formation of ordered AAO in a steady-state.

The large-scale instability at the o/e interface will have a characteristic spacing, $\lambda_S$ (associated with $\lambda_c$ in Eq. (2)) and the steady state spacing associated with mechanical flow will have a characteristic spacing $\lambda_{pf}$, both of which are large compared to the characteristic length scale of the structure resulting from the electric-field-induced instability, $\lambda_F$. However, $\lambda_{pf}$ in Eq. (7) is not necessarily identical to the $\lambda_S$ because of differences in the underlying mechanism that control the characteristic length scales. If $\lambda_{pf} \neq \lambda_S$, ordering of the pores driven by the plastic flow at the m/o interface will be disturbed by branching (if $\lambda_{pf} > \lambda_S$) or closing (if $\lambda_{pf} < \lambda_S$) of pores through morphological and kinetic interactions. Therefore, for the formation of self-ordered AAO, the anodic conditions for $\lambda_{pf} \sim \lambda_S$ are required. This postulate is supported by the observation that changes in $\lambda_{pf}$ by application of mechanical tensile loads during anodization decreases ordering of AAO under what would otherwise be typical self-ordering anodization conditions (e.g. sulfuric acid, 23V) [23].

In summary, porous structures can independently result from field-induced and strain-induced instabilities. In conventional anodization, AAO results in a porous structure with a single length scale which depends on $V_{an}$ with $\xi = 2 \sim 2.5$ nm/V, and is a consequence of a strain-induced instability. However, pre-forming $Al_2O_3$ can lead to a dual-scale porous structure, even at a constant anodic voltage, associated with both field-induced and strain-induced instabilities. Fig. 2-8 (a) shows a typical example of a dual-scale porous AAO structure resulting from discontinuous anodization at a constant voltage of 86 V. Pores with smaller $\lambda_F$ at the top surface result from field-assisted dissolution at $E > E^*$ with $\sigma < \sigma_c$. As anodizing continues, a strain-induced instability

with characteristic length scale $\lambda_s$ results when $\sigma > \sigma_c$, leading to growth of the conventional ordered porous alumina structure associated with plastic deformation and flow of the oxide (Fig. 2-8 (a) and (b)). Furthermore, Fig. 2-8 (c) – (f) illustrates that by controlling the thickness of the pre-formed $Al_2O_3$, which suppresses growth of AAO in 5 wt.% $H_3PO_4$, the secondary strain-induced instability is delayed and the field-induced instability becomes dominant when $\sigma$ becomes less than $\sigma_c$, even when the anodization conditions are the same for all pre-formed oxide thicknesses.

## 2.4 Dendrite-like Pore Formation; Tertiary Instability

Fig. 2-9 (a) demonstrates the impact of mechanical confinement on plastic flow of porous AAO. Here, an underlying Al film was anodized in a radial direction due to a pin-hole in the pre-formed barrier oxide of thickness 160 nm, formed at anodic conditions of $V_{an}$ = 86V in 5 wt.% $H_3PO_4$. When the pre-formed oxide is too thick to be deformed mechanically, the plasticity in the radial direction at the Al-preformed-oxide interface is suppressed, leading to a build up of stress in the radial direction. As this stress builds up at the m/o interface, a secondary strain-induced instability develops as $\lambda_{pf}$ decreases according to Eq. (7). The resulting structure is analogous to dendrite structures formed during solidification, just as the ordered porous structures are analogous to cellular structures developed during solidification [21]. Therefore, this instability becomes a *tertiary* instability if the field-induced instability is included. When half of a mechanically stiff $SiO_2$ mask was removed, as shown in Fig. 2-9 (b), conventional pores

were observed in the exposed Al area but dendritic pores formed under the mask, owing to the mechanical constraint of the hard mask.

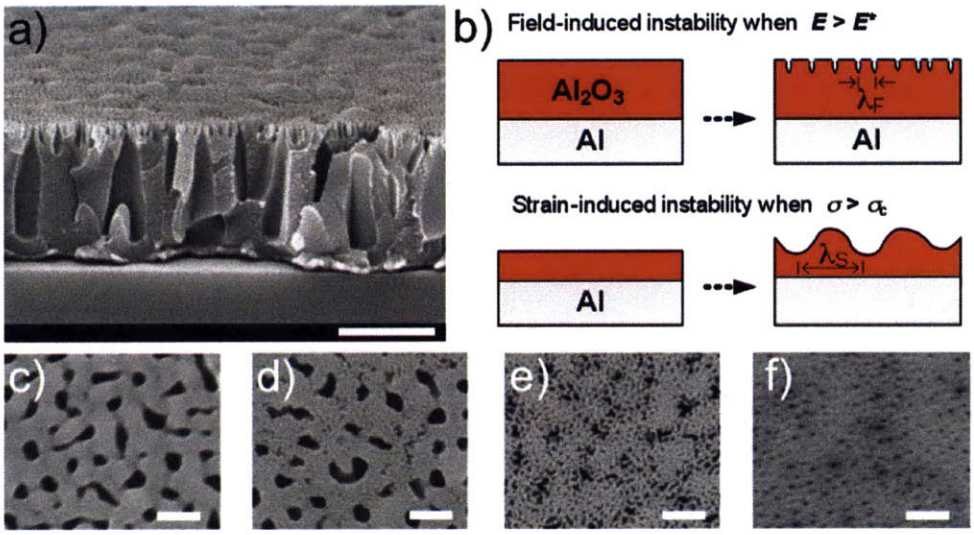


**Figure 2-8.** Dual-scale porous AAO and mechanisms for formation of AAO. a) Cross-sectional SEM image showing dual-scale porous AAO with a pre-formed $Al_2O_3$ layer, after re-anodizing in a 5 wt.% $H_3PO_4$ solution at RT with $V_{an}$=86V. Scale bar = 500 nm. b) Pore generation mechanisms; a field-induced instability when $\boldsymbol{E} > \boldsymbol{E}^*$ and a strain-induced instability when $\sigma > \sigma_c$. These instabilities are independent in origin and have different characteristic wavelengths, $\lambda_F$ and $\lambda_S$, respectively. While the field-induced instability develops in electrolytes which dissolve $Al_2O_3$ (acidic and basic solutions) when $\boldsymbol{E} > \boldsymbol{E}^*$, a strain induced instability can develop in any electrolyte, even in neutral solutions, when $\sigma > \sigma_c$. c)-f) Top-view SEM images of porous AAO anodized in 5 wt.% $H_3PO_4$ at $V_{an}$ = 86 V and at RT with a pre-formed planar $Al_2O_3$ layer of thickness (c) $h_0$ = 0 nm, (d) $h_0$ = 64 nm, (e) $h_0$ = 96 nm, and (f) $h_0$ = 128 nm. The strain-induced instability prevails in (c) where anodizationwas carried out under conventional anodization conditions. With pre-formed $Al_2O_3$ layers the time to reach the condition $\sigma > \sigma_c$ is longer and as $h_0$ is increased, the depth of the pores formed due to the electric-field-induced instability is greater, since $\boldsymbol{E}$ is greater than $\boldsymbol{E}^*$ for a longer time. In (f), only pores from the field-induced instability can be seen. Scale bars = 200 nm.

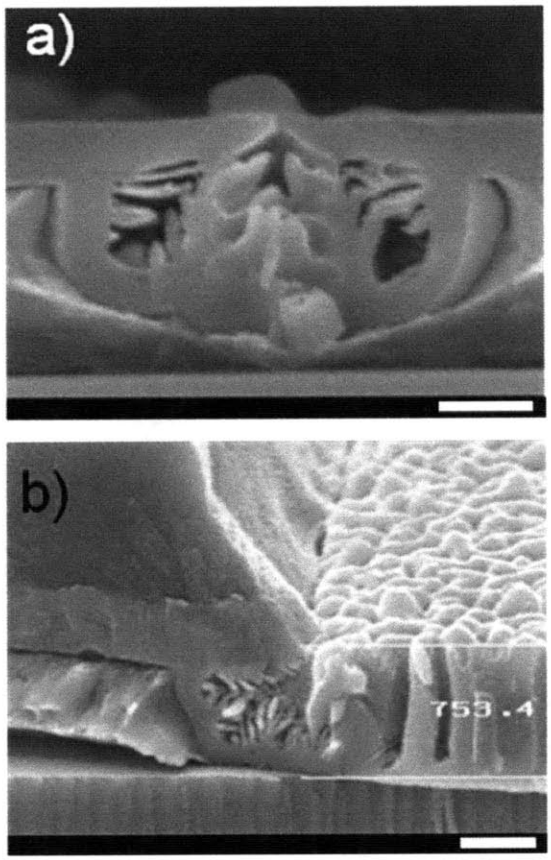


**Figure 2-9.** Dendritic growth under mechanical constraints. a) Cross-sectional SEM image of AAO after re-anodization in 5 wt.% $H_3PO_4$ solution at $V_{an}$ = 86V and RT for 49 min. with a 160 nm-thick pre-formed $Al_2O_3$ layer. Growth of porous AAO forms at a pin-hole in the pre-formed $Al_2O_3$. Scale bar = 200 nm. b) Cross-sectional SEM image showing that a dendritic instability develops when a pore forms under a silicon dioxide layer, due to mechanical constraint of plastic flow. Here, the dendritic porous structure is only seen under the edge of the $SiO_2$ mask. Conventional porous AAO formation occurs where the mask was removed and plastic flow of the AAO is allowed. Scale bar = 400 nm.

Interestingly, growth of porous AAO was found to be retarded in the presence of the mechanical constraint; the growth rate of unconstrained growth of AAO was about 18 nm/min but that of constrained AAO was about 3 nm/min in 5 wt.% $H_3PO_4$ at 3°C and at $V_{an}$= 86V. From Eq. (7), the formation rate of AAO is directly related to the rate of plastic flow of the oxide. Therefore, the formation rate of AAO will be significantly reduced when the rate of plastic flow of the oxide is decreased.

## 2.5 Conclusions

We have demonstrated that the formation of nanoporous AAO is affected by both electrochemical and mechanical instabilities. This was done by growing flat oxides with uniform thickness, but of different thicknesses, before switching to the conditions that lead to pore formation. When present, the field-instability precedes the strain-induced instability and leads to disordered pores with relatively small spacings. Contrary to common belief, it is shown that it is a mechanical instability that leads to the larger-scale ordered structures often used as scaffolds for growth of the nanoscale 1-D structures. Once a mechanical instability develops, the growth of the associated pore structure is limited by the kinetics of lateral deformation/flow of the oxide at the base of the pores. This mechanism and the resulting structure are analogous to cellular growth during solidification. Mechanical constraints can also lead to dendritic growth of pores. Recognition of the influences of mechanical deformation and mechanical constraints on oxide flow should provide new insight into methods that can be used to control the

structures resulting from anodization, not only for aluminum but possibly also for other metals such as Ti.

## References


1. Hoar, T.P. and N.F. Mott, *A mechanism for the formation of porous anodic oxide films on aluminium*. Journal of Physics and Chemistry of Solids, 1959. **9**(2): p. 97-99.
2. O'Sullivan, J.P. and G.C. Wood, *The Morphology and Mechanism of Formation of Porous Anodic Films on Aluminium*. Proceedings of the Royal Society of London. A. Mathematical and Physical Sciences, 1970. **317**(1531): p. 511-543.
3. Parkhutik, V.P. and V.I. Shershulsky, *Theoretical Modeling of Porous Oxide-Growth on Aluminum*. Journal of Physics D-Applied Physics, 1992. **25**(8): p. 1258-1263.
4. Hunter, M.S. and P. Fowle, *Factors Affecting the Formation of Anodic Oxide Coatings*. Journal of the Electrochemical Society, 1954. **101**(10): p. 514-519.
5. Thompson, G.E., et al., *Nucleation and Growth of Porous Anodic Films on Aluminum*. Nature, 1978. **272**(5652): p. 433-435.
6. Siejka, J. and C. Ortega, *An $O^{18}$ Study of Field-Assisted Pore Formation in Compact Anodic Oxide Films on Aluminum*. Journal of the Electrochemical Society, 1977. **124**(6): p. 883-891.
7. Cherki, C. and J. Siejka, *Study by Nuclear Microanalysis and $O^{18}$ Tracer Techniques of the Oxygen Transport Processes and the Growth Laws for Porous Anodic Oxide Layers on Aluminum*. Journal of the Electrochemical Society, 1973. **120**(6): p. 784-791.
8. Thompson, G.E., Thin Solid Films, 1997. **29**: p. 192-201.

9. Lee, W., et al., *Fast fabrication of long-range ordered porous alumina membranes by hard anodization*. Nature Materials, 2006. **5**(9): p. 741-747.

10. Meng, G.W., et al., *Controlled fabrication of hierarchically branched nanopores, nanotubes, and nanowires*. Proceedings of the National Academy of Sciences of the United States of America, 2005. **102**(20): p. 7074-7078.

11. Bradhurst, D.H. and J.S.L. Leach, *The Mechanical Properties of Thin Anodic Films on Aluminum*. Journal of the Electrochemical Society, 1966. **113**(12): p. 1245-1249.

12. Wüthrich, N., *Intrinsic stresses in anodic films on aluminium*. Electrochimica Acta, 1981. **26**(11): p. 1617-1623.

13. Van Overmeere, Q., B. Nysten, and J. Proost, *In situ detection of porosity initiation during aluminum thin film anodizing*. Applied Physics Letters, 2009. **94**(7): p. 074103.

14. Asaro, R.J. and W.A. Tiller, *Interface morphology development during stress corrosion cracking: Part I. Via surface diffusion*. Metall. Trans., 1972. **3**: p. 1789-1796.

15. Alcalá, G., et al., *Mechanical properties of amorphous anodic alumina and tantala films using nanoindentation*. Nanotechnology, 2002. **13**(4): p. 451-455.

16. Liu, S.H., et al., *Effect of surface physicochemical properties on the lubricating properties of water film*. Applied Surface Science, 2008. **254**(22): p. 7137-7142.

17. Barvosa-Carter, W., et al., *Kinetically driven growth instability in stressed solids*. Physical Review Letters, 1998. **81**(7): p. 1445-1448.

18. Yu, H.H. and Z. Suo, *Stress-dependent surface reactions and implications for a stress measurement technique*. Journal of Applied Physics, 2000. **87**(3): p. 1211-1218.

19. Garcia-Vergara, S.J., et al., *A flow model of porous anodic film growth on aluminium*. Electrochimica Acta, 2006. **52**(2): p. 681-687.

20. Masuda, H. and K. Fukuda, *Ordered Metal Nanohole Arrays Made by a 2-Step Replication of Honeycomb Structures of Anodic Alumina*. Science, 1995. **268**(5216): p. 1466-1468.

21. Flemings, M.C., *Solidification processing*. 1974, New York: McGraw-Hill.

22. Meyers, M.A. and K.K. Chawla, *Mechanical behavior of materials*. 1999, Upper Saddle River: Prentice-Hall, .

23. Sulka, G.D., et al., *Effect of tensile stress on growth of self-organized nanostructures on anodized aluminum*. Journal of the Electrochemical Society, 2004. **151**(5): p. B260-B264.

# Chapter 3. Abnormal Anodic Aluminum Oxide Formation in Confined Structures for Lateral Pore Arrays

## 3.1 Introduction

Nanostructured porous materials provide important templates and scaffolds for growth and assembly of one-dimensional (1-D) nanomaterials for a wide spectrum of applications such as electronic, optical, and energy storage devices [1-4]. When the nanostructure of the template can be controlled, control of the position of individual 1-D nanomaterials can also be exercised, allowing, in principle, integrated functionality for each individual nanowire and nanotube. Because of the anisotropic nature of 1-D nanomaterials, arrays of nanowires and nanotubes can be formed vertically and horizontally with respect to a substrate and the orientation of the assembly should be chosen to maximize their functionality. For example, vertically ordered 1-D nanomaterials are suitable for devices requiring high-surface area and high density, such as Li-ion batteries, and horizontally ordered semiconductor 1-D wires and tubes are desirable for devices with more than 3 electrodes, such as a metal-oxide-semiconductor field effect transistors [4-6]. Therefore, development of a nanostructured template with pores aligned horizontally as well as vertically on a substrate offers important opportunities for integration of nanowires and nanotubes into devices and systems.

Thin film nanoporous anodic aluminum oxide (AAO) has been extensively studied for its use as a template or scaffold for growth of 1-D nanomaterials [7-10]. Porous AAO consists of vertical cylindrical pores in an aluminum oxide matrix formed

by anodic oxidation from the top of an Al film. The pore diameter $D_p$ is adjustable from less than 10 nm to more than 400 nm with controllable high aspect ratio > 1,000:1. The pore spacing $D_s$ linearly depends on the anodic voltage $V_{an}$ with proportionality $\xi = 2 \sim 2.5$ nm/V [9, 11-13]. In addition, after prolonged anodization (2~12 hrs) under specific anodization conditions, the vertical pores self-organize into domains with hexagonally close-packed structures. For example, anodization in sulfuric acid at $V_{an} = 19 \sim 25$ V, oxalic acid at 40V and $120 \sim 150$ V, and phosphoric acid at $160 \sim 195$ V lead to ordered pore formation [11-13]. Moreover, by templating pore formation, a mono-domain of perfectly ordered pores with arbitrary $D_s$ can be produced with controlled symmetry (including non-hexagonal symmetries) and with independently controlled $D_s$ and $D_p$ [14, 15]. By modifying the anodization conditions, the nanostructure of the ordered AAO can be further engineered to have hierarchically branched pores and modulated pore diameters along the pore propagation direction [16, 17]. With these characteristics, porous AAO provides an ideal scaffold for growth of vertically aligned mono-disperse nanowires and nanotubes for functional devices.

Recently, AAO scaffolds with *horizontal* pore arrays in the plane of substrate surfaces have also been fabricated on glass and Si substrates, allowing template-assisted growth of Te and Ni nanowires in lateral scaffolds [18-21]. Because pores only grow in directions normal to the Al surface, a side anodization process for horizontal AAO, H-AAO on substrate surfaces, requires anodization of edges of patterned Al films, with top surfaces protected from anodization. Masuda et al. were first to propose a side anodization process and fabricated mono- and double layers of H-AAO with $D_s \sim 200$

nm. This was done by anodizing vertical Al sidewalls of 200 and 400 nm thickness, prepared by cleaving $Al_2O_3$/Al/glass structures [18]. Cojocaru et al. further refined the process to prepare vertical Al surface confined by $SiO_2$ layers using photolithography and patterning technology, and successfully fabricated multilayers of H-AAO with $D_s < 50$ nm [19]. In previous reports, however, anodization to form lateral pores has been performed only for very short times (5~10 min), resulting in lateral pores with low aspect ratios (<10:1) and poor ordering [18-21]. To achieve highly ordered lateral pore arrays, a prolonged anodization is required under so-called self-ordering anodization conditions.

Since a volume expansion occurs during anodic oxidation, typically ~ 140% under the self-ordering anodization conditions [12], additional stress associated with this volume expansion may arise due to mechanical confinement for prolonged anodization times. As we discussed in earlier chapters, recent literature indicates that mechanical stress accounts for steady-state growth of AAO via plastic deformation and flow of the oxide during anodization of Al [22-24]. Additional mechanical stress from confinement may therefore modify nanostructure evolution and kinetics during horizontal anodization of Al in confined structures, and important insights into understanding of mechanistic aspects of AAO formation may be gained through study of confinement effects. However, a role of mechanical constraint during horizontal anodization of Al in governing the pore structure and kinetics of H-AAO formation has not been studied since side anodization in previous studies was conducted for very short times (5 ~ 10 min.) [18-21].

In this Chapter, we report on prolonged anodization of the edges of $SiO_2$-capped aluminum films, leading to highly ordered lateral pore arrays with $D_s$ ranging from 50 nm to 500 nm and having various numbers of pore stacks from monolayers to 12 layers. For the first time, we observed abnormal growth behavior of AAO in confined structures, including periodic dendritic pore structures. Furthermore, we will show that the unexpected anodic behavior originates from suppressed volume expansion and plastic deformation of the oxide in confined structures during anodization. Based on this understanding, we also explored new anodization conditions that minimize the confinement effect and demonstrated the formation of dendrite-free H-AAO.

## 3.2 Experiments

*Fabrication of vertical Al sidewalls on a substrate*:

First, an Al thin film was deposited using e-beam deposition on thermally grown $SiO_2$ on a Si substrate. Al films with thicknesses from 50 nm to 600nm were deposited. Thin films of $SiO_2$ with 500 nm thickness were then deposited on the Al using plasma-enhanced chemical vapor deposition (PECVD) at 250°C. These films served as mask layers on the Al, to prevent un-wanted anodization from the top surface. The $SiO_2$ was then patterned into strips using photolithography and reactive ion etching (RIE) with $CF_4$, and the Al surface was locally exposed where the $SiO_2$ mask was removed. Using the $SiO_2$ strips as hard masks, the exposed Al area was etched using Al etchant type A (Transene) and Al sidewalls were exposed between the $SiO_2$ hard mask and the substrate. However, the Al sidewalls were not vertical because of the isotropic nature of wet

etching. To make the sidewalls vertical, the Al was electropolished using a mixed solution of perchloric acid and ethanol (1:3 ratio) at 15 V for 5 ~ 15 sec. at room temperature (RT). Photoresist, PR, (AZ1518, Shipley) about 1.5 μm thick left on the $SiO_2$ was also used as a mask layer to prevent unwanted anodization of Al from the top surface through pin-holes in PECVD $SiO_2$.

*Anodization*:

Anodization of vertical Al sidewalls was carried out under various conditions, such as in 10 vol.% $H_2SO_4$, 0.3 M oxalic acid, and 5 wt.% $H_3PO_4$ at $V_{an}$ from 20 to 185 V for extended times, i.e., 2 to ~ 6 hrs.

## 3.3 Results and Discussion

Figure 3-1 shows a schematic illustration of our side anodization process for self-aligned H-AAO made by anodizing two vertical Al edges capped with a mask on a substrate. Figure 3-1 also shows the expected structure of the H-AAO, characterized by smooth inner pore walls and smoothly scalloped shapes of the barrier layer at the base of the pores, based on characteristics of V-AAO. A photoresist/$SiO_2$ capping layer was used as a mask that prevents anodization from the top surface of the Al. In side anodization, the anodic voltages and thickness of the Al films, $h_{Al}$, were carefully chosen to achieve the desired features of the resulting pore structures of the H-AAO, such as $D_s$, $D_p$, and the number of pore stacks $N_{ps}$ (monolayer or multilayer). For example, a monolayer ($N_{ps}$ = 1) and 10 layers ($N_{ps}$ = 10) of H-AAO with the $D_s$ of 500 nm and 50 nm formed when

anodizing 500nm-thick Al sidewalls at $V_{an}$ = 195 V and 20 V, respectively, or $N_{ps} \sim h_{Al}/D_s$ = $h_{Al}/2.5V_{an}$.

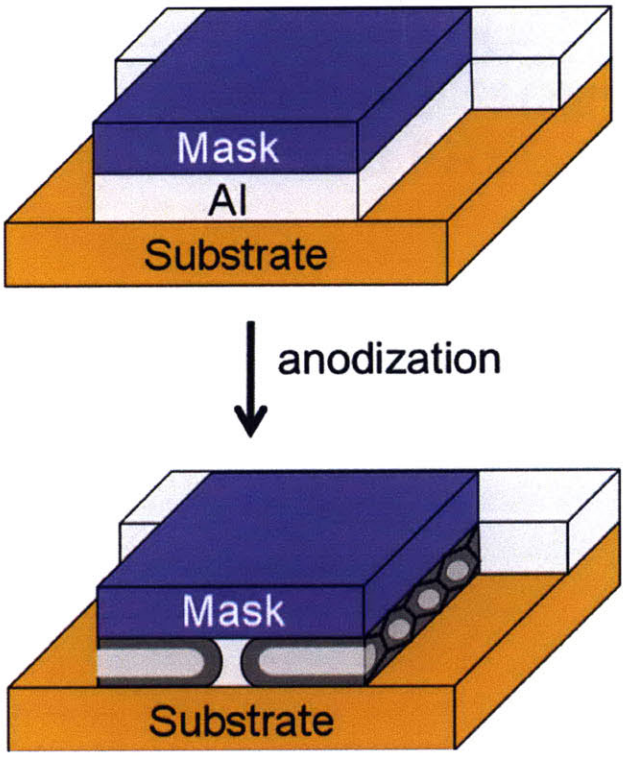


**Figure 3-1.** Schematic illustration of the process flow for fabrication of structures for formation of Horizontal-Anodized Aluminum Oxide (H-AAO). H-AAO structures were formed by anodizing vertical Al sidewalls capped with insulating masks on a substrate, made by patterning Al/insulating-layer lines. A multilayer of photoresist and $SiO_2$ deposited using Plasma-Enhanced Chemical Vapor Deposition (PE-CVD) was chosen for the mask, due to its mechanical and electrochemical inertness.

Figure 3-2 shows an SEM image of the self-ordered H-AAO monolayer with $D_s \sim$ 500 nm on a $SiO_2$ substrate, obtained by anodizing a 600 nm-thick confined Al vertical wall in 5 wt.% phosphoric acid at 185 V and 20°C for 6 hrs. For top view SEM observation, the PR was removed using acetone and rinsed using isopropanol and the $SiO_2$ was thinned to about 250 nm using reactive ion etching (RIE). In Fig. 3-2, it is clearly seen that two rows of H-AAO are produced as two exposed vertical Al sidewalls of an Al line were anodized. The length of the H-AAO pores is about 4.2 μm and is uniform along the edge of the Al line. As growth of H-AAO continued, pores became straight and regularly spaced, to form self-ordered lateral pore arrays. Notably, the ordering of lateral pores is often interrupted by oblique pores, which results in formation of lateral domains of ordered lateral pores with a domain size of ~ 6 μm, as expected from analogous behavior in bulk anodization [11, 12].

To investigate pore structures in H-AAO confined by two $SiO_2$ layers, cross-sectional scanning electron microscopy was used. Figure 3-3 shows a cross-sectional SEM image of a self-aligned H-AAO monolayer anodized for 6 hrs in 5 wt.% $H_3PO_4$ at 185V and 20°C. The pore structure of the H-AAO was expected be a monolayer of pores with smooth inner pore walls and smoothly scalloped shapes of the barrier layer at the base of the pore, as illustrated in Fig. 3-1. However, Fig. 3-3 (a) reveals dramatic differences compared to the schematic in Fig. 3-1. Despite the fact that a monolayer of AAO was formed, periodic secondary pore structures appeared at the inner walls of the pores, resulting in dendritic shapes. The periodicity of the secondary pores is about 85 nm at 20°C in 5 wt.% $H_3PO_4$ at $V_{an}$ = 185 V. This periodic dendritic structure also appears at

lower temperatures, 3 and 10°C, in the same electrolyte and at the same anodic voltage, but with shorter periodicity ~ 60 nm.

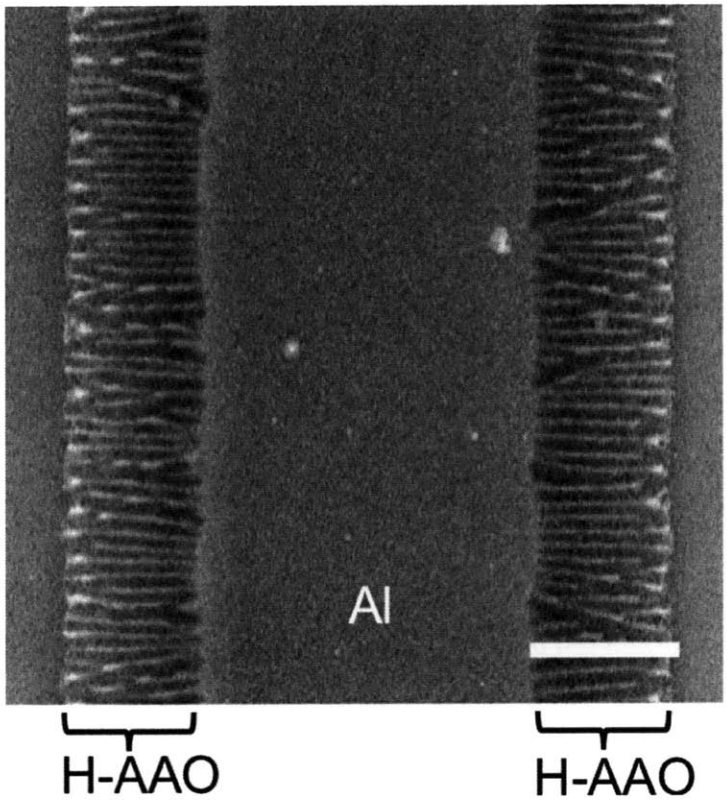


**Figure 3-2.** Plan-view Scanning Electron Microscopy (SEM) image of a self-aligned H-AAO monolayer with a pore spacing of $D_s$ ~ 500 nm, anodized for 6 hrs in 5 wt.% $H_3PO_4$ at $V_{an}$ = 185 V and 20°C. Scale bar = 10 μm.

We also conducted side anodization at/near other self-ordering anodization conditions, i.e. in oxalic acid at 40V and sulfuric acid at 20V, in order to determine if the

dendritic inner pore structure developed in these cases as well. Figure 3-3 (b) shows cross-sectional SEM images of H-AAOs formed by anodization for 2 hrs. at 3°C, in 10 vol.% sulfuric acid at 20V ($D_s$ = 50nm). Since $D_s < h_{Al} \sim 600$ nm, multilayers of multilevel pores formed with $N_{ps} \sim 15$ layers normal to the plane of the substrate surface. As seen in Fig. 3-3 (b), multi-level pores near the pore openings are straight and have smooth inner walls, but propagation of pores is eventually disrupted and dendritic pores form as the growth of H-AAO continues further into the Al. Similar pore structures developed in H-AAO with $D_s$ = 100 nm and $N_{ps} \sim 7$, when the pores were formed in 0.3 M oxalic acid at 40V. It should be noted that the $D_p$ of the straight pores was about 25 nm and decreased to less than 10 nm in the H-AAO, with $D_s$ = 100 nm, implying that an extra volume of $Al_2O_3$ expanded from the center of the primary pores as the dendrites formed. In addition, the pore/Al interfaces have convex curvature into the Al films while the outermost surface of the oxide remains straight. Since a pore grows in a direction normal to the Al surface, the growth of the pores follows the curvature change of the Al/H-AAO interface, which may facilitate the formation of dendrites, as seen in Fig. 3-3 (b). Nonetheless, the dendrites observed at the center of the H-AAO films in Fig. 3-3 (a) and (b) are a unique characteristic of H-AAO at self-ordering anodization conditions for prolonged times.

High-aspect-ratio cellular pores are hard to achieve in H-AAO, even after prolonged anodization time. For example, the length of H-AAO pores in Fig. 3-3 (b) is only about 570 nm after 2 hrs of anodization. Figure 4 summarizes the pore length for V-AAO and H-AAO with various values of $h_{Al}$, from 50 to 600 nm, and as a function of

time for anodization in 10 vol.% sulfuric acid at 3°C and 20 V. In general, the pore length of AAO, $L_{AAO}$, depends on the anodization time, t, according to $L_{AAO} \propto t^n$. The growth of V-AAO, as shown in Fig. 3-4, linearly increases (n = 1) with anodization time with a rate of ~ 240 nm/min, given a constant steady-state anodization current with a constant applied anodic voltage. On the other hand, the pore length for H-AAOs has a sub-linear dependence on time (n = 0.4 ~ 0.6). Moreover, the initial pore growth for H-AAO is further retarded as the Al film thickness is decreased, while changes in pore length after 5 min are similar for all H-AAOs with various $h_{Al}$ or various degrees of confinement. For instance, formation of 500 nm pores for H-AAO with $h_{Al}$ = 600 nm is 20 times slower than for unconfined V-AAO and 27 % of the pore growth for H-AAO occurs in less than 5 min. As seen in Fig. 3-3 (b), pores at/near the H-AAO/electrolyte interface, which formed early during the side anodization reaction, have straight and well-defined structures without dendritic side arms. Therefore, it can be deduced from Fig. 3-3 (b) and Fig. 3-4 that the development of dendrite structures in H-AAO accompanies kinetic retardation and can be avoided if the side anodization is performed under less aggressive confinement conditions, i.e. $h_{Al} > 500$ nm and $D_s < 50$ nm or $N_{ps} >> 10$, and for short anodization times (<5 min). However, abnormal H-AAO formation is inevitable for H-AAO for $N_{ps} < 10$, especially for $N_{ps} = 1$ under the anodization conditions associated with Fig. 3-3 (a) and (b). To produce cellular rather than dendritic horizontal pores with controlled $D_s$ and $N_{ps}$, it is important to understand differences in anodization in mechanically constrained structures compared to bulk anodization.

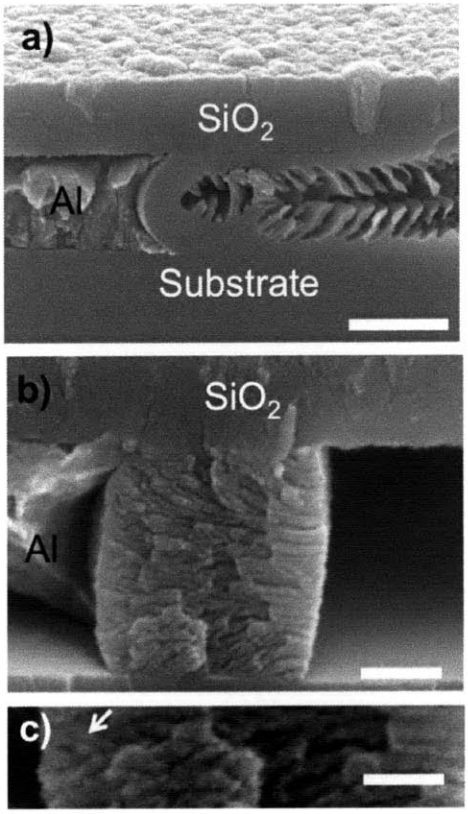


**Figure 3-3.** Cross-sectional SEM images of H-AAO anodized (a) for 6 hrs in 5 wt.% $H_3PO_4$ at $V_{an}$ = 185 V and 20°C, and (b) for 2 hrs in 10 vol.% $H_2SO_4$ at 20V and 3°C, respectively. Scale bars = 500 nm in (a), and 200 nm in (b). The pore spacing is fixed by the anodic voltage, $D_s$ ~ 2.5 nm/V, enabling control of the number of pore layers with respect to the thickness of the Al films. The dendritic structures were formed under all self-ordering anodization conditions. (c) a close-up image of the H-AAO shown in (b). An arrow indicates a dendritic structure. Scale bar = 100 nm.

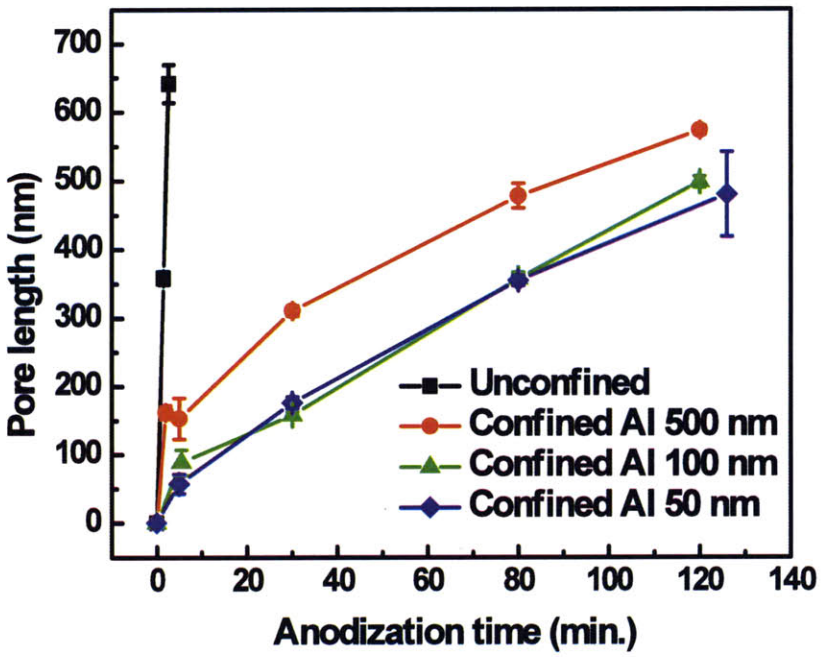


**Figure 3-4.** Length of V-AAO and H-AAO pores for various Al film thicknesses (50 ~ 600 nm) as a function of anodization time in 10 vol.% $H_2SO_4$ at 20 V and 3°C. Growth of H-AAO is significantly slowed due to mechanical confinement, for all the Al film thicknesses.

When aluminum oxide forms by oxidation of Al, the volume of $Al_2O_3$ that results is generally larger due to incorporation of oxygen ions and the volume expansion is represented by the Pilling-Bedworth ratio (PBR). The PBR defines the expected ratio of the volume of the produced $Al_2O_3$ over the volume of the reacted Al [25]. For barrier-type $Al_2O_3$ (planar non-porous alumina), for which the current efficiency $\eta$, the ratio of consumed electrical charge for electrochemical oxidation to form $Al_2O_3$ from Al to total the electrical charge provided, is close to 100 % and the PBR is 1.61 [26]. In the case of

porous AAO, where $\eta < 100$ %, however, the volume expansion, R, defined as the ratio of the thickness of the produced $Al_2O_3$, $h_{Al_2O_3}$, over the initial thickness of the reacted Al, $h_{Al}$, is often used instead of the PBR, because of incorporation of free space as pores in the AAO, and loss of volume of the $Al_2O_3$ and Al in the electrolyte during anodization. Typically, R is about 1.4 under self-ordering anodization conditions [12]. Therefore, in side anodization it is expected that the outermost H-AAO/electrolyte interface would move toward the electrolyte from the position of the initial Al/electrolyte interface, by sliding of the H-AAO between the $SiO_2$ layers, in order to accommodate the 140 % volume expansion. However, optical microscope images of a single Al line before and after side anodization in 5 wt. % $H_3PO_4$ at 185 V and 20°C reveal that the H-AAO/electrolyte interface has not moved relative to the position of the initial Al/electrolyte interface, implying that volume expansion of H-AAO does not occur.

In chapter 2, we reported that formation mechanisms for V-AAO are affected by both an electrochemical instability due to a field-assisted dissolution of the oxide and a mechanical instability due to strain developed in the AAO and Al. We argued that the period of the steady state pore structure is a consequence of the requirement that the rate of plastic deformation of the oxide match the rate of oxide formation. In addition, Garcia-Vergara et al. and Skeldon et al. also concluded that W tracer studies indicate that growth of V-AAO is maintained by plastic flow of the $Al_2O_3$ from the barrier oxide at the bases of the pores toward the pore walls [22, 23]. Moreover, Houser and Hebert recently suggested that steady-state growth of AAO could be quantitatively modeled when viscous flow of the oxide is assumed [24]. Hence, the volume expansion of anodic

alumina is maintained by plastic deformation and flow of the oxide during anodization. In side anodization, however, flow of $Al_2O_3$ toward the pore wall is inhibited by traction at the $SiO_2$ interfaces. Therefore, we postulate that the dendritic growth mode illustrated in Fig. 3-5 results from suppression of the plastic flow needed to accommodate the stress associated with the needed volume expansion, and the dendrite structures in Fig. 3-3 (a) and (b) form as a result of plastic flow in spaces surrounding the primary pore wall centers. While aluminum oxide is brittle, AAO is known to exhibit significant plasticity during anodization [27, 28]. Indeed, the formation of the dendritic structures in H-AAO was also observed in V-AAO when the flow was prohibited by local constraint, and, therefore, is a general characteristic of AAO formation in confined structures, and has been called a dendritic instability in chapter 2.

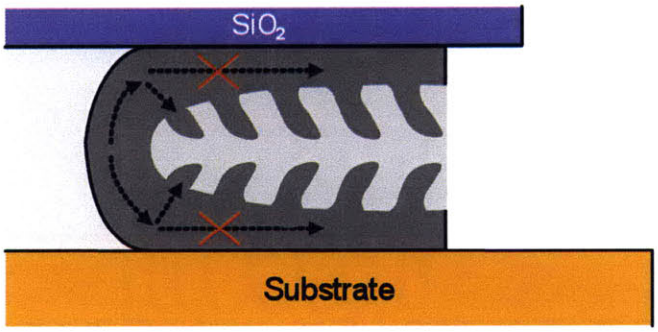


**Figure 3-5.** Schematic illustration of the formation mechanism of H-AAO with dendritic pore structures. Since volume expansion by plastic flow in the pore growth direction is inhibited due to traction at the $SiO_2$ mask interface, the extra volume of newly formed $Al_2O_3$ extrudes inside the primary pore, leading to the dendritic structure. Plasticity of the oxide in the presence of an electric field facilitates the extrusion.

The suppressed plastic flow of the oxide and the consequent formation of the secondary dendritic pores due to traction at the interface are also believed to affect the kinetics of anodic oxidation reaction. In V-AAO without constraint, a steady-state growth is achieved when a constant rate of anodic oxidation of Al is balanced by a constant rate of plastic flow of the oxide away from the tip of the pores. Therefore, when the plastic flow is suppressed by mechanical constraints, a reduced steady-state growth rate is expected for H-AAO.

From the arguments presented above, we expect that anodization conditions for which there is no volume expansion ($R \sim 1$) are required in order to minimize confinement effects, i.e. the dendrite instability and growth rate reduction observed for H-AAO. It is well-known that R depends on the anodic conditions, especially the current density or anodic voltage [29]. Figure 3-6 shows R as a function of the anodic voltage in 5 wt.% phosphoric acid at 3°C, as determined by measuring the thickness of anodized V-AAO from 600nm-thick Al films. R increases from 1.02 to 1.59 since a smaller pore volume results from the decreased pore density and the increased current efficiency $\eta$, as $V_{an}$ is increased from 20 V to 185 V. The growth rate of the V-AAO was measured and found to increase from 3.93 to 121.97 nm/min exponentially with anodic voltage. H-AAO was also formed from 600nm-thick Al films, in order to compare the formation kinetics and structures under the same anodization conditions for 120 ~ 135 min. Since the growth rate of H-AAO is not constant over time, the pore length of H-AAO, $L_{HAAO}$, was normalized by dividing by the pore length for V-AAO, i.e., $L_{HAAO}/ L_{VAAO}$, at a given anodization condition, to quantify the growth rate suppression in horizontal anodization.

Figure 3-6 shows $L_{HAAO}$ and $L_{HAAO}/ L_{VAAO}$ as a function of the R. Here, $L_{VAAO}$ was calculated based on the measured growth rate of V-AAO and the growth time. It is clearly seen that the normalized pore length of H-AAO decreases as R increases. For example, $L_{HAAO}$ is only 4.2 % of $L_{VAAO}$ at $V_{an}$ = 185 V. The normalized pore length of H-AAO increases and saturates at around 0.45, i.e., $L_{HAAO} \sim 0.45\ L_{VAAO}$, as R approaches 1 or at $V_{an} \leq 40$ V. Therefore, minimization growth retardation for horizontal anodization is achieved with R ~ 1, for which H-AAO forms without generating a compressive stress due to suppressed plastic flow of the oxide. The inner pore nanostructures in the H-AAOs shown in Fig. 3-6 were also investigated as a function of anodic voltage. Figures 3-7 (a) and (b) show corresponding cross-sectional SEM images of H-AAOs formed at $V_{an}$ = 86V and 20V, respectively. With fixed Al thickness = 600 nm, $N_{ps}$ the number of layers of pores in the H-AAO increases from a monolayer to ~ 12 layers with decreasing $V_{an}$, since $D_s \sim 2.5\ V_{an}$. When H-AAO was formed by anodization at $V_{an}$ = 86 V, with R = 1.37, as shown in Fig. 3-7 (a), the dendritic structure appears inside the pores. On the other hand, dendrite-free cellular H-AAO formed with $V_{an} \leq 40$ V and R ~ 1. For example, Figure 3-7 (b) shows dendrite-free H-AAO with $D_s \sim 50$ nm and $N_{ps} \sim 12$, anodized at 20 V.

Using these anodization conditions i.e., $V_{an} < 40$ V in 5 wt.% $H_3PO_4$ solution, we further fabricated dendrite-free horizontal pores with the number of layers of pores controlled varied by varying the Al film thickness. Figure 3-8 (a) shows ~ 6 layers of H-AAO pores with $D_s \sim 50$ nm, formed by anodizing 200 nm-thick Al films confined by $SiO_2$ at 20 V. Monolayers of H-AAO pores were also produced without dendrites with 50

and 75 nm-thick Al films and $V_{an}$ = 20 V and 30 V, as shown in Fig. 3-8 (b) and (c), respectively. Figure 3-8 (d) shows a top-view SEM image of the H-AAO monolayer anodized for 2 hrs. at the same conditions but at an elevated temperature, 20°C, to increase the growth rate. The length of the H-AAO pores increases by a factor of about 3.5 ~ 3.75 when the temperature is increased from 3°C to 20°C for fixed electrolyte concentrations and reaction times. However, the lateral ordering of the H-AAO in Fig. 3-8 (d) is poor compared to H-AAO anodized under self-ordering conditions, such as those used for Fig. 3-2. However, the V-AAO counterpart also exhibits poor ordering and the inter-pore confinement effect that leads to ordering has been removed by achieving conditions for which R=1. Therefore, while dendritic growth and growth rate reductions have been suppressed, templating may be required to achieve highly ordered H-AAO.

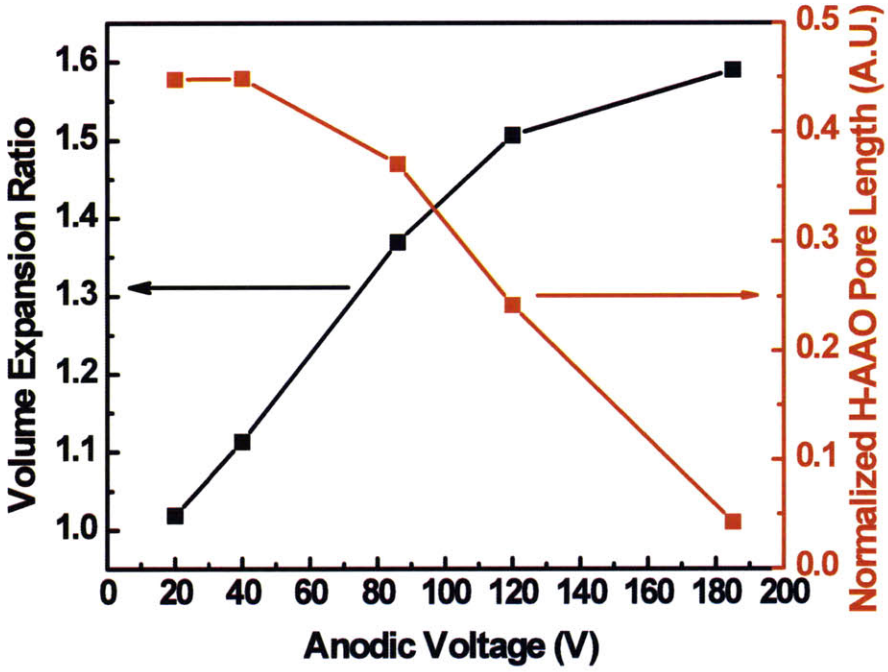


**Figure 3-6.** Volume expansion ratio of V-AAO and the normalized pore length of H-AAO as a function of anodic voltage in 5 wt.% $H_3PO_4$ at 3°C. The H-AAOs were grown for 120 ~ 135 min. at all anodization conditions and the pore length was normalized with respect to that of V-AAO at each anodic voltage at a given anodization time.

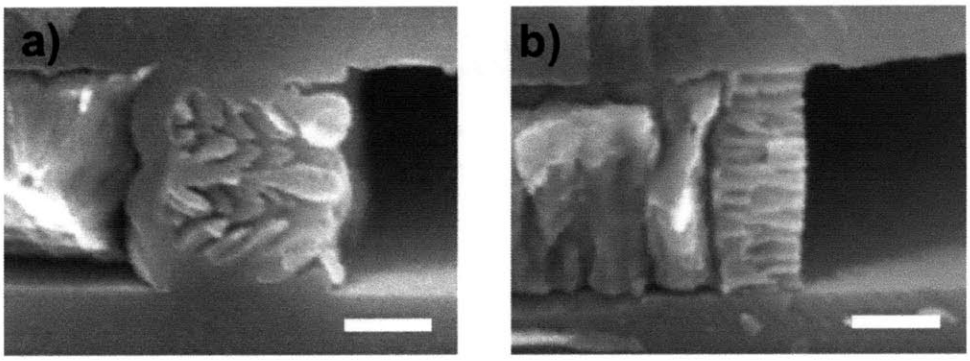


**Figure 3-7.** Cross sectional SEM images of the corresponding H-AAOs in Fig. 3-6, formed at (a) $V_{an}$ = 86 V, and (b) 40 V. Scale bars = 200 nm.

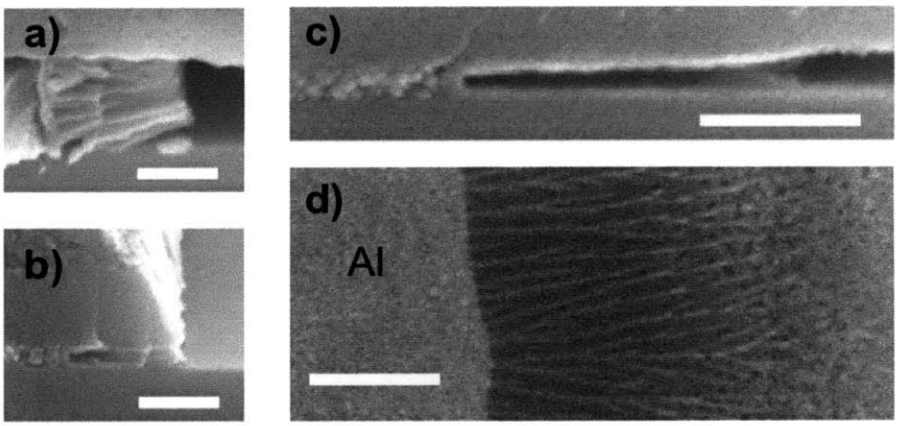


**Figure 3-8.** Cross sectional SEM images of dendrite-free H-AAO (a) ~ 6 layers by anodizing 200 nm-thick Al, and (b) a monolayer of pores obtained by anodizing 50 nm-thick Al at 20 V and 3°C for 2 hrs. (c) a monolayer of pores with $D_s$ ~ 75 nm obtained by anodizing 75 nm-thick Al at 30 V and 20°C for 2 hrs. Scale bars = 200 nm. (d) Plan-view SEM image of dendrite-free H-AAO anodized in 5 wt.% $H_3PO_4$ at 20°C and 20 V for 2hrs. Scale bar = 500 nm.

## 3.4 Conclusions

Highly ordered H-AAO was fabricated by anodizing vertical Al side walls confined by $SiO_2$ layers at self-ordering anodization conditions for prolonged times > 2 ~ 6 hrs. However, while domains of self-ordered H-AAO were achieved, it was found that dendrite nanostructures formed and the growth rate was significantly suppressed. We demonstrated that the kinetic retardation and dendritic structures originate from suppression of volume expansion due to suppressed plastic flow of the $Al_2O_3$ because of traction at the interfaces with the confining $SiO_2$ layers. In addition, a strategy was provided to avoid these abnormalities by using anodization conditions for which there is no volume expansion associated with formation of AAO from Al (R ~ 1). This was achieved by anodizing in 5 wt.% $H_3PO_4$ at values of $V_{an}$ from 20 to 40 V. Using this anodization condition, we successfully demonstrated dendrite-free H-AAO formation with a controlled number of pore layers, from monolayers to ~ 12 layers and with $D_s$ from 50 to 100 nm. However, the lateral ordering of the dendrite-free H-AAO was poor due to the lack of repulsive forces between the pores. These forces are normally associated with plastic deformation at the pore tip. Finally, the experimental procedure used in this work, i.e., the anodization of metals in a confined structure, can be used as a general methodology for the understanding pore formation mechanisms in other nanoporous anodic oxide, such as porous $TiO_2$.

## References


1. Martin, C.R., *NANOMATERIALS - A MEMBRANE-BASED SYNTHETIC APPROACH*. Science, 1994. **266**(5193): p. 1961-1966.
2. Xia, Y.N., et al., *One-dimensional nanostructures: Synthesis, characterization, and applications*. Advanced Materials, 2003. **15**(5): p. 353-389.
3. Kline, T.R., et al., *Template-grown metal nanowires*. Inorganic Chemistry, 2006. **45**(19): p. 7555-7565.
4. Taberna, L., et al., *High rate capabilities $Fe_3O_4$-based Cu nano-architectured electrodes for lithium-ion battery applications*. Nature Materials, 2006. **5**(7): p. 567-573.
5. Huang, Y., et al., *Directed assembly of one-dimensional nanostructures into functional networks*. Science, 2001. **291**(5504): p. 630-633.
6. Lu, W. and C.M. Lieber, *Nanoelectronics from the bottom up*. Nature Materials, 2007. **6**(11): p. 841-850.
7. Keller, F., M.S. Hunter, and D.L. Robinson, *Structural Features of Oxide Coatings on Aluminum*. Journal of the Electrochemical Society, 1953. **100**(9): p. 411-419.
8. Diggle, J.W., T.C. Downie, and C.W. Goulding, *Anodic oxide films on aluminum*. Chemical Reviews, 1969. **69**(3): p. 365-405.
9. O'Sullivan, J.P. and G.C. Wood, *The Morphology and Mechanism of Formation of Porous Anodic Films on Aluminium*. Proceedings of the Royal Society of London. A. Mathematical and Physical Sciences, 1970. **317**(1531): p. 511-543.

10. Oh, J. and C.V. Thompson, *Selective barrier perforation in porous alumina anodized on substrates*. Advanced Materials, 2008. **20**(7): p. 1368-1372.

11. Masuda, H. and K. Fukuda, *Ordered Metal Nanohole Arrays Made by a 2-Step Replication of Honeycomb Structures of Anodic Alumina*. Science, 1995. **268**(5216): p. 1466-1468.

12. Li, A.P., et al., *Hexagonal pore arrays with a 50-420 nm interpore distance formed by self-organization in anodic alumina*. Journal of Applied Physics, 1998. **84**(11): p. 6023-6026.

13. Lee, W., et al., *Fast fabrication of long-range ordered porous alumina membranes by hard anodization*. Nature Materials, 2006. **5**(9): p. 741-747.

14. Masuda, H., et al., *Highly ordered nanochannel-array architecture in anodic alumina*. Applied Physics Letters, 1997. **71**(19): p. 2770-2772.

15. Krishnan, R., et al., *Wafer-level ordered arrays of aligned carbon nanotubes with controlled size and spacing on silicon*. Nanotechnology, 2005. **16**(6): p. 841-845.

16. Meng, G.W., et al., *Controlled fabrication of hierarchically branched nanopores, nanotubes, and nanowires*. Proceedings of the National Academy of Sciences of the United States of America, 2005. **102**(20): p. 7074-7078.

17. Lee, W., R. Scholz, and U. Gösele, *A continuous process for structurally well-defined $Al_2O_3$ nanotubes based on pulse anodization of aluminum*. Nano Letters, 2008. **8**(8): p. 2155-2160.

18. Masuda, H., K. Nishio, and N. Baba, *Fabrication of a One-Dimensional Microhole Array by Anodic-Oxidation of Aluminum*. Applied Physics Letters, 1993. **63**(23): p. 3155-3157.

19. Cojocaru, C.S., et al., *Conformal anodic oxidation of aluminum thin films*. Nano Letters, 2005. **5**(4): p. 675-680.

20. Gowtham, M., et al., *Controlled fabrication of patterned lateral porous alumina membranes*. Nanotechnology, 2008. **19**(3): p. 035303.

21. Xiang, Y., et al., *Microstructured horizontal alumina pore arrays as growth templates for large area few and single nanowire devices*. Physica Status Solidi-Rapid Research Letters, 2008. **2**(2): p. 59-61.

22. Garcia-Vergara, S.J., et al., *A flow model of porous anodic film growth on aluminium*. Electrochimica Acta, 2006. **52**(2): p. 681-687.

23. Skeldon, P., et al., *A tracer study of porous anodic alumina*. Electrochemical and Solid State Letters, 2006. **9**(11): p. B47-B51.

24. Houser, J.E. and K.R. Hebert, *The role of viscous flow of oxide in the growth of self-ordered porous anodic alumina films*. Nat Mater, 2009. **8**(5): p. 415-420.

25. Pilling, N.B. and R.E. Bedworth, J. Inst. Met., 1923. **1**: p. 529-582.

26. Pringle, J.P.S., *The Anodic-Oxidation of Superimposed Metallic Layers - Theory*. Electrochimica Acta, 1980. **25**(11): p. 1423-1437.

27. Bradhurst, D.H. and J.S.L. Leach, *The Mechanical Properties of Thin Anodic Films on Aluminum*. Journal of the Electrochemical Society, 1966. **113**(12): p. 1245-1249.

28. Wüthrich, N., *Intrinsic stresses in anodic films on aluminium*. Electrochimica Acta, 1981. **26**(11): p. 1617-1623.

29. Vrublevsky, I., et al., *The study of the volume expansion of aluminum during porous oxide formation at galvanostatic regime*. Applied Surface Science, 2004. **222**(1-4): p. 215-225.

# Chapter 4. Selective Barrier Perforation in Porous Alumina Anodized on Substrates

## 4.1 Introduction

Anodic aluminum oxide (AAO) formed from films on substrates can have mono-disperse pores with diameters as low as a few tens of nanometers and with lengths of tens of micrometers [1, 2]. At specific anodization conditions, domains of close-packed pore arrays form, with interpore spacing $D_s$ from 50 nm to 500 nm [1-4]. Pores typically are only ordered within domains, and $D_s$ and the pore diameter $D_p$ can not be varied separately. However, with pore formation guided by lithographically defined templates, pores with perfect long range order, with controlled ordering symmetry (including symmetries other than close-packed), with controlled pore locations, and with independently controlled $D_s$ and $D_p$, can be produced [3, 5-7]. Control of these characteristics in porous AAO (PA) is key for producing ideal templates for growth of mono-disperse nanowires and nanotubes, and for use as a scaffolds that separate and align wires and tubes for electrical connection and integration with other materials and devices. To facilitate the functional integration of these nanostructures, layers of ordered porous AAO (OPA) with through-pore contact to electrically conducting underlayers is desirable.

However, anodization of aluminum on a conducting underlayer, for subsequent through-pore electrical connections, faces two significant challenges. First, the insulating barrier oxide at the base of the pores should be etched without widening the pore

diameter or detaching the PA from the substrates. Second, the underlying contact layer should not react electrochemically in an uncontrollable manner after Al anodization is complete. A metal underlayer can not be used if anodization of the underlayer itself involves reactions that might hinder uniform anodization over large-area substrates, lead to detachment of the PA from the substrate, or leave insulating by-products that can not be removed.

Currently, the most widely used underlayers for PA are noble metals such as Pt [1, 6]. However, this leads to formation of an inverted barrier oxide (Figure 4-1 (b)) that leads to pore broadening at the base [1]. Conventional chemical etching processes for barrier oxide removal also result in enlargement of the pore diameter (Figure 4-1 (d)), due to the isotropic nature of PA etching. Barrier thinning techniques based on decreasing the anodization voltage [6] or using a reverse bias in KOH [1] and sulfuric acid [2] have been applied to minimize pore widening while removing the barrier layer. However, Au and Pt underlayers catalyze electrolysis of water at anodization or reverse bias conditions, so that bubbles of oxygen gas ($H_2$ gas when a reverse bias is applied) violently evolve when the noble metal interface is reached [1, 2]. Consequently, voids form at the oxide/metal interface and eventually the PA delaminates from the substrate, even when thin Ti adhesion layers are used [1, 2]. Therefore, noble metals do not provide appropriate contact layers beneath PA.

If a metal is used as an underlayer that also oxidizes under Al anodization conditions and has an oxide with a higher ionic conductivity than alumina, the underlayer oxide will penetrate the alumina barrier oxide [8] and grow into the alumina pores [9].

The oxides of Ti, Ta, and Nb have higher ionic conductivity than alumina and are known to penetrate the barrier layer of porous alumina (Figure 4-1 (c)) [9]. Therefore, by selectively etching the penetrating oxide, which is insulating as well, the base of the alumina pores can be opened without etching of the PA. However, $TiO_2$, $Ta_2O_5$, and $Nb_2O_5$ are chemically stable in aqueous solution. If the oxide that forms is semiconducting, it can still be used to electrodeposit materials in the pores, but not to make ohmic contacts to underlying metallic layers. Iwasaki et al. reported electro-deposition of cobalt catalyst particles in PA on Nb, without post-anodization etching of $Nb_2O_5$ [10]. In this case, electrical contact was made through a semi-conducting $NbO_2$ layer created by thermal reduction of insulating $Nb_2O_5$ in a reducing ambient at 500°C, which did not provide direct and complete ohmic contact to the underlying Nb. Furthermore, the pores were also widened significantly in dilute phosphoric acid etching before the thermal reduction process. Direct ohmic contact to metallic underlayers by removal of the penetrating oxides (e.g. $TiO_2$, $Ta_2O_3$, and $Nb_2O_5$) has not been reported in earlier studies. In this chapter, we show that tungsten also forms an oxide that can penetrate the PA barrier oxide, but that tungsten oxide can be readily and selectively etched in aqueous solutions to open PA pores and expose the metallic W layer at the bottom of the pores, without pore widening.

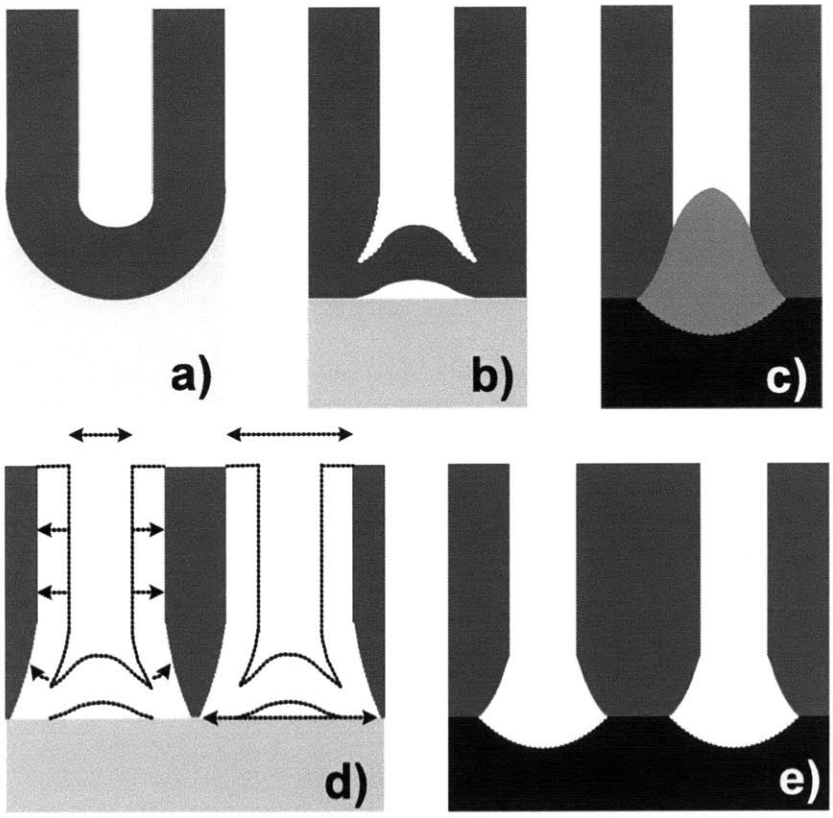


**Figure 4-1.** Schematic diagrams of porous alumina formed on different underlayers: (a) Scallop-shaped barrier oxide forms on Al [1]; (b) An inverted barrier oxide forms on noble metals with a void at the base of the pore [1]; (c) When ionic conduction is higher in the oxide of the underlying layer, and the layer oxidizes under the same conditions as the aluminum, the oxide of the underlayer (e.g., Ta and Nb) penetrates the bottom of the pores [9]; (d) The diameter of the pore is widened when alumina etching is used to clear the barrier oxide at the base of the pores. Note the decreased contact area between the PA and the underlayer; (e) The result of selective etching of $WO_3$ protruding into the pores, as in (c).

## 4.2 Experiments

*Al/W bilayers*

W (60 nm)/Ti (15 nm) bilayers were deposited on thermally oxidized Si substrates using multi-source e-beam evaporation. The base pressure was $1x10^{-6}$ Torr and the thickness of the films was determined using a quartz crystal monitor. Ti serves as an adhesion layer for W on $SiO_2$. 500 nm-thick Al layers were deposited after W deposition was complete.

*Pre-patterning of Al/W layers*

Al/W bilayers were coated with a negative photoresist (Ohka-PS4) and anti-reflection coating (ARC, XHRi-11). The resist and ARC stack was patterned using interference lithography using a Lloyd's mirror arrangement and double exposure at right angles, to expose square arrays with a periodicity of 200 nm [11]. After the pattern was transferred to the ARC layer using an $O_2$ plasma, dimples on the Al surface were made by wet etching the exposed Al (Al etchant type A, Transene).

*Anodization*

In the case of mild anodization, the pre-patterned Al/W layers were anodized using a 5 wt.% phosphoric acid solution at a constant voltage of 86 V and at room temperature. In the case of hard anodization, a constant voltage of 100 V was applied in 0.3 M oxalic acid at 3°C, after the Al/W bilayers were first anodized for 2.5 minutes under mild anodization conditions. Disordered PA was also fabricated by anodizing un-

patterned Al/W bilayers with 10 vol.% sulfuric acid at 20 V and 3°C and 0.3 M oxalic acid at 40 V and 3°C, respectively. To promote the penetration of $WO_3$ into $Al_2O_3$ barrier oxide, anodization was continued for about 1 to 2 min., without changing any anodization parameters, after the current first began to decrease. A mesh of platinum wires was used as the cathode.

The $WO_3$ in the PA was removed using a pH 7 buffer solution (a mixture of sodium phosphate and potassium phosphate with pH = 7.00 at 25°C, The VWR International) at room temperature. The typical etching time was 10 min for all samples.

*Ni nanowire growth*

Nickel was electroplated from a Watts bath (containing 300 g/L $NiSO_4.6H_2O$, 45 g/L $NiCl_2.6H_2O$, 45 g/L $H_3BO_3$, pH 4.5) using a platinum anode at room temperature. A constant current density of 1 to 2 $mA/cm^2$ was maintained during electrodeposition. When the cathodic voltage began to drop slightly from the saturation value (about -2 V ~ -2.15 V), the deposition was stopped.

For fabrication of free-standing nanowires, the OPA scaffold was removed using a mixture of 1.8 wt.% chromic acid and 6 wt% phosphoric acid at 65 °C for 2 hrs. After the OPA was removed, the sample was rinsed with acetone and isopropanol. In some cases (e.g. Figure 4-5 (c)), Ni wires in the OPA scaffold were annealed at 450°C in forming gas for 1 hr before the OPA was selectively removed. In other cases (e.g. Figure 4-5 (d)), the Ni was not annealed.

## 4.3 Results and Discussion

Figure 4-2 (a) shows a current-time (I-t) curve for anodization of an Al/W bilayer in 5 wt.% phosphoric acid at a constant voltage of 86 V and room temperature (RT). During anodization of Al/Au or Al/Pt bilayers, the current surges abruptly as gas evolution occurs when the alumina barrier layer reaches the Au or Pt interface [1]. In contrast, as seen in Figure 4-2 (a), for Al/W bilayers the current drops gradually and saturates after the alumina barrier oxide interface reaches the tungsten layer and an anodic oxide of tungsten forms. Figure 4-2 (b) shows a scanning electron microscope (SEM) image of a cross-section through a pore that has reached the final state shown in the current-time curve. This SEM image clearly shows $WO_3$ protruding through the barrier oxide, while the pore structures otherwise remain intact. Since the ionic conductivity of $WO_3$ is higher than that of $Al_2O_3$ (the electric field for the ionic transport in $WO_3$ is about 5. 6 to $5.9x10^6$ V/cm, while that in alumina $8.3x10^6$ V/cm [12]), anodic $WO_3$ forms preferentially when W is exposed to anodizing species, such as $OH^-$ or $O^{2-}$ ions. The large volume change associated with oxidation of W (Pilling-Bedworth ratio of 3.6 [12]) may also help $WO_3$ to penetrate the PA barrier oxide. It should be noted that the features shown here (the I-t curve and penetration of tungsten oxide into the pores) are general to other anodization conditions, including anodization using sulfuric or oxalic acid.

Since $WO_3$ is insulating, it must be removed selectively with respect to $Al_2O_3$ for ohmic contact through the pores. Figure 4-3 shows the equilibrium ion concentrations in

an aqueous solution with α-alumina and $WO_3$, as a function of pH at room temperature. Dissolution reactions for alumina in aqueous solution are given by [13]

$$2Al^{3+} + 3H_2O = Al_2O_3 + 6H^+ \quad (1)$$

and

$$Al_2O_3 + H_2O = 2AlO_2^- + 2H^+ . \quad (2)$$

From these reactions, the equilibrium concentrations of aluminum and aluminate ions are given by [13]

$$\log[AlO_2^-] = \frac{\mu^\circ_{Al_2O_3} + \mu^\circ_{H_2O}}{2RT \cdot 2.303} + pH = -11.76 + pH \quad (3)$$

and

$$\log[Al^{3+}] = \frac{\mu^\circ_{Al_2O_3} - 3\mu^\circ_{H_2O}}{2RT \cdot 2.303} - 3pH = 8.55 - 3pH, \quad (4)$$

where $\mu^\circ_{Al_2O_3}$ and $\mu^\circ_{H_2O}$ are the standard chemical potentials of aluminum oxide (solid) and water (liquid), respectively. From equation (3) and (4), it can be seen that alumina will dissolve in strongly acidic or strongly basic solutions, such as phosphoric acid or potassium hydroxide solutions, respectively. However, the dissolution of alumina is negligible in mildly acidic or basic solutions.

The influence of pH on the solubility of tungsten oxide is given by the following reaction [13],

$$WO_3 + H_2O = WO_4^{2-} + 2H^+ . \quad (5)$$

The equilibrium concentration of tungsten oxide ions in aqueous solution is given by [13]

$$\log[WO_4^{2-}] = \frac{\mu^\circ_{WO_3} + \mu^\circ_{H_2O}}{RT \cdot 2.303} + 2pH = -14.05 + 2pH, \quad (6)$$

where $\mu^{o}_{WO_3}$ and $\mu^{o}_{H_2O}$ are the standard chemical potentials of $WO_3$ (solid) and water (liquid), respectively. From equation (6) and figure 4-3 it can be seen that $WO_3$ is stable in an acidic environment but will dissolve in neutral and basic solutions.

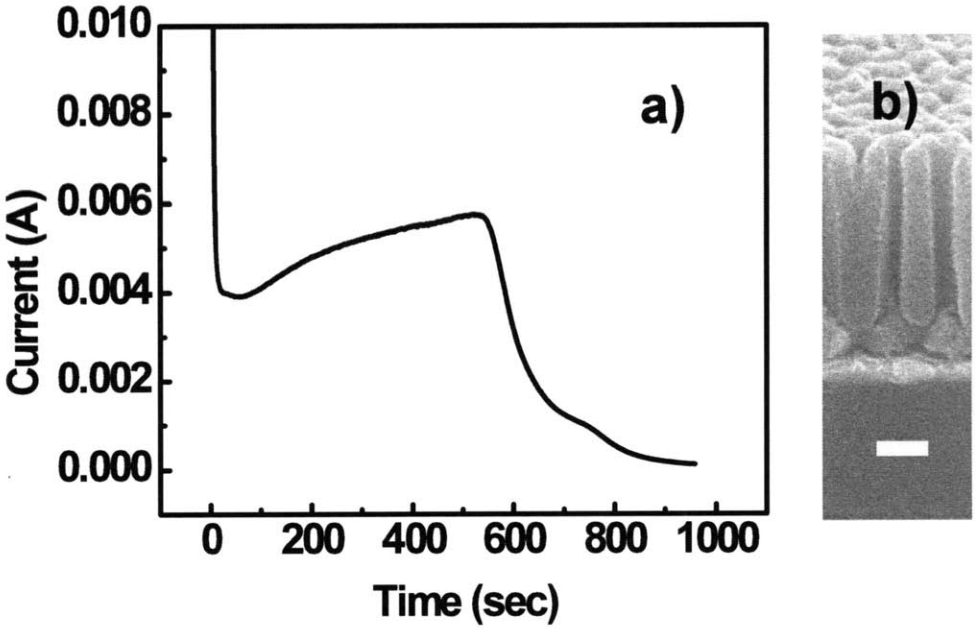


**Figure 4-2.** (a) A current-time curve for anodization of an Al/W/Ti multilayer film deposited on oxidized silicon substrates; (b) A cross-sectional scanning electron microscope image of a corresponding anodized Al/W/Ti multilayer. Note the protrusion of $WO_3$ into the alumina pores, as schematically illustrated in Figure 4-1 c. (The scale bar = 200 nm.)

At pH = 7, the equilibrium concentration of $WO_4^{2-}$ is about 1 mol/L, while that of $AlO^{2-}$ is $1.74 \times 10^{-5}$ mol/L. Therefore, an aqueous solution with pH = 7 will dissolve $WO_3$ without etching $Al_2O_3$.

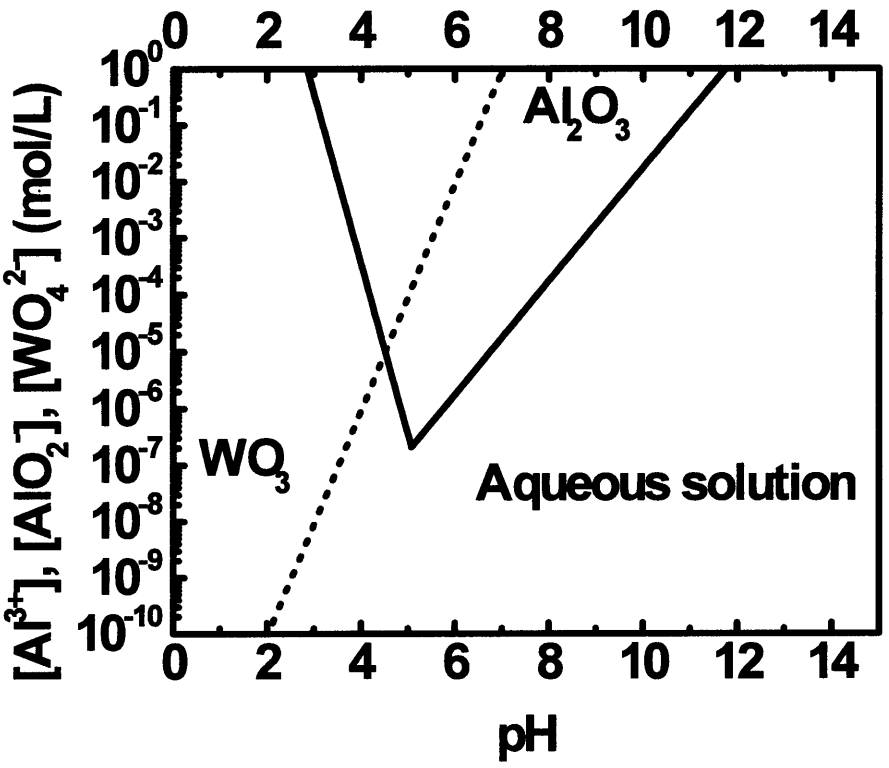


**Figure 4-3.** The influence of pH on dissolution of $Al_2O_3$ and $WO_3$. Based on data in reference 13.

Figure 4-4 shows cross sectional SEM images that illustrate the formation and selective etching of $WO_3$ in the perfectly ordered PA films formed on W underlayers. By templating the original Al surface with a di-periodic pattern of dimples with square ordering symmetry, perfectly ordered PA layers on W were fabricated, with pores arranged with square symmetry, with a pore spacing of 200 nm, and with pore diameters

of 83 nm or 55 nm. The larger-diameter pores were obtained using 'mild' anodization conditions, 5 wt.% phosphoric acid at 86 V and room temperature, and the 55 nm-diameter pores were obtained using 'hard' anodization conditions, 0.3 M oxalic acid at 100 V and 3°C [7, 14]. The pores with varied diameters, shown in Figures 4-4 (c) and (d), were anodized first under mild conditions, and then under hard conditions [7, 14].

It can clearly be seen that the protruding $WO_3$ in Figures 4-4 (a) and (c) is selectively removed (Figures 4-4 (b) and (d)) in a pH 7 buffer solution, without modification of the AAO pore structure. The top diameter of the pore increased negligibly, from 83 nm to 83.8 nm, after etching, while that of the bottom of the pore widened due to the shape of the protruding $WO_3$. Again, it should be noted that the process of sacrificial oxidation and selective removal of $WO_3$ works for anodization with different electrolytes (sulfuric and oxalic acid) and different voltages, as shown in Figure 4-5.

Figure 4-6 shows SEM images of Ni nanowires grown in long-range-ordered PA prepared as described above. In Figure 4-6 (a) and (b), Ni nanowires with aspect ratios of 6.9 were grown to a uniform height and with a filling ratio > 97 %, indicating complete removal of the insulating barrier oxide and $WO_3$. Figures 4-6 (c) and (d) show free-standing Ni nanorods obtained after selective removal of the OPA scaffold using a mixture of phosphoric and chromic acid at 65°C.

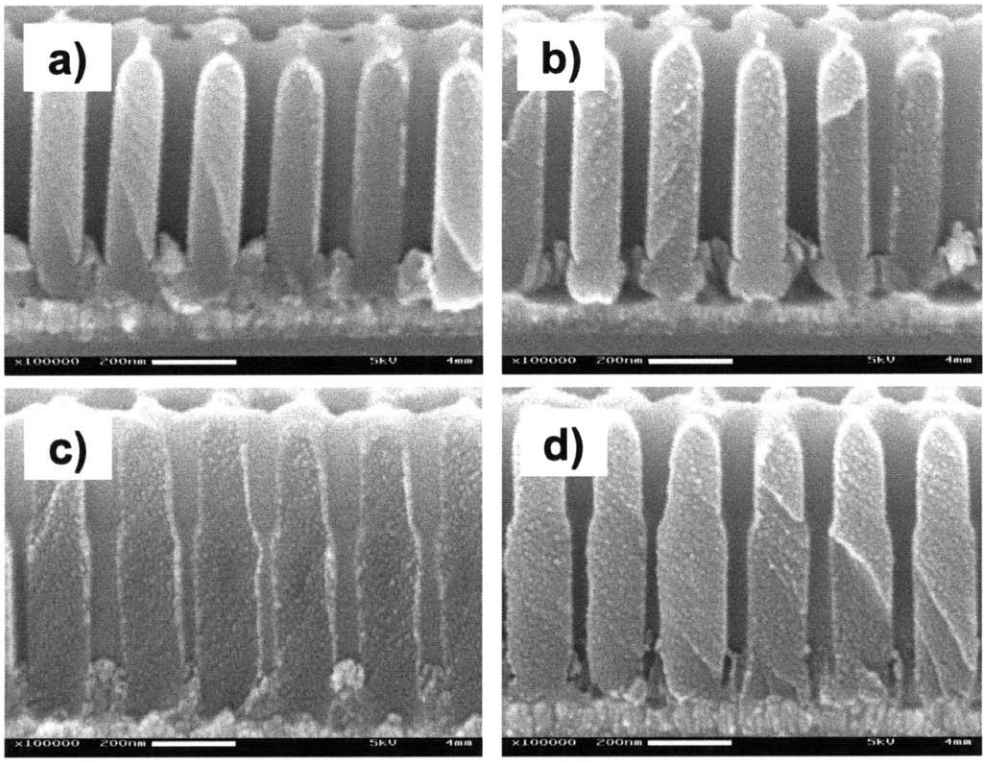


**Figure 4-4.** Pore opening through selective removal of $WO_3$: (a) SEM image of ordered porous alumina (OPA) formed on a W underlayer using mild anodization conditions (86 V, 5 wt.% phosphoric acid solution); (b) A sample like the one in a), after selective removal of the $WO_3$ that penetrates the pores. The anodic $WO_3$ was selectively removed using a pH 7 buffer solution; (c) OPA formed on W underlayers using hard anodization conditions (100 V, 0.3 M oxalic acid solution) followed by mild anodization conditions [as in (a) above]; (d) A sample like the one in (c), after selective removal of the $WO_3$ that penetrates the pores. (The scale bars = 200 nm).

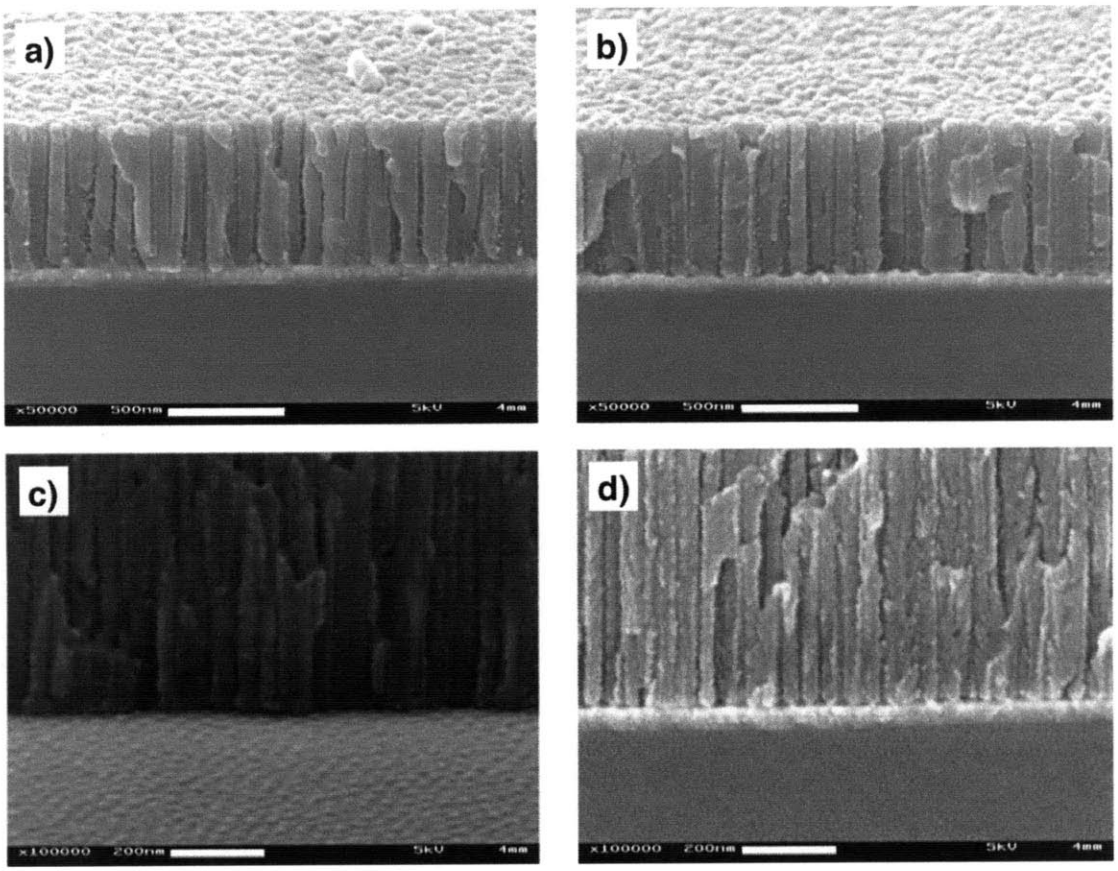


**Figure 4-5.** Selective barrier perforation process with oxalic and sulfuric acid anodization: (a) SEM image of AAO formed on W at 40 V with 0.3 M oxalic acid solution. The $WO_3$ protrusions have penetrated the barrier oxide of the alumina; (b) Anodic $WO_3$ created by anodization in oxalic acid is selectively removed from alumina pores using a pH 7 buffer solution. The bottom of the pores has been opened without significant pore widening; (c) AAO formed on W in sulfuric acid (20 V, 10 vol.% sulfuric acid solution). The $WO_3$ protrusions have penetrated the barrier oxide of the alumina; (d) Anodic $WO_3$ created by anodization in sulfuric acid was selectively removed from alumina pores using a pH 7 buffer solution. In both cases, anodization was carried out using untemplated Al at 3°C.

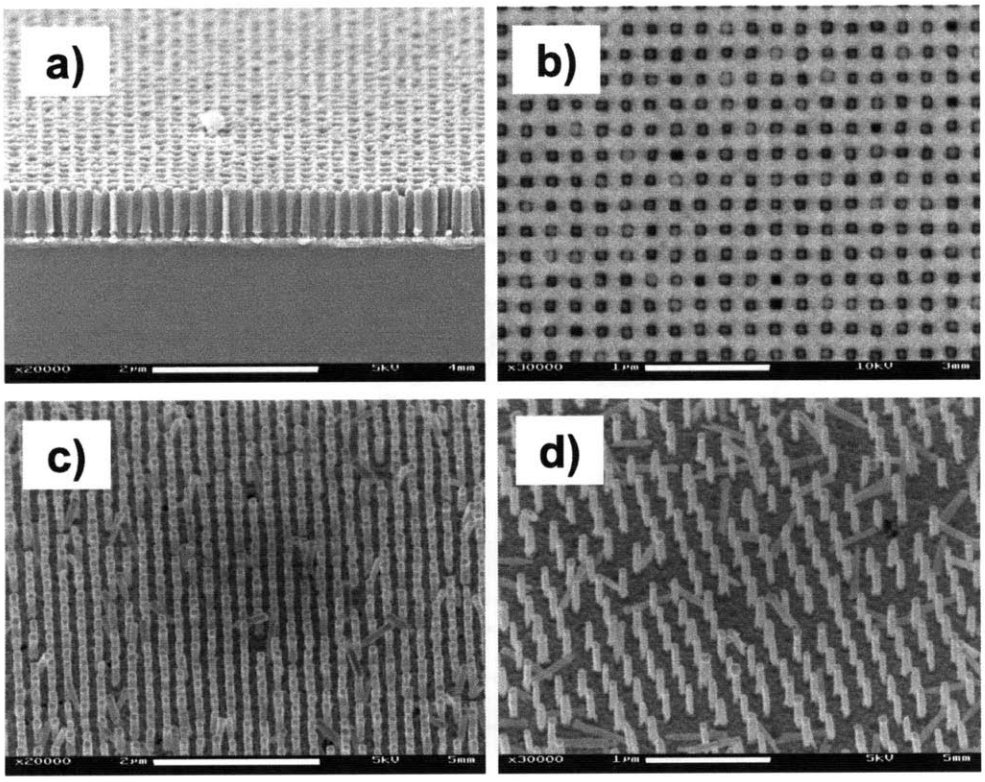


**Figure 4-6.** Perfectly ordered Ni nanowire arrays: (a) Cross-sectional SEM image of arrays of Ni nanowires grown by electrodeposition in an OPA scaffold, with square ordering symmetry and with a periodicity of 200 nm (The scale bar = 2 μm); (b) top-view SEM image of Ni nanowire arrays in an OPA scaffold (The scale bar = 1 μm); (c) SEM image (at a tilt of 30°) of a free-standing Ni nano-electrode array made by selective etching of porous alumina scaffolds of the type shown in (a) and (b). The nanowire spacing is 200 nm and the diameters are 83 nm. (The scale bar = 2 μm); (d) SEM image (at a tilt of 30°) of a free-standing Ni nano-electrode array with a wire spacing of 200 nm and diameter of 55 nm (The scale bar = 1 μm).

## 4.4 Conclusions

A new method for perforation of the barrier layer in ordered porous alumina has been developed, based on anodization of Al/W bilayer films and selective removal of tungsten oxide. This technique does not lead to pore widening, and uniformly opens pores over large areas without damaging or causing delamination of the porous alumina. This technique has been demonstrated through the templated growth of perfectly ordered uniform arrays of Ni nanowires with different wire diameters but the same wire spacing.

## References


1. Rabin, O., et al., *Formation of thick porous anodic alumina films and nanowire arrays on silicon wafers and glass*. Advanced Functional Materials, 2003. 13(8): p. 631-638.
2. Tian, M.L., et al., *Penetrating the oxide barrier in situ and separating freestanding porous anodic alumina films in one step*. Nano Letters, 2005. 5(4): p. 697-703.
3. Masuda, H., K. Yada, and A. Osaka, *Self-ordering of cell configuration of anodic porous alumina with large-size pores in phosphoric acid solution*. Japanese Journal of Applied Physics Part 2-Letters, 1998. 37(11A): p. L1340-L1342.
4. Li, A.P., et al., *Hexagonal pore arrays with a 50-420 nm interpore distance formed by self-organization in anodic alumina*. Journal of Applied Physics, 1998. 84(11): p. 6023-6026.
5. Krishnan, R., et al., *Wafer-level ordered arrays of aligned carbon nanotubes with controlled size and spacing on silicon*. Nanotechnology, 2005. 16(6): p. 841-845.
6. Choi, J.S., et al., *Monodisperse metal nanowire arrays on Si by integration of template synthesis with silicon technology*. Journal of Materials Chemistry, 2003. 13(5): p. 1100-1103.
7. Lee, W., et al., *Fast fabrication of long-range ordered porous alumina membranes by hard anodization*. Nature Materials, 2006. 5(9): p. 741-747.
8. Pringle, J.P.S., *The Anodic-Oxidation of Superimposed Metallic Layers - Theory*. Electrochimica Acta, 1980. 25(11): p. 1423-1437.

9. Mozalev, A., et al., Electrochim. Acta, 2003. 48: p. 3155-3170.

10. Iwasaki, T., T. Motoi, and T. Den, *Multiwalled carbon nanotubes growth in anodic alumina nanoholes*. Applied Physics Letters, 1999. 75(14): p. 2044-2046.

11. Farhoud, M., et al., *Fabrication of 200 nm period nanomagnet arrays using interference lithography and a negative resist*. Journal of Vacuum Science & Technology B, 1999. 17(6): p. 3182-3185.

12. Iglesias-Rubianes, L., et al., J. Electrochem. Soc., 2002. 149: p. B23-B26.

13. Pourbaix, M., *Atlas of electrochemical equilibria in aqueous solution*. 1974, Houston: National Association of Corrosion Engineers.

14. Krishnan, R. and C.V. Thompson, *Monodomain high-aspect-ratio 2D and 3D ordered porous alumina structures with independently controlled pore spacing and diameter*. Advanced Materials, 2007. 19(7): p. 988-992.

# Chapter 5. A Tungsten Interlayer Process for Fabrication of Through-pore Anodic Aluminum Oxide (AAO) Scaffolds on Any Substrate

## 5.1. Introduction

Arrays of one-dimensional (1-D) nanomaterials have attracted much attention for various applications in electronic, optical, and energy storage devices [1-5]. Nanoporous materials as scaffolds have been successfully demonstrated to provide effective routes to the growth and assembly of the vertically aligned 1-D nanomaterials over very large areas on various substrates [2, 6-8]. Thin film nanoporous anodic aluminum oxide (AAO), in particular, has been extensively studied because of the ability to produce ordered pore arrays with tunable nanostructural features [9-12]. Thin films of AAO are formed by anodizing Al films on a substrate that offers mechanical support and often functionality for vertically aligned 1-D nanomaterials as desired for specific applications [13-20]. For example, AAO scaffolds have been grown directly on substrates with electrical conductivity (Pt, Ti, W, and etc) [14-16], optical transparency (glass and indium tin oxide (ITO)) [17, 18], and/or mechanical flexibility (polydimethylsiloxane (PDMS)) [19]. Moreover, a substrate under an AAO scaffold can allow epitaxial growth of semiconductor nanowires from the substrate surface at the pore bottom, such as epitaxial growth of (100) Si nanowires on (100) Si surfaces, by constraint of the vapor-liquid-solid (VLS) mechanism [20].

In practice, however, an additional barrier removal process is required to expose the substrate surface at the pore bottom, since a thin layer of $Al_2O_3$, the barrier layer, separates the pores from the substrates after anodization [10-12]. The barrier layer can be removed by chemical etching (typically in diluted phosphoric acid), but this results in a significant widening of the pores that makes it difficult to provide scaffolds for small-diameter 1-D nanomaterials as defined by the etched AAO scaffold [13, 18, 20]. Furthermore, a substrate can react electrochemically after Al anodization is complete. Metals, such as Pt, and ITO, violently produce $O_2$ gas from water electrolysis under anodic conditions (or $H_2$ gas in cathodic conditions) which leads to non-uniform anodization over large-area substrates and detachment of the AAO from the substrate [14, 17, 18]. Oxidative metals, such as Ta [21] and Nb [22] leave insulating and semi-conducting by-products that are difficult to selectively remove with respect to $Al_2O_3$.

To fully utilize the important structural features of AAO scaffolds for assembly of vertically aligned 1-D nanomaterials, it is highly desirable to develop a process for fabrication of AAO scaffolds on any substrate (AS) and expose the surface of the substrate under at the base of the pore without widening of pores. So far, fabrication of through-pore AAO structures has only been realized without pore widening for a limited set of substrates, such as Ti and W [14-16].

In chapter 4, we reported a new method for perforation of the barrier $Al_2O_3$ layer without pore widening and decohesion of the AAO. In this method, a thin tungsten film under the Al was used to form an anodic tungsten oxide that penetrates the barrier layer at the base of the pores. A selective chemical etching process was developed to selectively

remove the penetrated anodic $WO_3$ and expose the surface of the metallic W underlayer at the base of the pore, without pore widening.

In this chapter, we describe development of a W-interlayer process as a general strategy for fabrication of a small-diameter through-pore AAO on any substrate (through-pore AAO/AS) under various anodization conditions without increasing the pore diameter. The process is based on the previously reported barrier perforation technology using a tungsten underlayer, but we further refine the process to expose surfaces of any substrate, not just W, at the pore bottom. First, we report that anodic oxidation of W results in barrier type $WO_3$ formation, which reaction is self-terminating with application of a constant anodic voltage in porous AAO-forming electrolytes. Then, we determine the consumed thickness of the remaining W layer for the anodic oxidation under a variety of conditions. A through-pore AAO/AS structure (in the present case, to Au substrates) was fabricated by anodization of multilayer structures, i.e., Al/W/AS, with W interlayers with precisely controlled thickness so that the AAO barrier layer can be perforated to expose the substrate surface at the pore base using a selective wet etching process. Finally, Au and Pt nanowires with controlled diameter from about 12 nm to about 120 nm were grown using electrodeposition to demonstrate the successful implementation of the W interlayer process for the through-pore AAO/AS process without modification of the nanostructure of the as-grown scaffold.

## 5.2 Experiments

Multilayer thin films, W (10 and 20 nm)/Au (200 nm)/Ti (15 nm) and W (80

nm)/Ti (15 nm), were deposited on thermally oxidized Si substrates using e-beam evaporation. The base pressure was $1 \times 10^{-6}$ Torr and the thickness of the films was determined using a quartz crystal monitor. Thin layers of Ti were used as adhesion layers for Au and W films on $SiO_2$ substrates. Al (500 nm) thin films were then deposited on the multilayer films.

Anodization of the multilayer thin films was carried under various anodic conditions to produce porous AAOs with different pore spacings $D_s$ and diameters $D_p$. For example, $V_{an}$ = 86V in 5 wt.% phosphoric acid solution at room temperature (RT) and $V_{an}$ = 89V in 0.3 M oxalic acid at 3°C were used to fabricate AAOs with $D_s \sim 200$ nm with $D_p \sim 120$ nm and 40 nm, respectively. For AAO with $D_s \sim 60$ nm and 100 nm, Al multilayers were anodized with 0.3 M sulfuric acid at $V_{an}$ = 25V and 3°C, and with 0.3 M oxalic acid at $V_{an}$ = 40V and 3°C, respectively. A mesh of platinum wires was used as the cathode. Anodic tungsten oxide which forms at the bottom of the pores in the AAO at the end of anodization of Al/W bilayer was removed using a pH 7 buffer solution (a mixture of sodium phosphate and potassium phosphate with pH = 7.00 at 25°C, VWR International) at room temperature for 10 min.

Gold and platinum nanowires were grown by electrodeposition in a through-pore AAOs on Au/Ti bilayers on a thermally oxidized Si wafers using a platinum counter electrode at RT. Gold was electroplated from a commercial solution (BDT®510, Enthone) and a constant current density of 0.25 $mA/cm^2$ was applied. For Pt, electrodeposition was conducted using a solution of 0.5 mM $K_2PtCl_4$ (Alfa Aesar) in 0.5 M $H_2SO_4$ at RT with application of a constant voltage of 0.01V versus a Ag/AgCl

reference electrode (Beckman). For fabrication of free-standing Au and Pt nanowires, the AAO scaffold was removed using a 25 wt.% tetramethylammonium hydroxide (TMAH, SACHEM, INC) solution at 60°C for 2 hours. TMAH solutions also remove the remaining W on Au substrates. After the AAO was removed, the sample was rinsed with acetone and isopropanol.

## 5.3 Results and Discussions

Figure 5-1 (a) and (b) illustrate conventional (Fig. 5-1 (a)) and W-interlayer (Fig. 5-1 (b)) process schemes for fabrication of through-pore AAO scaffolds for growth of nanowires or nanotubes. In our case, an Au film was used since it is a well-established electroplating base for growth of metallic nanowires. In the conventional process shown in Fig. 5-1 (a), a thin insulating barrier oxide, $Al_2O_3$, separates the pores from the Au substrate. In most cases, barrier removal is achieved by controlled chemical etching of the $Al_2O_3$. However, use of a chemical etching processes results in widening of the pore and therefore limits the ability to grow the smallest-diameter nanowires as defined by the as-grown AAO scaffold. Moreover, violent water electrolysis reactions at the Au substrate often induce mechanical failure of the AAO, though crack formation and even delamination from the substrates.

Figure 5-1 (b) presents the W interlayer process for formation of a through-pore AAO scaffold on an Au substrate, retaining the minimum pore diameter achieved in the as-grown scaffold. In the W interlayer process, a thin layer of tungsten is inserted between the Al film and the Au substrate, constituting an Al/W/Au tri-layer. When the tri-

layer is anodized, the anodization reactions proceeds as $O^{2-}$ ions reach each interface; with the W interlayer reacting with $O^{2-}$ ions, after porous AAO formation is finished, to form $WO_3$ that penetrates the barrier layers at the base of the AAO pores and, then, abrupt $O_2$ gas evolution occurs from reaction with the Au substrate upon complete consumption of W interlayer. By precisely controlling anodic oxidation of the W under the AAO, therefore, it is possible to achieve the condition for complete oxidation of W under the pore base without $O_2$ gas evolution, as illustrated in Fig. 5-1 (b). The Au surface at the bottoms of the pores can then be exposed by selective removal of the penetrating $WO_3$ with respect to both the AAO and the Au substrate through use of a wet etching process using pH 7 buffer solutions, as reported in our previous study [16]. Therefore, for ideal implementation of the W interlayer process, it is critical to determine the point at which the W thickness is fully consumed through $WO_3$ formation as a function of anodization parameters such as the anodic voltage, electrolyte chemistry, and anodization time for the W under the AAO.

To investigate the structural details of $WO_3$ formation at the base of the pores of AAO, the anodization of Al (500 nm)/W (80 nm) bilayers was conducted with application of a constant anodic voltage in various electrolytes. Figure 5-2 shows the anodic current density-time (*j*-t) curve for anodization of an Al/W bilayer in 5 wt.% $H_3PO_4$ at $V_{an}$ = 86V and at room temperature (RT). The anodic current density becomes constant at ~ 1.9 $mA/cm^2$ from 260 to 720 sec, indicating that the AAO forms in a steady-state. After the end of Al anodization, $WO_3$ forms at the pore bottom, where the electric field is concentrated with respect to the pore walls, and penetrates the $Al_2O_3$ barrier layer, in part

due to a large volume expansion ratio. In the *j*-t curve, as the anodization of W starts, the current density rapidly drops to about 0.5 mA/cm$^2$ and then more gradually decreases. After 1100 sec., the anodic current density saturates at less than 0.06 mA/cm$^2$.

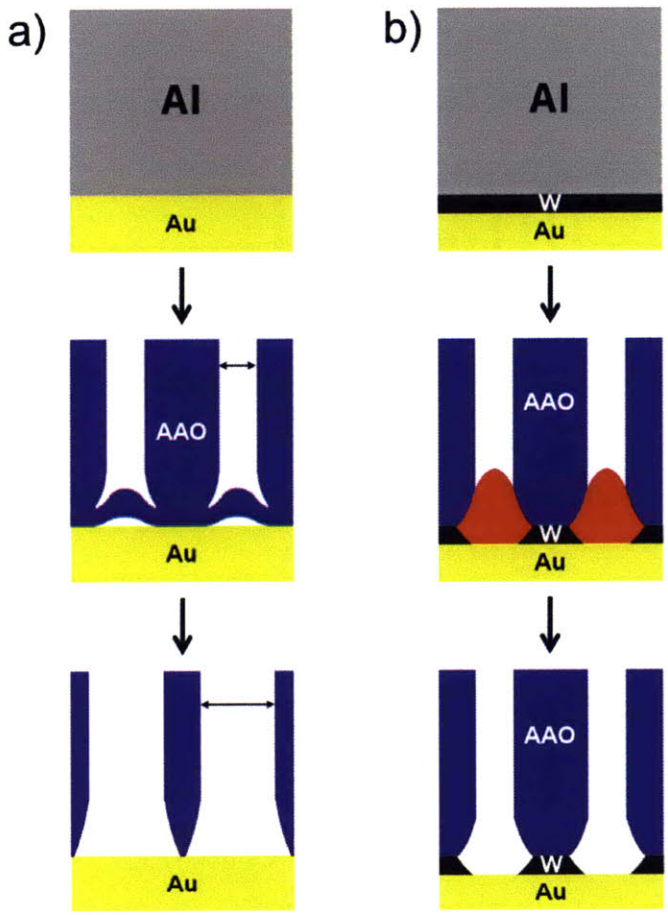


**Figure 5-1.** Schematic processes for fabrication of a through-pore AAO on a substrate. (a) The conventional process for anodization of an Al/Au bilayer followed by etching of the AAO to clear the barrier oxide at the base of the pore. This results in an increase in the pore diameter. (b) The new W interlayer process for anodization of an Al/W/Au tri-layer. Here, the W interlayer forms $WO_3$ that perforates the $Al_2O_3$ barrier layer and can be selectively etched to open the base of the pores without pore widening. The W also promotes adhesion of the AAO to the Au substrate.

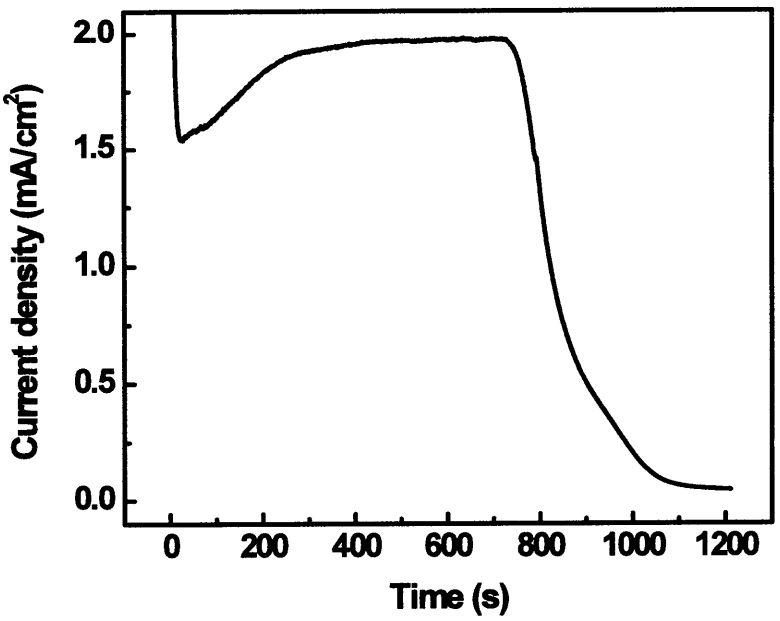


**Figure 5-2.** The anodic current density-time (*j*-t) curve for anodization of an Al/W bilayer in 5 wt.% phosphoric acid at 86V and room temperature. The tungsten oxide forms as the *j* begins to decrease. The gradual decrease and saturation in *j* at the end of anodization corresponds to barrier-type anodic oxidation of W.

It is well-known that anodization of W results in formation $WO_3$ with flat surfaces, forming a so-called barrier type oxide in electrolytes used to form porous AAO, such as phosphoric and sulfuric acid [23]. In contrast with porous oxide formation, for which the growth rate can be maintained at a steady state with application of a constant anodic voltage, growth of a barrier type oxide is self-limiting; and the growth of the oxide stops as the driving force for anodic oxidation, i.e. the electric field across the oxide, decreases as a result of thickening of the oxide at a fixed anodic voltage [24]. Since the anodic current density is directly related to the growth rate of the oxide by Faraday's law, the gradual decrease of the anodic current density in Fig. 5-2 confirms that the

penetrating $WO_3$ at the pore bottom also grows as a barrier type oxide and that the growth is self-limiting.

Figures 5-3 (a) and (b) show cross-sectional scanning electron microscopy (SEM) images of anodized Al/W bilayers under the condition shown in Fig. 5-2 for different anodization times at which $j$ drops to 1.17 and 0.2 mA/cm$^2$. Here, the selective removal of $WO_3$ using a pH 7 buffer solution for 10 min. was carried out to emphasize the formation of the perforating $WO_3$, and that dimples in the W underlayer were produced as a consequence of the constraint of oxidation of tungsten under the AAO pores. The depth of the dimples in the W layer was measured as a function of W anodization time. When the anodic current density rapidly drops, as shown in Fig. 5-3 (a), the barrier-perforating $WO_3$ forms only locally, due to non-uniform anodization of W under the AAO. As W anodization continues, with a gradual decrease in the anodic current density, the $WO_3$ penetrates the barrier layer of each pore of the AAO. The self-limiting nature of the $WO_3$ growth facilitates uniform perforation by suppressing the growth of the early-penetrating $WO_3$. Figure 5-3 (b) shows that the pore bases of the AAO are uniformly perforated when $j$ = 0.2 mA/cm$^2$. Figure 5-3 (c) shows the measured dimple depth in the W underlayer as a function of the W anodization time. The W anodization time is defined by subtracting the time at which the anodic current drops due to complete anodization of Al from total anodization time for the Al/W bilayer. For example, the W anodization times for Fig. 5-3 (a) and (b) were about 81 and 257 sec., respectively. Figure 5-3 (c) clearly shows that the anodic oxidation of the Al/W bilayer consumes about 19.3 nm of W for the formation of penetrating $WO_3$ in 5 wt.% $H_3PO_4$ at $V_{an}$ = 86V and room temperature, independently of

the W anodization time. This confirms that the anodic $WO_3$ grows as a barrier-type oxide under AAO.

The consumed thickness of the W layer for penetrating $WO_3$ formation was also measured under various porous AAO formation conditions. Figure 5-4 presents a summary of measurements of the W dimple depth as a function of the anodic voltage in different electrolytes, after treatment of $WO_3$ in pH 7 buffer solutions for 10 min. Anodic conditions, such as 0.3 M sulfuric acid at 25V and 3°C, and 0.3 M oxalic acid at 40V and 89V and 3°C, including 5 wt.% phosphoric acid at 86V and RT, were used. Since the $WO_3$ also grows as a barrier-type layer under sulfuric and oxalic anodization conditions, the Al/W bilayers were anodized until the anodic current density gradually decreased and saturated in all conditions, or for W oxidation times were 165, 170, and 60 sec. The measured dimple depth in the W films was about 10.4 nm at 25V, 11.5 nm at 40V, 19.3 nm at 86V and 24.5 nm at 89V.

The measured dimple depth shown in Fig. 5-4 allows determination of the optimum thickness of the W interlayer for fabrication of a through-pore AAO on any substrate, without enlarging the pore diameter and without violent anodic reactions with the substrate. It should be noted that the optimum thickness of the W interlayer must be empirically determined for each anodic voltage and electrolyte chemistry. For instance, Fig. 5-5 shows the *j*-t curves for anodization of Al/W/Au tri-layers in 5 wt.% $H_3PO_4$ at $V_{an}$ = 86V and RT, for which the optimum thickness of the W interlayer was determined to be about 19.3 nm, and illustrates the impact of the W interlayer thickness on the anodization behavior of the tri-layer. If the W interlayer thickness (10 nm) is thinner than the

optimum thickness (~ 19.3 nm), the resulting $WO_3$ is too thin, and the electric field across the oxide is still strong enough to drive oxygen ions to the Au substrate. In consequence, the anodic current surges due to $O_2$ evolution from the substrate immediately after Al/W anodization is finished. On the other hand, if the interlayer thickness is close to the W optimum thickness, the tungsten oxide can grow to its self-limiting thickness and the abrupt increase in the current density can be avoided, until the full thickness of the W interlayer is consumed. Additionally, in Fig. 5-3, we see that the barrier layer of the AAO can be perforated by stopping anodization of the Al/W layer when the current density starts to gradually decrease. Therefore, selective barrier perforation can be achieved by stopping anodization of the Al/W (20 nm)/Au tri-layer after a gradual decrease in the current but before the current surge, i.e. at about 160 sec of W anodization, or the time at which $j = 0.5$ mA/cm$^2$ in the $j$-t curve. The inset in Fig. 5-5 clearly shows that the surface of the Au substrate was exposed at the base of the pores through selective removal of the penetrated $WO_3$. Traces of W under the cellular boundary of the AAO also appeared where the AAO was detached during preparation for SEM imaging.

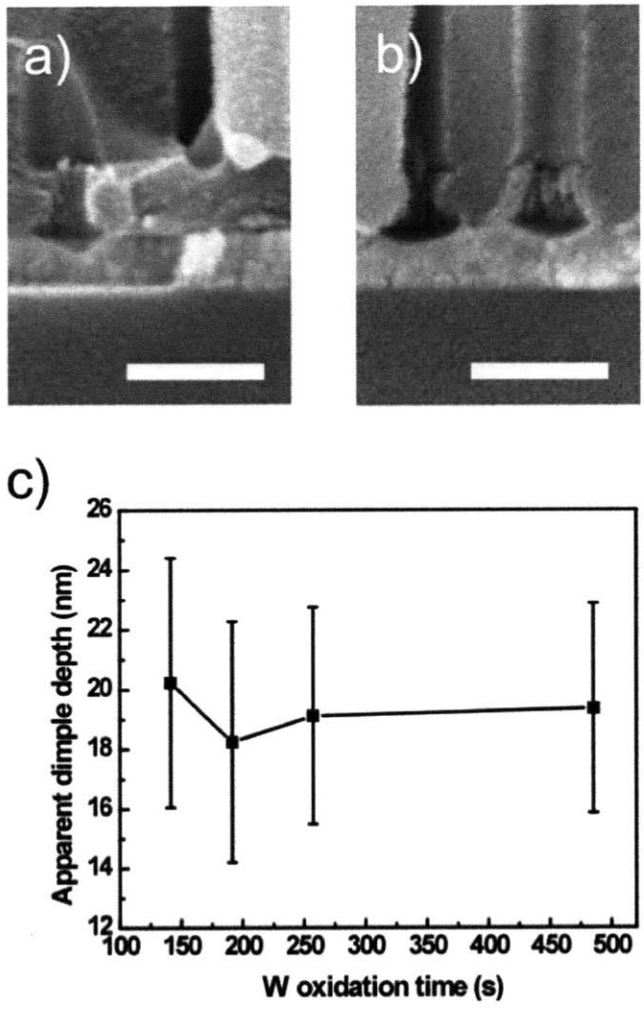


**Figure 5-3.** Cross-sectional scanning electron microscope images of through-pore AAO on a W underlayer, after anodization in 5 wt.% $H_3PO_4$ at 86V and RT until (a) $j$ = 1.17 mA/cm$^2$ (or the W oxidation time = 81 sec) and (b) $j$ = 0.2 mA/cm$^2$ (or the W oxidation time = 257 sec). The penetrating $WO_3$ at the pore bottom was removed using a pH 7 buffer solution for 10 min, revealing dimples in the W underlayer. Scale bars = 200 nm. (c) Measured depth of the dimples in the W underlayer as a function of W anodization time under the same anodization conditions as in (a) and (b).

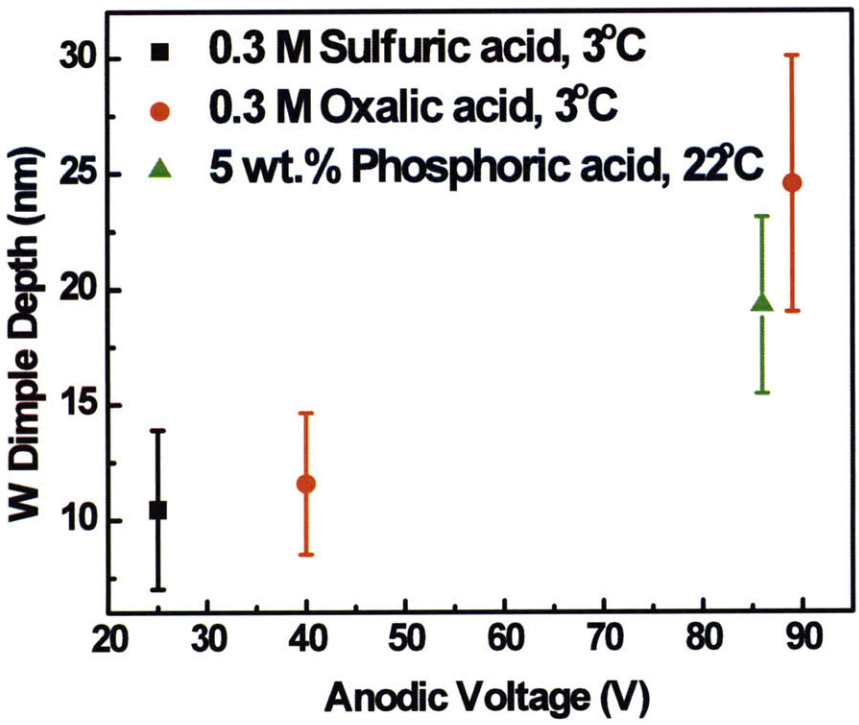


**Figure 5-4.** Depth of dimples in the W underlayer resulting from consumption of W to form the penetrating $WO_3$ at the base of the pores, measured under various anodization conditions. The measured depth of the dimples provides the optimum thickness of the W interlayer for each anodization condition.

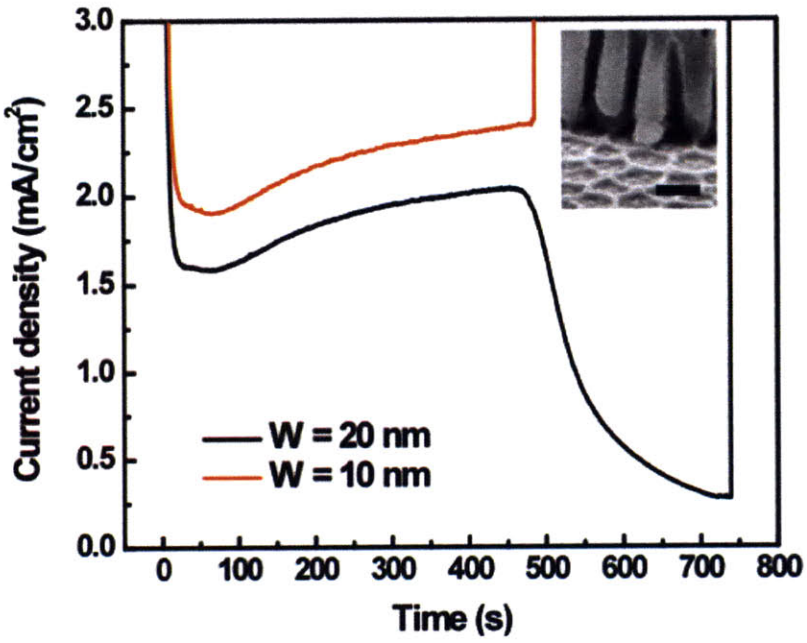


**Figure 5-5.** Effect of the thickness of the W interlayer on the anodic current density-time (*j*-t) curves for anodization of an Al/W/Au trilayer in 5 wt.% phosphoric acid at 86V and room temperature. For a W film with a thickness of 10 nm, j surges immediately after AAO formation is finished. Sequential anodic reactions are observed as the W oxidizes. The inset image shows a cross-sectional SEM image of the through-pore AAO on Au with a 20nm thick layer after anodization was stopped when j = 0.5 mA/cm$^2$. Scale bar = 200 nm.

Figure 5-6 shows SEM images of arrays of gold and platinum nanowires electrodeposited in selectively perforated AAO scaffolds on Au substrates using the W interlayer process under various anodization conditions. The AAO scaffolds were fabricated by anodizing the Al/W/Au tri-layers in 5 wt.% phosphoric acid at 86V and room temperature (Fig. 5-6 (a)), 0.3 M oxalic acid at 40V and 3°C (Fig. 5-6 (b)), and 0.3 M sulfuric acid at 25V and 3°C (Fig. 5-6 (c) and (d)). The Au surfaces were exposed by selectively etching the penetrating $WO_3$. After the growth of the Au and Pt nanowires, the through-pore AAOs were etched for release of the nanowires. Two different thicknesses of the W interlayer (10 and 20 nm) were used, based on the dimple depth measurements shown in Fig. 5-4. Using the scaffolds with different nanostructures, nanowires with various diameters and densities were grown. For example, Fig. 5-6 (a) and (b) shows vertically-aligned Au nanowires with diameters of about 120 nm, and 31.8 nm, respectively. Figure 6 (c) shows an SEM image of the Pt nanowires grown in the scaffold with the smallest pore diameter (~ 12 nm) used in this work, demonstrating that the diameters of the nanowires are the same as the pore size of the as-grown AAO scaffold. In addition, a low magnification image of the Pt nanowire array (Fig. 5-6 (d)) demonstrates that Pt nanowires with diameters of about 10 nm can be uniformly grown on the Au substrates over very large areas using the W interlayer process.

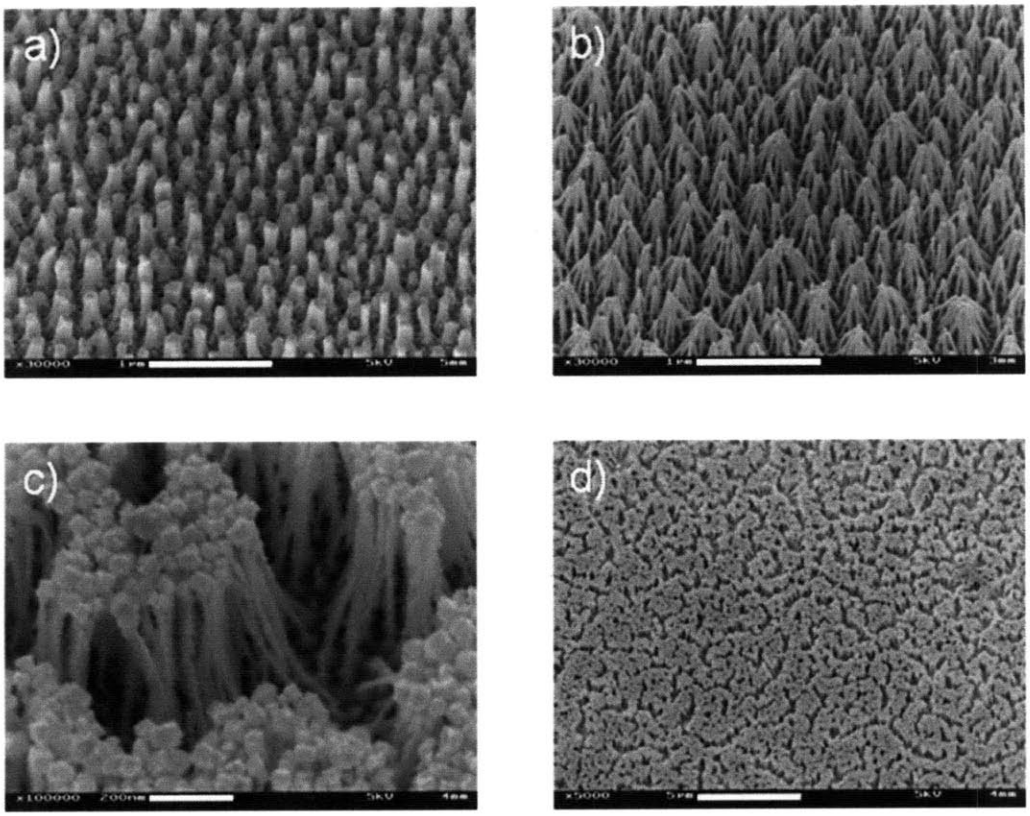


**Figure 5-6.** Tilted-angle (30°) SEM images of free-standing Au and Pt nanowires on Au substrates, formed by electrodeposition in various through-pore AAOs formed with controlled pore diameters. (a) Au nanowires with diameters of about 120 nm and spacings of about 200 nm and lengths of about 590 nm and (b) Au nanowires with diameters of about 31.8 nm and spacings of about 100 nm and lengths of about 530 nm. Scale bars = 1 μm. (c) Pt nanowires with 12 nm diameters, spacings of 65 nm and lengths of about 710 nm. Scale bar = 200 nm. (d) Large-area view of the Pt nanowires in (c). Scale bar = 5 μm.

## 5.4 Conclusions

We developed a W interlayer process for formation of small-diameter through-pore AAO scaffolds with different pore diameters and spacings on an Au substrate. The W interlayer process is based on anodization of an Al/W/Au tri-layer with precise control of the W thickness for the formation of AAO scaffolds with the $WO_3$ extrusion at the pore bottoms and selective removal of the $WO_3$ to expose the surface of the Au substrate, without widening pore diameter.

For precise control of the W thickness, we first showed that anodic oxidation of W constrained under AAO consumes a constant thickness of W with application of a constant voltage in acidic electrolytes. From comparison of the j-t curve and the structural evolution of the penetrating $WO_3$ during anodization of Al/W bilayer, we showed that the saturation in the anodic current density at the end of anodization indicates the self-limiting nature of the $WO_3$ growth. We then determined the thickness of consumed W for anodic oxidation under the pore bottom in various anodization conditions.

A through-pore AAO on an Au substrate was fabricated by anodization of an Al/W/Au tri-layer with W interlayers with optimum thickness. For example, the optimum thickness of the W interlayer for anodization of the tri-layer in sulfuric acid at 25V is about 10 nm. The barrier layer at the pore bottom can be perforated by formation of the penetrating $WO_3$ which can be monitored by the j-t curve of the anodization of the tri-layer and the Au surface is exposed by selective wet etching of the penetrating $WO_3$ in pH 7 buffer solution for 10 min.

Using such scaffolds, vertically aligned free-standing Au and Pt nanowires with

different diameters from about 12 nm to 120 nm were grown on Au substrates by electrochemical deposition. Since anodization of an Al/W/Au tri-layer proceeds in sequential manner and anodic oxidation of the W interlayer is self-limiting, the W interlayer process developed in this work can be applied to other substrates under a range of specific anodization conditions. Therefore, the W interlayer process provides a simple way to fabricate a through-pore AAO scaffolds for the growth of hetero-epitaxial nanowires or 1-D nanomaterials with controllable Ohmic and Schottky contact on substrates required for various applications.

## References


1. Xia, Y.N., et al., *One-dimensional nanostructures: Synthesis, characterization, and applications*. Advanced Materials, 2003. **15**(5): p. 353-389.

2. Bhushan, B., ed. *Springer hnadbook of nanotechnology*. 2004, Springer-Verlag: Heidelbert. 99 - 145.

3. Hicks, L.D. and M.S. Dresselhaus, *Thermoelectric figure of merit of a one-dimensional conductor.* Physical Review B, 1993. **47**(24): p. 16631-16634.

4. Yao, J., et al., *Optical negative refraction in bulk metamaterials of nanowires*. Science, 2008. **321**(5891): p. 930-930.

5. Taberna, L., et al., *High rate capabilities Fe3O4-based Cu nano-architectured electrodes for lithium-ion battery applications*. Nature Materials, 2006. **5**(7): p. 567-573.

6. Martin, C.R., *NANOMATERIALS - A MEMBRANE-BASED SYNTHETIC APPROACH*. Science, 1994. **266**(5193): p. 1961-1966.

7. Kline, T.R., et al., *Template-grown metal nanowires*. Inorganic Chemistry, 2006. **45**(19): p. 7555-7565.

8. Thurn-Albrecht, T., et al., *Ultrahigh-Density Nanowire Arrays Grown in Self-Assembled Diblock Copolymer Templates*. Science, 2000. **290**(5499): p. 2126-2129.

9. Keller, F., M.S. Hunter, and D.L. Robinson, *Structural Features of Oxide Coatings on Aluminum*. Journal of the Electrochemical Society, 1953. **100**(9): p. 411-419.

10. O'Sullivan, J.P. and G.C. Wood, *The Morphology and Mechanism of Formation of Porous Anodic Films on Aluminium*. Proceedings of the Royal Society of London. A. Mathematical and Physical Sciences, 1970. **317**(1531): p. 511-543.

11. Masuda, H. and K. Fukuda, *Ordered Metal Nanohole Arrays Made by a 2-Step Replication of Honeycomb Structures of Anodic Alumina*. Science, 1995. **268**(5216): p. 1466-1468.

12. Lee, W., et al., *Fast fabrication of long-range ordered porous alumina membranes by hard anodization*. Nature Materials, 2006. **5**(9): p. 741-747.

13. Crouse, D., et al., *Self-ordered pore structure of anodized aluminum on silicon and pattern transfer.* Applied Physics Letters, 2000. **76**(1): p. 49-51.

14. Rabin, O., et al., *Formation of thick porous anodic alumina films and nanowire arrays on silicon wafers and glass*. Advanced Functional Materials, 2003. **13**(8): p. 631-638.

15. Tian, M.L., et al., *Penetrating the oxide barrier in situ and separating freestanding porous anodic alumina films in one step*. Nano Letters, 2005. **5**(4): p. 697-703.

16. Oh, J. and C.V. Thompson, *Selective barrier perforation in porous alumina anodized on substrates*. Advanced Materials, 2008. **20**(7): p. 1368-1372.

17. Chu, S.Z., et al., *Formation and microstructures of anodic alumina films from aluminum sputtered on glass substrate*. Journal of the Electrochemical Society, 2002. **149**(7): p. B321-B327.

18. Kevin P. Musselman, et al., *Low-Temperature Synthesis of Large-Area, Free-Standing Nanorod Arrays on ITO/Glass and other Conducting Substrates*. Advanced Materials, 2008. **20**(23): p. 4470-4475.

19. Stefan Mátéfi-Tempfli and Mária Mátéfi-Tempfli, *Vertically Aligned Nanowires*

*on Flexible Silicone using a Supported Alumina Template prepared by Pulsed Anodization*. Advanced Materials, 2009. **21** (40): p. 4005-4010.

20. Shimizu, T., et al., *Synthesis of vertical high-density epitaxial Si(100) nanowire arrays on a Si(100) substrate using an anodic aluminum oxide template*. Advanced Materials, 2007. **19**(7): p. 917-920.

21. Mozalev, A., et al., Electrochim. Acta, 2003. **48**: p. 3155-3170.

22. Iwasaki, T., T. Motoi, and T. Den, *Multiwalled carbon nanotubes growth in anodic alumina nanoholes*. Applied Physics Letters, 1999. **75**(14): p. 2044-2046.

23. Shimizu, K., et al., Corros. Sci., 1998. **40**: p. 1229-1238.

24. Diggle, J.W., T.C. Downie, and C.W. Goulding, *Anodic oxide films on aluminum*. Chemical Reviews, 1969. **69**(3): p. 365-405.

# Chapter 6. Summary and Future Work

## 6.1 Summary

For 50 years, field-assisted dissolution of the oxide has been the generally accepted model for formation of porous alumina. According to this model, it is suggested that the dissolution rate of the oxide is greatly enhanced in pore-forming electrolytes in the presence of the external field during anodization and hence steady-state pore formation can be maintained. However, the dissolution rate of the oxide as a function of the external electric field has never been measured, partly due to the fact that the anodic oxidation of Al is in dynamic balance between dissolution at the oxide/electrolyte (o/e) interface and oxidation at the metal/oxide (m/o) interface.

In work performed for this thesis, we developed a new experimental procedure, called discontinuous anodization, to decouple dynamic equilibrium between two interfaces as a function of the electric field during Al anodization. In discontinuous anodization, an $Al_2O_3$ layer with flat surfaces is first formed, and the thickness was then reduced through use of a controlled applied anodic voltage, and therefore a changing E-field across the oxide during anodization in acidic electrolytes. We quantitatively demonstrated that the dissolution rate of the oxide was enhanced in the presence of the external E-field and pore formation initiated due to a field-induced instability. However, the spacing of the pore structures resulting from this field-induced instability was significantly different from that of the well-known porous structures studied in previous work. The spacing of these pores also had a linear dependence on the anodic voltage

which is significantly smaller than the pore spacing of the conventional pores. The field-assisted dissolution model is therefore not consistent with these experimental results.

Instead, it is demonstrated that mechanical behavior of the anodic oxide has a governing role in initiation and steady-state growth of pores during Al anodization. It is shown that the well-known pore structures initially form due to a mechanical instability and the pore spacings are initially determined by the fastest growing wavelength, $\lambda_{max}$. In addition, the steady-state pore growth is a result of forced plastic deformation and flow of the oxide. Based on these observations, a model, in analogy with cellular solidification, is proposed to quantitatively explain the formation of hexagonally closed packed porous AAO at certain anodization conditions, based on the flux balance between oxidation and lateral plastic flow at the m/o interface. In this model, repulsive mechanical interactions of each pore arising from the need to share a volume in which the oxide flows are suggested as a driving force for self-organization of the pores.

New insight gained from this mechanistic study of formation of porous aluminum oxide allowed us to develop new routes to nano-structuring of AAO scaffolds for assembly of ordered arrays of low-dimensional materials with controlled diameter, spacing, and orientation with respect to a substrate surface.

Horizontal porous AAO (H-AAO) on a substrate provides an ideal platform for growth of ordered arrays of semiconducting nanowires and nanotubes in the plane of a substrate surface. H-AAO can be fabricated by anodizing vertical sidewalls of patterned Al films capped with insulating $SiO_2$ mask layers. The mask layers prevent unwanted anodization at the top surfaces. However, plastic deformation and flow of the aluminum

oxide are severely inhibited during anodization of Al in mechanically confined structures. Under anodization conditions for which 140% of volume expansion is expected, mechanical constraints are shown to result in formation of periodic dendrite inner pore structures and a reduction of the growth rate under self-ordering anodization conditions. Based on this mechanistic understanding, we demonstrated that anodization conditions that lead to zero volume expansion avoid dendritic H-AAO pores and kinetic retardation of pore formation. This is a new and potentially very useful result.

A process for perforation of the insulating barrier oxides at the base of pores, without modifying porous structure from as-grown AAO films, was developed. This process can be carried out on any conducting substrate. In the process, plastic deformation and flow of $Al_2O_3$ facilitates penetration of anodic $WO_3$, which has a high volume expansion ratio of ~ 3.6, into the barrier layer of the porous AAO during anodization of Al/W bilayers on a Si substrate. This allows exploitation of a new selective barrier perforation process, since the two anodic oxides are chemically distinct and can be selectively etched.

In chapter 4, we present a thermodynamic background for a selective wet etching process for of $WO_3$ with respect to $Al_2O_3$ using pH 7 buffered solutions. We also successfully demonstrated selective removal of penetrated $WO_3$ to expose a metallic W surface at the base of pores. without changing the as-anodized pore structure. In chapter 5, we discussed a further refinement of this process, and report a W interlayer process for fabrication of a through-pore AAO scaffold on any conducting substrate (AS) by anodizing Al/W/AS tri-layers. By empirically determining the optimum thickness of the

W interlayer for specific anodization conditions and by selective wet etching of the anodic $WO_3$ on AS, we successfully demonstrate through-pore AAOs on a variety of substrates for various anodization conditions without changing the pore diameter on any substrate. With this W interlayer process, we fabricated vertically aligned free-standing Au and Pt nanowires by electrodeposition on an Au substrate.

## 6.2 Future Work

Through the work described in this thesis, we showed that the growth stress of the anodic oxide formed during anodization drives pore initiation due to a mechanical instability and that steady-state pore growth results from plastic deformation and flow of the oxide. However, there has been very limited work done on measurement of the growth stress during anodization. To elucidate the detailed origins of the mechanical instability, it is important to understand the stress evolution of the oxide during pore formation as a function of anodic conditions. For example, as we discussed in chapter 2, the origin of the mechanical instability (energetically driven or kinetically driven strain instabilities) can be indentified from monitoring how the critical wavelength depends on the critical stress, i.e. $\lambda_c \propto 1/\sigma_c$ or $\lambda_c \propto 1/\sigma_c^2$. Therefore, future work should include in-situ growth stress measurements under various anodization conditions. Furthermore, the effects of the externally applied stresses on the pore spacing at the on-set of pore formation should also be investigated.

In chapter 2, we showed that plastic flow of the oxide drives self-ordering of pores in a steady state. In chapter 3, we also showed that the growth rate of porous

alumina is greatly reduced as a result of suppressed plastic deformation and flow needed when anodization leads to a volume expansion. Therefore, the next question is how ordering and the growth rate of porous anodic oxides in steady-state are affected by external stress during anodization. Moreover, anodic alumina shows significant plasticity during anodization, while $Al_2O_3$ is known as a brittle material. Therefore, future work should include studies of the origin of the plasticity of the oxide during anodization. In analogy to discontinuous anodization, this can be done using tensile mechanical tests of the pre-formed oxides as a function of the E-field during anodization.

Finally, through the work described in chapter 4 and 5, we demonstrated fabrication of metallic nanowires with various diameters on any substrate. In future work, the various electrical and electrochemical properties of the arrays of metallic nanowires should be evaluated for use in functional devices.